University of Plymouth

PEARL **https://pearl.plymouth.ac.uk**

04 University of Plymouth Research Theses 01 Research Theses Main Collection

2013

Investigation of baroclinic tides in the northern South China Sea

Guo, Chuncheng

http://hdl.handle.net/10026.1/1500

http://dx.doi.org/10.24382/4336
University of Plymouth

All content in PEARL is protected by copyright law. Author manuscripts are made available in accordance with publisher policies. Please cite only the published version using the details provided on the item record or document. In the absence of an open licence (e.g. Creative Commons), permissions for further reuse of content should be sought from the publisher or author.

This copy of the thesis has been supplied on condition that anyone who consults it is understood to recognize that its copyright rests with its author and that no quotation from the thesis and no information derived from it may be published without the author's prior consent.

Investigation of baroclinic tides in the northern South China Sea

Chuncheng Guo

Faculty of Science and Technology

Plymouth University

A thesis submitted to Plymouth University in partial fulfillment of the requirements for the degree of:

Doctor of Philosophy

January 2013

Abstract

Investigation of baroclinic tides in the northern South China Sea

Chuncheng Guo

Baroclinic tides result from the interaction of barotropic tides with topography in stratified oceans. They play an important role in driving deep ocean mixing. In this research, investigations of the dynamics of baroclinic tides and internal solitary waves (ISWs) in the northern South China Sea (SCS) are conducted, mainly by means of the Massachusetts Institute of Technology general circulation model (MITgcm).

Firstly, simulations of internal wave generation at the Luzon Strait (LS) are carried out. By conducting three-dimensional (3D), high-resolution experiments, it was found that the generated wave field features a multi-modal structure: large, pronounced ISWs of first mode (amplitude $\sim 120\ m$) and second mode (amplitude $\sim 120\ m$) were reproduced. The two north-south aligned ridges in the LS contribute together to the generation of the second mode ISWs, whereas the easternmost ridge of the two is responsible for the first mode ISWs. It was found that multiple generation mechanisms of internal waves could occur in this region, and overall it belongs to a mixed lee wave regime.

A specific type of short internal waves arose during the 3D simulation. These ride on a second mode ISW with similar phase speed, trailing a first mode ISW. The short waves possess wavelengths of $\sim 1.5\ km$ and amplitudes of $\sim 20\ m$, and only show up in the upper layer up to a depth of $\sim 500\ m$. Scrutiny of the generation process showed that these short waves appear in two distinct regions and are produced due to two mechanisms, namely, the disintegration of an inclined baroclinic bore near the LS, and the overtaking of a second mode ISW in the deep water by a faster first mode ISW. Robust evidence has been sought from satellite imagery and by solving the theoretical Taylor-Goldstein Equation to verify their existence.

The effects of superposition of multiple tidal harmonics (diurnal and semidiurnal) on the resultant ISW generation were investigated. It was first found that, by analyzing historical observational data, the occurrence of ISWs in the far-field always follow strong semidiurnal barotropic tidal peaks in the LS, regardless of whether it is the maximum for the diurnal or total tidal strength. However, modelling results of MITgcm and a linear internal tide generation model demonstrate that the diurnal tidal harmonics modulate the arrival time and amplitude of the propagating ISWs. Specifically, it leads to the emergence of the so-called A and B type ISWs and an alternation and transition between the two.

Secondly, the shoaling process of ISWs in the northern SCS slope-shelf area is investigated. A series of two-dimensional (2D) experiments are set up to study the shoaling of a large-amplitude second mode concave ISW over a linear slope that resembles the SCS slope. Modelling results show that a strong transformation of the wave profile starts to take place when the wave is approaching the shelf break. A convex type wave is born at the trailing edge of the incident

wave and gradually disintegrates into a group of ISWs due to the steepening of the rear wave profile. The frontal face of the wave gets flatter when travelling on the slope, but forms a steep structure right above the shelf break. However, this steep structure shows no tendency to evolve into an ISW: instead, it gets increasingly flat again while evolving on the shelf. The trailing convex wave packet travels faster and merges with the frontal concave wave. Finally, a wave packet with rank-ordered convex ISWs moves forward steadily on the shelf. Energy transfer to the ambient modes is evident, as both first mode and higher modes are clearly seen during and after the shoaling process.

First mode ISW evolution is studied too by performing 3D, high-resolution experiments over the wide northern SCS slope and shelf area. It was found that the wave profiles change drastically near the shelf break and the Dongsha Atoll. In agreement with satellite imagery, the wavefront of the leading ISW becomes more spatially oblique with respect to its original orientation as it progresses westward due to the inclination of the slope in the topography. Wave disintegration is prominent in the shallow water zone, and wave polarity reverses near the turning point (at the 130 m isobath), which is consistent with the predictions of weakly nonlinear theory. A series of 2D experiments were set up to inspect the effects of rotation on the shoaling ISW. The results indicate that under the rotation, upon reaching the continental shelf, one shoaling ISW could disintegrate into one ISW packet and one secondary solibore that contains a number of rank-ordered waves with much shorter wavelength than an ISW. The secondary solibore is very pronounced in the northern portion of the northern SCS slope and shelf, but could hardly be discerned in the southern portion, which is consistent with the outcome of 3D simulations.

Contents

List of Figures

Acknowledgements

I am most grateful to my three supervisors, Dr. Vasyl Vlasenko, Dr. Nataliya Stashchuk, and Prof. Xueen Chen. My PhD degree could not have been fulfilled smoothly without your great support and efforts. As my director of study, Vasyl has been supervising me since September 2009, when I was a visiting student at the University of Plymouth. Vasyl and Nataliya have impressed me greatly with their superb knowledge and persistent enthusiasm in research, which I consider an invaluable treasure for my academic career. Their guidance, encouragement, and of course, magnificent personality, have been indispensable for the successful completion of my project. I'm very proud and pleased that they took me on as their student, and guided me in depth to the mysterious and fascinating area of ocean science.

My sincere gratitude certainly also goes to Prof. Xueen Chen, who, despite being my third supervisor, has been crucial in my personal development. I remember very well that it was a freezing evening in the winter of 2007 that I first met you. Today it has been about 5 years under your supervision and I consider myself a lucky one to be recruited by you. Prof. Chen is a gracious gentleman and is known for being very kind and generous to his students. Your unselfishness, prestige, and passion for my work are most beneficial to my project and certainly to my career.

I wholeheartedly thank all my friends and colleagues, and those who have ever helped me in the UK. Your support and assistance have made my life easier and richer. You are all so great and wonderful. I will surely miss you folks and I wish you all the best and a successful completion of your PhDs.

I'm most indebted to every member of my family. I'm grateful that you have always been working hard to maintain an easy, hilarious, and harmonic family after all the things we have been through. You have taught me, as a man, what is responsibility, persistence, respect, fidelity, and sentience, which are the most precious qualities that have all taken root in my blood. Your infinite support and deep love are the biggest motivations of my life. I love every one of you, and I will never walk alone.

I thank my two examiners, Prof. Toby Sherwin (external examiner) and Dr. Phil Hosegood (internal examiner) for all the efforts they have put into evaluating my thesis. Toby and Phil have raised insightful comments that have significantly improved the quality of the thesis. Their professional attitude and enthusiasm on my work are greatly appreciated.

My PhD project is funded by the China Scholarship Council (CSC), which has covered fully my tuition fee and living stipend. Their sponsorship is greatly acknowledged.

Authors declaration

At no time during the registration for the degree of Doctor of Philosophy has the author been registered for any other University award.

All the materials presented in this thesis are the author's original work, except for Chapters 4.4, 6.2, and 6.4, which were done in collaboration with Vasiliy Vlasenko and Nataliya Stashchuk, who contributed about 80% thereof.

Relevant scientific seminars and conferences were regularly attended at which work was often presented. Five papers have been accepted for publication in refereed journals.

Signed: _____

Date: _____

Publications :

Vlasenko, V. & Stashchuk, N. & **Guo, C.** & Chen, X. *Multimodal structure of baroclinic tides in the South China Sea.* **Nonlinear Processes in Geophysics,** 2010 , 17, 529-543.

Guo, C. & Chen, X. & Vlasenko, V. & Stashchuk, N. *Numerical investigation of internal solitary waves from the Luzon Strait: Generation process, mechanism and three-dimensional effects.* **Ocean Modelling,** 2011 , 38, 203-216.

Guo, C. & Chen, X. *Numerical investigation of large amplitude second mode internal solitary waves over a slope-shelf topography.* **Ocean Modelling,** 2012 , 42, 80-91.

Guo, C. & Vlasenko, V. & Alpers, W. & Stashchuk, N. & Chen, X. *Evidence of short internal waves trailing strong internal solitary waves in the northern South China Sea from synthetic aperture radar observations.* **Remote Sensing of Environment,** 2012 , 124, 542-550.

Vlasenko, V. & **Guo, C.** & Stashchuk, N. *On the mechanism of A-type and B-type internal solitary wave generation in the northern South China Sea.* **Deep Sea Research I,** 2012 , 69, 100-112.

Guo, C. & Chen, X. *A review of internal solitary wave dynamics in the northern South China Sea.* **Progress in Oceanography,** 2013 (accepted).

[Posters and conference presentations]:

2010:

Dragon 2 Mid-term Results Symposium, *Guilin, China.* **Poster presentation:** Multimodal structure of baroclinic tides in the South China Sea.

The Second International Conference: Nonlinear Waves-Theory and Applications, *Beijing, China.*

2011:

European Geosciences Union (EGU) annual assembly, *Vienna, Austria.* **Poster presentation:** Numerical simulation on the transformation of large amplitude second mode internal solitary waves over a slope-shelf topography.

The 16th Pacific-Asian Marginal Seas Meeting (PAMS) *Taipei, Taiwan.* **Oral presentation:** On the generation and evolution of internal solitary waves in the northwest of South China Sea.

The 16th Pacific-Asian Marginal Seas Meeting (PAMS) *Taipei, Taiwan.* **Poster presentation:** Numerical simulation on the transformation of large amplitude second mode internal solitary waves over a slope-shelf topography.

2012:

European Geosciences Union (EGU) annual assembly, *Vienna, Austria.* **Poster presentation:** Short internal waves trailing strong internal solitary waves in the South China Sea.

16th biennial Joint Numerical Sea Modelling Group (JONSMOD) workshop, *Brest, France.* **Oral presentation:** Short internal waves trailing strong internal solitary waves in the South China Sea.

Nonlinear Waves in Fluids, *Loughborough, UK.* **Oral presentation:** The effect of rotation on shoaling of large amplitude internal solitary waves in the northern South China Sea.

American Geophysical Union (AGU) Fall Meeting, *San Francisco, US.* **Poster presentation:** The effect of rotation on shoaling of large amplitude internal solitary waves in the northern South China Sea.

Word count for the main body of this thesis: 50000

Chapter 1

Introduction

1.1 Background

The key role played by internal waves in mixing the ocean has been reconsidered in more recent years following the recognition from satellite altimeter data that about a third of barotropic tidal energy is lost in the open ocean rather than the shallow marginal seas (Egbert & Ray 2000). Diapycnal mixing processes in the ocean are crucial in determining the circulation and climate change (Munk & Wunsch 1998, Wunsch & Ferrari 2004). It takes place at the smallest scales and is the termination of a variety of dynamical processes. The breaking of internal waves is believed to be a leading source in mixing the ocean. Internal tides are a kind of internal wave with tidal frequency. They are ubiquitous in the world's oceans (Simmons et al. 2004, Garrett & Kunze 2007) and are primarily generated by barotropic tides flowing over topographic features. The wind-generated near-inertial waves and internal tides are critical in mixing the upper and abyssal oceans, respectively.

The transfer of barotropic tidal energy into eventual heat goes through several processes. Upon flowing over rough topographies, a portion of barotropic tidal energy is locally directly lost, whereas the rest converts into baroclinic energy by the generation of internal tides. The baroclinic energy either locally dissipates or propagates out of the source region in the form of low-mode internal tides. The radiated internal tides can be destroyed by processes like shear instability and nonlinear wave-wave interactions, or, after traveling a long range, dissipate in the margins of the ocean. Munk & Wunsch (1998) presented a chart of the global budget of tidal energy flux and concluded that 2.1 Terawatts (TW) of tidal energy must be dissipated throughout the ocean to maintain the abyssal stratification, and an estimation of a bulk turbulent diffusivity of $10^{-4}\ m^2 s^{-1}$ was obtained. Observed turbulent diffusivity in the ocean varied from $10^{-5}\ m^2 s^{-1}$ in the thermocline (Ledwell et al. 1993) to larger than $10^{-3}\ m^2 s^{-1}$ in the deep basin above rough topography (Polzin et al. 1997, Ledwell et al. 2000). The main source of the energy comes from the breaking of internal waves. Munk & Wunsch (1998) estimated that about one Terawatt of energy lost from barotropic tide is due to the internal tides. After Munk & Wunsch (1998), there have been a number of attempts to quantify the tidal energy budget that involves the estimation of tidal conversion and turbulent diffusivity (Simmons et al. 2004, Arbic et al. 2012). There has also been an increasing number of large-scale in situ measurements, for example, the Brazil Basin Tracer Release Experiment (Polzin et al. 1997, Ledwell et al. 2000), the Hawaii Ocean Mixing Experiment (Nash et al. 2006, Rainville & Pinkel 2006). These experiments have greatly stimulated the progression of internal tide and mixing process study.

When linear internal tides are radiated out of the generation site, it is known that they are subject to nonlinear effects, which act to steepen and shorten the wave profile. Nonlinear internal waves, which are also referred as internal solitary waves (ISWs) or solitons, are a kind of coherent structure that is perfectly balanced by the steepening effects of nonlinearity and dispersive

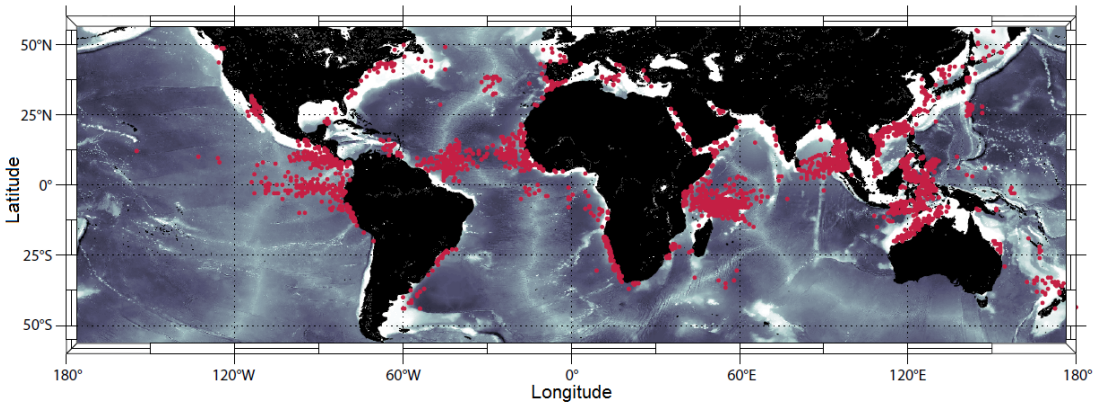

Figure 1.1: Locations of ISWs that were observed by Moderate-Resolution Imaging Spectroradiometer (MODIS) acquired from August 2002 through May 2004 (figure adopted from Jackson et al. (2012)).

effects of nonhydrostaticity. Such a balance leads to the longevity and persistence of the wave profile (Apel et al. 2006). The history of ISWs dates back to the studies of Russell (1844), whose observations and experiments were later confirmed theoretically by Boussinesq (1871), Rayleigh (1876), followed by the work of Korteweg & de Vries (1895) that yielded the famous Korteweg-de Vries (KdV) equation. By integrating the KdV equation, a more recent work by Zabusky & Kruskal (1965) showed that ISWs can be generated from very general initial conditions and one ISW can collide elastically with another.

There are quite a few pathways that could lead to the generation of ISWs, of which the most common one is a result of their origin in the tide-topography interaction, which produces internal tides that subsequently steepen during the evolution process. Figure 1.1 is a compiled map of ISW occurrences across the globe, from which its widespread and ubiquitous nature can be clearly seen. These hot spots are mostly situated in the marginal seas where the bathymetry transitions sharply to the shallow continental shelf. Given their often large scale and energetic motion, ISWs are known to be a potential hazard to offshore drilling platforms and submarines and have important consequences for underwater acoustics, shelf biology and dynamics.

ISWs in the northern South China Sea (SCS) have been of great interest to oceanographers in the last decade, due to their regular occurrence (twice a day) and impressive scales (up to $\sim$150 m). The northern SCS is a regional sea that is approximately located between $112^\circ \sim 122^\circ E$ and $18^\circ \sim 23^\circ N$ (Figure 1.2). It is connected to the western Pacific in the east through a gateway named Luzon Strait (LS), and in the south it is linked to the rest of the SCS. Meridionally the LS features two parallel tall, steep ridges, namely the eastern ridge (Lan-Yu Ridge) and the western ridge (Heng-Chun Ridge). The eastern ridge is taller and a couple of islands are randomly distributed on it. West of the two-ridged LS is the deep northern SCS basin (water depth greater than 3000 m) which zonally covers nearly 200 km, and which gradually transitions to the continental slope and shelf that cover a massive area with significant three-dimensional (3D) bathymetry.

ISWs in the northern SCS are energetic and ubiquitous (Figure 1.3). Numerous studies have been carried out to look into the internal wave properties and dynamics in this area. In situ measurements (Ramp et al. 2004, Alford et al. 2010, 2011) and satellite imagery (Zhao et al. 2004,

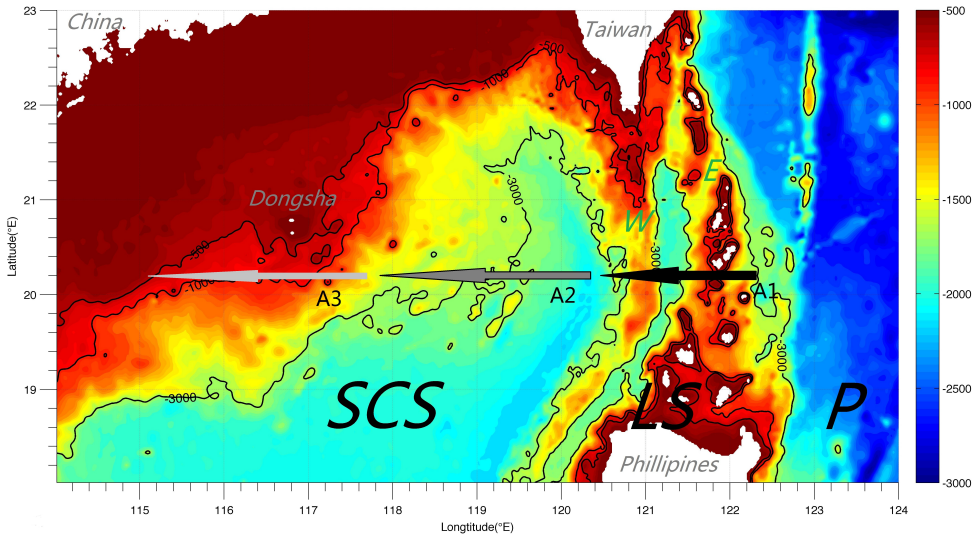

Figure 1.2: Bathymetry of the northern SCS (-500, -1000, and -3000 m isobaths are shown). The letters indicate some important geographical locations: *SCS* denotes the South China Sea; *LS* denotes the Luzon Strait; *P* denotes the Pacific Ocean; *E* denotes the eastern ridge of the LS (Lan Yu Ridge); *W* denotes the western ridge of the LS (Heng Chun Ridge). The three arrows, from right to left (A1-A3), indicate the approximate regions of internal wave generation in the LS, internal wave propagation in the deep basin, and internal wave shoaling and dissipation on the continental slope and shelf.

Zheng et al. 2007) are fundamental and illuminating in the early stages of study, supplemented in more recent years by state-of-the-art numerical simulations with increasingly realistic configurations (Vlasenko et al. 2010, Zhang et al. 2011, Buijsman et al. 2012). Unanimous conclusion has been reached in terms of the origin of these large waves, viz., strong zonal barotropic tides interact intensely with the two ridges at LS, which results in the production of large baroclinic tides that subsequently evolve into ISWs under the consistent shaping of nonlinear, nonhydrostatic, and rotational effects (Farmer et al. 2009, Li & Farmer 2011). ISW fission is ubiquitous when the waves approach the shelf break, where ISW packets with multiple waves are spawning, as shown in Figure 1.3. Wave deformation is expedited when further progressing above the shelf, with the emergence of wave polarity reversal somewhere in the shallow water (Orr & Mignerey 2003). Eventually, the waves fully break and dissipate in the northern SCS margin, marking the end of the life cycle (Figures 1.2 and 1.4).

1.2 Up-to-date investigation of baroclinic tides in the northern South China Sea

1.2.1 Background

As was introduced above, internal wave study in the northern SCS has been a hot topic in the last decade. The origin of the waves is due to the interaction of barotropic tides with the steep topographic features in the LS. In this section internal wave dynamics in this region will be reviewed.

The LS (Figure 1.2), which is located west of the Pacific Ocean, plays an important role in the dynamics of the SCS. It is a gateway connecting the SCS and the western Pacific Ocean.

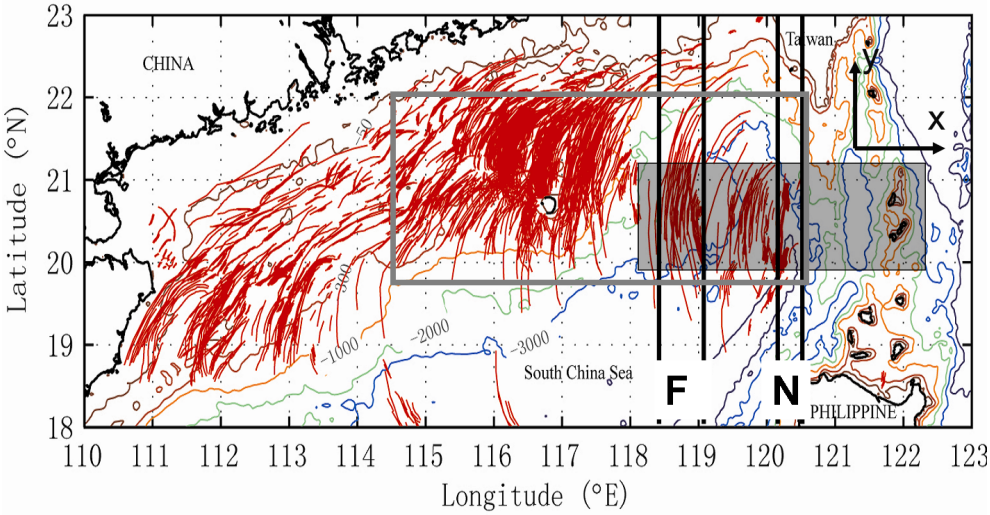

Figure 1.3: Radar signatures of ISWs (red lines) compiled from a set of 344 European remote sensing satellite (ERS) Synthetic Aperture Radar (SAR) and Envisat Advanced Synthetic Aperture Radar (ASAR) images acquired between 1995 and 2007 (courtesy of Weigen Huang). The smaller shaded grey rectangle is the modelling domain of wave generation (Chapter 4). The larger grey rectangle denotes the modelling domain of wave shoaling (Chapter 8). The two meridional bands marked by 'N' and 'F' are the regions where some short internal waves appear (Chapter 5).

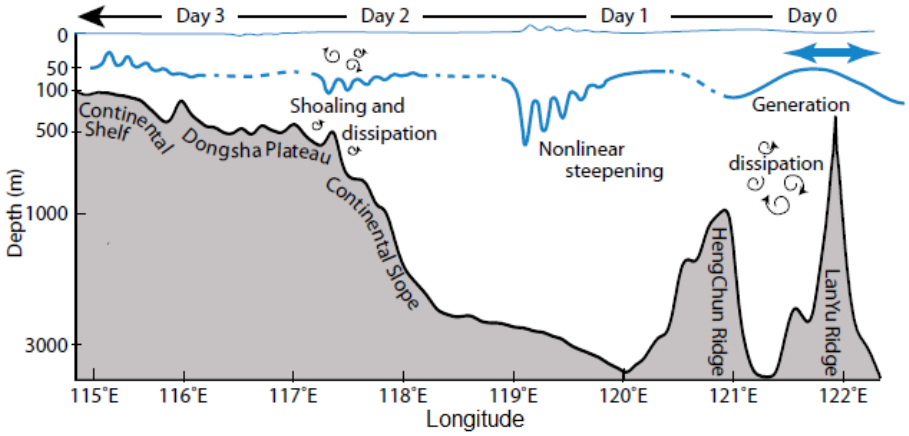

Figure 1.4: Schematic showing the life cycle of an ISW from its origin at LS to its dissipation in the northern SCS margin (figure adopted from Simmons & Alford (2012)).

The most prominent feature of the bathymetry in the LS is two steep meridional ridges. The eastern ridge is relatively higher and is thought to be the primary source for the generation of large amplitude ISWs due to intense tide-topography interactions, while the western ridge is not that efficient in generating ISWs due to its greater depth, but it also contributes somehow to the formation of ISWs in the northern SCS (Vlasenko et al. 2010, Buijsman et al. 2012).

Barotropic tides in the LS feature a fortnightly modulation with a mixture of both diurnal and semidiurnal tidal components. Numerical experiments on barotropic tides in the LS (Jan et al. 2008) showed that four principal harmonics, O_1, K_1, M_2 and S_2, constitute the complex barotropic tide structure there, with the first three components dominating. Figure 1.5 shows one month's zonal velocity data in April-May, 2007 at one point ($20.6^\circ N$, $122.0^\circ E$) between Itbayat Island and Batan Island. It is clear in the figure that barotropic tides at this site are highly asymmetric with much stronger ebb (eastward) tides than flood (westward) tides. When decomposing the total tides into semidiurnal (M_2, S_2) and diurnal (K_1, O_1) components, it can be seen that during the spring phase the diurnal part dominates (Figure 1.5c) while in the neap phase the semidiurnal counterpart is much more prominent (Figure 1.5d). The shape of the tidal curve shown in Figure 1.5 features one strong eastward peak and two westward peaks (one stronger, one weaker) on certain days, and is typical of the barotropic tides in the LS, although the ever-changing phase between diurnal and semidiurnal components can lead to slight changes of the overall tides. The resultant asymmetry of the barotropic forcing from multiple tidal harmonics in the LS brings about the so-called A and B ISWs observed in the northern SCS (Ramp et al. 2004).

The Kuroshio is a very intense western boundary current (velocity $\sim$ 1 m/s) originating from the North Equatorial Current. Its flow patterns and characters have significant impacts on the hydrological environment in the SCS. Several manifestations have been identified when the Kuroshio passes by the LS (Liu et al. 2008): the main stream flowing northward between the two ridges and along the east flank of the eastern ridge without intrusion into the SCS; the intrusion of a branch; the formation of a "loop" style circulation, i.e., the main stream intruding into the SCS through the southern and middle reaches of the LS, meandering clockwise, and flowing out in the northern reach of the LS. Yuan, Han & Hu. (2006) argued that this anticyclonic intrusion of Kuroshio, accompanied by active eddy-shedding, is a transient process rather than a persistent one. As is known, the superposition of the Kuroshio on the tidal flows in the LS complicates the situation of internal wave generation in the northern SCS and clouds our understanding of this problem. There have been quite a few numerical efforts to look into this issue (Du et al. 2008, Warn-Varnas et al. 2009, Buijsman, McWilliams & Jackson 2010, Li & Farmer 2011, Jan et al. 2012). However, The understanding of this is, to a large extent, incomplete, presumably because the understanding of the Kuroshio characteristics and water exchange at LS is not very clear. The results indicate that the Kuroshio does affect the wave generation but it does not play a substantial role. Current studies mostly remain superficial and are of a qualitative nature, and controversy remains about if the Kuroshio favors or undermines the wave generation at LS.

Oceanic stratification is crucial to internal wave properties. In the northern SCS, monthly-averaged climatological temperature/salinity dataset World Ocean Atlas (2009) shows more or less spatial homogeneity but exhibits obvious seasonal variation (Figure 1.6). Maximum buoyancy frequency in summer is located around -100 m and can reach as large as 0.017 $rad\ s^{-1}$, while in winter the stratification is somehow weaker owing to the existence of a larger upper mixed layer caused by the winter monsoon. In addition, stratification exhibits spatial variation

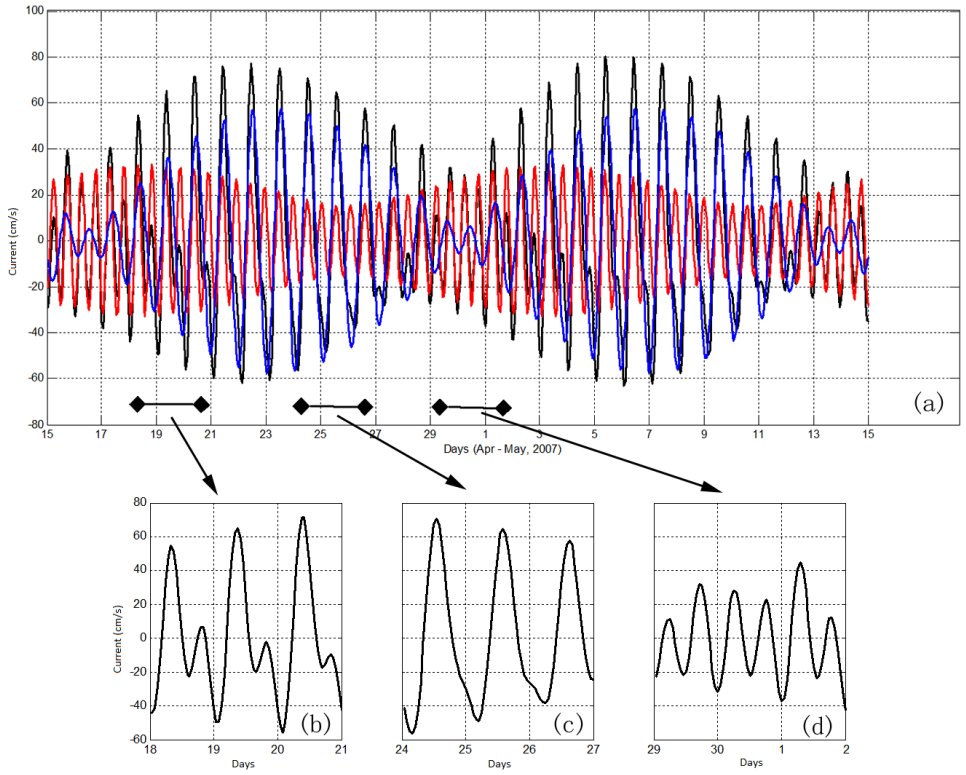

Figure 1.5: a) Zonal velocity from 15th April to 15th May, 2007 at 20.6°N, 122.0°E in the LS. The black line is the overall tide (including M_2, S_2, K_1, and O_1 harmonics), whereas the red and the blue lines are the semidiurnal and diurnal components, respectively. Meridional currents in the LS are weak. b), c), and d) are three time periods featuring mixed tides, diurnal-dominant tides, and semidiurnal-dominant tides, respectively.

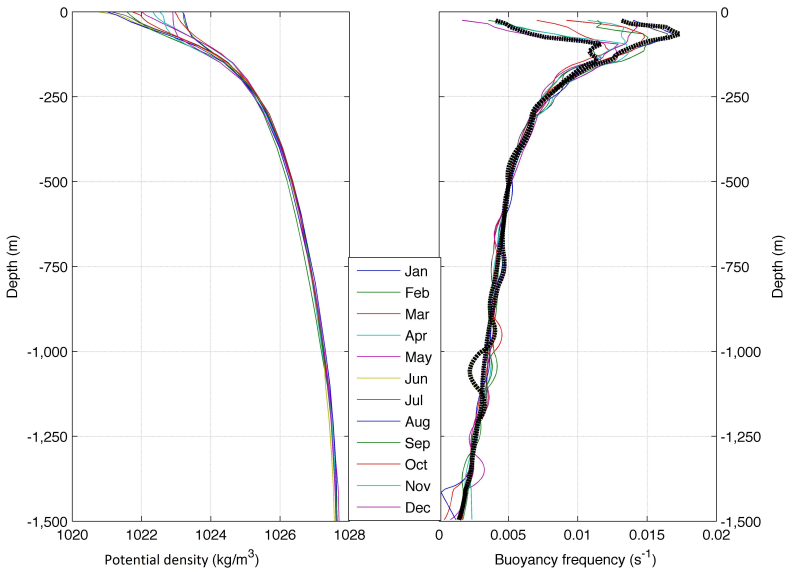

Figure 1.6: Climatologically averaged monthly density (left) and buoyancy frequency (right) profiles in the northern SCS. Data is from World Ocean Atlas (2009). The two thick dashed lines in the right panel indicate weakest pycnocline with thickest mixed layer in January, and strongest pycnocline with thinnest mixed layer in June, respectively.

on the two sides of the LS (Shaw et al. 2009), which is one of the factors that contribute to the lesser occurrence of ISWs east of the LS (Buijsman, McWilliams & Jackson 2010). As a consequence of the change of stratification, both satellite imagery (Zheng et al. 2007) and in situ measurements (Ramp et al. 2010) have revealed significant seasonal and inter-annual variations, with lesser occurrence of events in winter. Nonetheless, some numerical efforts (Li 2010, Vlasenko et al. 2010) demonstrate that the amplitudes of ISWs generated in winter are no smaller than those in summer.

1.2.2 Investigation approaches

Three major approaches are employed to investigate internal wave dynamics in the northern SCS: satellite images, in situ observations, and numerical simulations. All these three methods are indispensable and supplementary to each other.

1.2.2.1 Satellite images

Visualization of ISWs on SAR images is very straightforward. One can clearly identify the location, propagating direction, along-crest width, number of waves in one packet, and even wave amplitude through some theoretical methods (Zheng et al. 2001). Figure 1.7 shows three Envisat ASAR images featuring ISWs near the LS, in the deep basin, above the shelf break, and on the continental shelf. A packet containing five ISWs (fragment c) shows up just west of the western ridge. Fragment b features two extraordinarily large ISW packets in the deep basin and near the shelf break. The packet in the deep basin has an along-crest width of nearly 300 km and is among the widest ever observed. The two consecutive packets are 127.6 km apart, which corresponds to the wavelength of a semidiurnal internal tide above that depth. Five

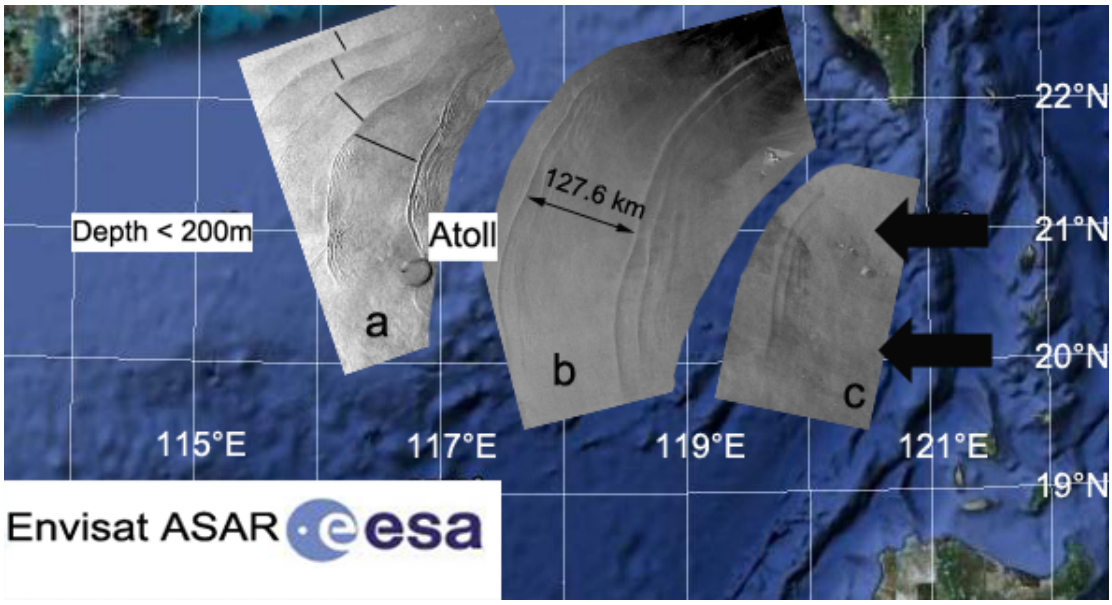

Figure 1.7: Three Envisat ASAR images compiled in one map showing: a) ISW packets on the shallow continental shelf (21-JUN-2005, 14:09 UTC); b) ISW packets near the shelf break and in the deep basin (12-AUG-2006, 14:04 UTC); c) ISW packet in the deep basin but near the LS (11-AUG-2006, 01:50 UTC). The arrow and the number in b) indicate the distance between the two consecutive ISW packets. The four black lines in a) show the decreasing distance between two neighboring packets when shoaling onto the shelf.

ISW packets, with decreasing distance between the neighboring two and which are significantly deflected northward, are present in fragment a. Wave refraction by the Dongsha Atoll can be seen, and wave surface signals are getting weaker further north.

The first study of ISW in this area using satellite images was conducted by Fett & Rabe (1977), and in more recent years their application has revived, with an increasingly widespread use (Hsu et al. 2000, Liu & Hsu 2004, Zhao et al. 2004, Zheng et al. 2007, Huang et al. 2008, Jackson 2009). These authors compiled maps of the spatial distribution of ISWs from many years (see also Figure 1.3) and obtained statistics that intuitively show the wave characteristics in this region. However, one should bear in mind that although the spatial resolution and coverage of many satellite images are very satisfying, they are restricted by long temporal sampling intervals, which makes the study of ISWs with sequential images impossible, given that most oceanic surface features (like ISWs) have relatively much shorter coherent time periods. Apart from that, satellite images are also of limited value for characterizing interior wave structures and the associated motions.

1.2.2.2 In situ measurements

In situ measurements of ISWs in the northern SCS were first reported about two decades ago (Ebbesmeyer et al. 1991, Bole et al. 1994), but only in recent years has much advance been made by both the deployment of extensive long-term moorings and shipboard measurements (Orr & Mignerey 2003, Ramp et al. 2004, Duda et al. 2004, Lien et al. 2005, Chang et al. 2006, Liu et al. 2006, St. Laurent 2008, Farmer et al. 2009, Li et al. 2009, Yang et al. 2009, Alford

et al. 2010, Ramp et al. 2010, Alford et al. 2011, Klymak et al. 2011, Li & Farmer 2011). The observational sites are located not only in the LS and the deep water of the northern SCS, but also on the continental slope and shelf.

The SCS component of the very large field experiment Asian Seas International Acoustic Experiment (ASIAEX) was carried out during 2000 and 2001. Some moorings were anchored on the shelf of the northern SCS and recorded ISWs periodically passing by. Although constrained by the small observational area and short duration, ASIAEX is the first large-scale in situ research on ISWs in the SCS, and it brought up a number of publications (Orr & Mignerey 2003, Ramp et al. 2004, Duda et al. 2004, Yang et al. 2004, Zhao & Alford 2006, Duda & Rainville 2008), which has provided considerable insight into our understanding of ISW dynamics in the northern SCS. An important finding from ASIAEX is the A and B ISWs (Ramp et al. 2004). ISWs belonging to type A have larger amplitudes and arrive at the moorings regularly with a period of 24 hours, while the B ISWs are relatively weaker and arrive about one hour later every day. Zhao & Alford (2006) analyzed the arrival times of ISWs at two moorings, and related them to the tidal forcing over Lan-Yu Ridge in the middle LS. The comparisons showed that every ISW packet can be associated with a westward current peak in the LS rather than an eastward one, which implies that the packets of ISWs are produced due to nonlinear steepening of internal tide. During ASIAEX, moored records (Duda et al. 2004, Yang et al. 2004) and shipboard measurements (Orr & Mignerey 2003) also observed wave polarity transitions from waves of depression to elevation resulting from the shoaling topography of the continental slope, corroborating findings from satellite images (Zhao et al. 2003). Yang et al. (2004) also reported the recording of a second mode ISW.

After ASIAEX, a few subsequent surveys followed, which were mostly Taiwan/US joint programs. Such experiments include: 1) Variations Around the Northern South China Sea (VANS) and the Windy Islands Soliton Experiment (WISE) (Yang et al. 2010, Ramp et al. 2010), which had four moorings deployed across the northern SCS (two in the deep basin, one on the upper continental shelf, and one in the LS) and obtained more than one year's high-resolution observations of temperature, salinity, and velocity; 2) Nonlinear Internal Waves Initiative (NLIWI) (Alford et al. 2010). Ten moorings, including Pressure Inverted Echo Sounders (PIES), ADCP moorings and profiling moorings, were deployed during 2006-07, and recorded 14 nonlinear ISWs as they passed by the synchronous array of these ten moorings from the LS to the shelf; 3) Internal Waves in Straits Experiment (IWISE) (Alford et al. 2011). Two lines of short-term observational stations were deployed across the middle and the southern reaches of the LS in 2010. Alford et al. (2011) presented some first observational studies of the internal tide generation and dissipation dynamics at the LS.

Apart from large-scale experiments, some short-term surveys were conducted above the slope-shelf area of the northern SCS (Chang et al. 2006, St. Laurent 2008, Klymak et al. 2011). It was found that most of the energy has already been dissipated before the waves reach the continental shelf, and a dissipation rate of $O(10^{-7} - 10^{-6})Wkg^{-1}$ was estimated, indicating that the northern SCS margin is a very dissipative area. Klymak et al. (2011) measured a beam-like structure impacting the continental shelf, rather than a more simple and common first baroclinic mode intrusion. Decomposition of the measured signals showed a multi-modal structure, with both diurnal and semidiurnal characteristics, and pronounced wave reflection occurred for diurnal waves due to the supercritical slopes.

1.2.2.3 Numerical simulations

Complementary to these satellite and in situ observational developments have been advances in numerical simulations of ISWs in this area. A number of models, which vary from 2D, two-layered, ideal, classic weakly nonlinear solutions to 3D, continuous layer, realistic, fully nonlinear and nonhydrostatic configurations, have been developed to investigate ISWs in the northern SCS (Cai et al. 2002, Du et al. 2008, Farmer et al. 2009, Shaw et al. 2009, Warn-Varnas et al. 2009, Buijsman, Kanarska & McWilliams 2010, Vlasenko et al. 2010, Li & Farmer 2011, Zhang et al. 2011, Buijsman et al. 2012). Most of the models focused on the generation in the LS and evolution in the deep water, and discussed how waves are influenced by factors like bathymetry, stratification, tidal forcing, Kuroshio intrusion, etc. However, most models have some limitations in one way or another which render them less likely to accurately model wave activities in this region. Such shortcomings like 2D modeling, hydrostatic approximation, ideal bathymetry and stratification, etc., are commonly seen for simplification.

While most models are 2D ones, attempts to employ 3D models have been made in recent years (Vlasenko et al. 2010, Zhang et al. 2011). Zhang et al. (2011) used the parallel, unstructured grid model SUNTANS (Fringer et al. 2006), which solves the fully nonlinear, nonhydrostatic Navier-Stokes equations, to study the ISW generation and propagation in thie region. The whole LS and the northern SCS continental slope were covered in the model domain, and realistic forcing was included to drive the model during a fortnight run. Qualitative comparisons with in situ measurements and satellite imagery show good similarity, demonstrating the capability of the model to simulate internal wave dynamics in this whole domain. Considerable attention was given in spatial and temporal characteristics of the generation and propagation of A and B ISWs.

Some modeling efforts were also put to investigate properties of internal tides near the LS with 3D hydrostatic Princeton Ocean Model (POM) (Niwa & Hibiya 2004, Jan et al. 2007, 2008, Zu et al. 2008). Wave dynamics like baroclinic wave flux, conversion rate and energy balance for different tidal harmonics were calculated and the results showed that both diurnal and semidiurnal internal tides are very active at LS, and pronounced isopycnal disturbances are registered in the far field.

1.2.3 Internal wave generation at LS

It has been widely acknowledged that the middle LS (i.e., around the Batan Islands) is the primary region for the generation of large amplitude ISWs in the northern SCS, while the rest of the strait generates comparatively weak waves. In situ observations (Alford et al. 2011) and numerical simulation (Jan et al. 2008) have shown that very strong energy conversion and energy flux occur here. However, the other two regions, i.e., the southern reach of the LS (the Babuyan Islands) and the northern part of the western ridge, although not that efficient, are also believed to be able to produce significant baroclinic signals (Hsu et al. 2000, Jan & Chen 2009, Alford et al. 2011). Internal waves radiating from different sources at the same time can meet and nonlinearly connect very rapidly with each other and propagate westward together (Cai & Xie 2010, Chen et al. 2011).

Inconsistent conclusions have been reached in terms of the generation process and mechanism of ISWs in the LS, presumably due to the intricate bottom topography and various oceanic dynamics there. Generation mechanisms proposed include lee wave mechanism (Cai et al. 2002), internal tide evolution mechanism (Lien et al. 2005, Zhao & Alford 2006, Warn-Varnas

et al. 2009, Vlasenko et al. 2012), western boundary current instability generation mechanism (Yuan, Zheng, Dai, Hu, Qiao & Meng. 2006), internal mixing disturbance mechanism (Du et al. 2008), tidal beam-thermocline interaction mechanism (Shaw et al. 2009), and mixed lee wave mechanism (Buijsman, Kanarska & McWilliams 2010).

1.2.4 Evolution in the deep basin and shoaling process in the shallow water

After internal waves are produced in the LS, they will propagate westward or northwestward in the deep basin. Both in situ measurements (Alford et al. 2010, Farmer et al. 2009) and SAR images (Zhao et al. 2004, Jackson 2009) reveal that ISWs have already well formed in the deep basin before they reach the shoaling continental slope (see Figure 1.3). Normally there exists only one single wave in a packet, while multi-wave packets emerge near the shelf break.

Internal tides are progressively shaped by nonlinear and rotational effects after propagating out of the source area. ISWs are formed under the continuous steepening of internal tides when non-hydrostatic effects come into play and rotation can be ruled out. These effects on the ISWs in the northern SCS were examined by Farmer et al. (2009), Li & Farmer (2011). They investigated the rotational effects in the northern SCS by comparing measured time series and modeled results with and without rotation. It was found that ISWs are much more developed without the presence of rotation, and in such a case they have larger amplitude, more waves, and arrive later than the observed waves.

When reaching the shallower margin of the northern SCS, internal wave signals, which include both high-frequency ISWs and long internal tides, interact strongly with the shoaling topography. Much of the internal tides from the LS disintegrate into ISWs at the steepening wave trough. The incident wave energy scatters upon the shoaling topography, either going further upslope, being partially reflected, or being locally dissipated. Of the strong transmitted wave energy onto the continental slope and shelf, a great proportion is locally dissipated near the shelf break (Lien et al. 2005, Chang et al. 2006, St. Laurent 2008, Klymak et al. 2011). Pronounced near-bottom isopyncal fluctuations with spring-neap cycles were measured, accompanied by a high rate of turbulent dissipation (Klymak et al. 2011). As a consequence, much of the incoming internal tidal energy originating from the LS has been lost before the waves could reach the shallow continental shelf.

Before introducing properties of internal tides or ISWs in shallower water, a point worth mentioning is the reflection and diffraction effect of the Dongsha Atoll, which is located at about $116°45'E$, $20°40'N$, right in the propagation path of ISWs from the LS. The Dongsha Atoll is featured by steep slopes around it and is connected to the deep sea on the east and the continental shelf on the west, respectively. When large amplitude ISWs of first mode or second mode impinge on the Dongsha Atoll, one wave will be broken apart into two fragments, which separately bypass the atoll and rejoin behind it. The process is accompanied by the generation of secondary waves and backward reflection, which makes the wave field become very complicated in the vicinity of the atoll. Figure 1.8 shows an ASAR image in which multiple dynamic processes related to ISWs can be seen: the ISW packets being refracted by the atoll, a weak reflected ISW, intricate wave-wave interaction between the previously refracted ISWs and incoming ISWs further north formed in the next cycle, and weak ISW packets shoaling onto the continental shelf.

Based on four mooring sites upon the shallow continental slope during ASIAEX, Duda & Rainville (2008) found that diurnal energy flux onto the shelf was greater than that measured at

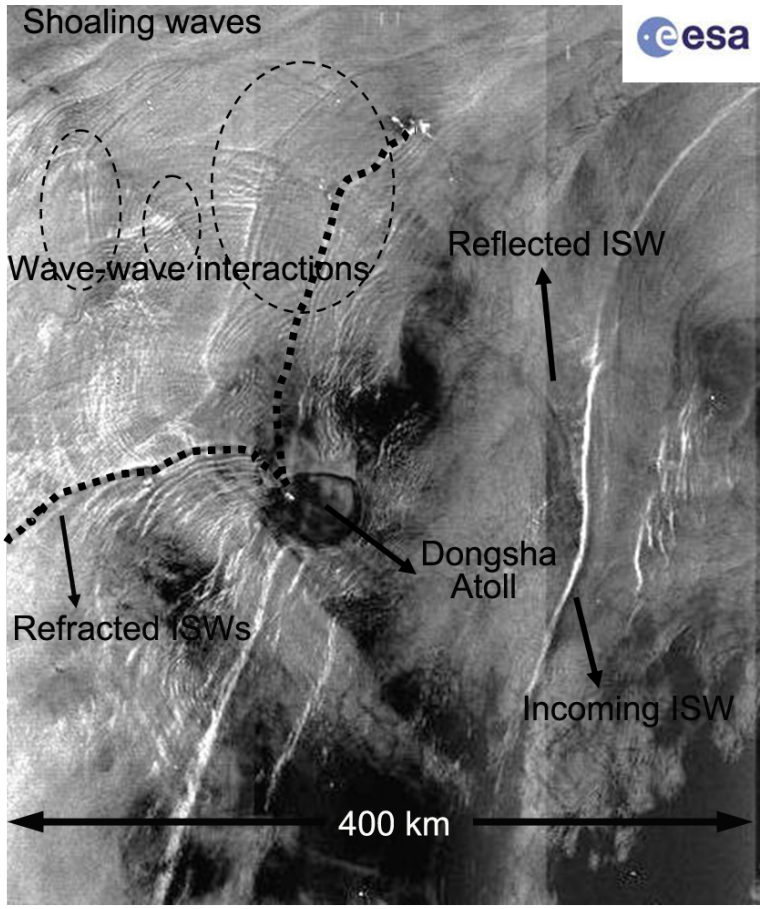

Figure 1.8: An Envisat ASAR image (03-NOV-2005, 14:15 UTC) showing the complicated wave field near the Dongsha Atoll. Incoming ISWs, refracted multi-wave packets, reflected single ISW, wave-wave interactions, and shoaling waves can be clearly spotted on the image. The two dashed lines indicate the position of the leading wave in the refracted ISW packet. The dashed ellipses show where pronounced wave-wave interactions take place.

the deeper site, whilst semidiurnal flux decreased monotonically upslope. This somehow implies the likelihood of local generation of diurnal internal tides, which originate from barotropic tide-topography interaction at this area. According to the calculation of the internal wave ray characteristic angles for both diurnal O_1 and semidiurnal M_2 tides (Duda et al. 2004), critical slopes for the diurnal tide in this region are 0.16 to 0.3 degree, much shallower than those for the semidiurnal tide, which are of the order 0.5 to 1 degree (similar estimation was also given by Klymak et al. (2011)). Considering that the shallower slopes that are critical for diurnal tides are very typical, this area is suitable for diurnal tidal generation rather than semidiurnal. Further interpretation was made by Duda & Rainville (2008), with more details and robust observational data. Meanwhile, Klymak et al. (2011) addressed that such critical nature of the northern SCS margin to the diurnal internal tides implicates the effect of internal tides in shaping the continental shelf.

In addition, complexity is also added by the correlation between the remotely generated shoaling internal tides and the local barotropic tides (Kelly & Nash 2010), which has great impact on the local energy conversion of barotropic to baroclinic tides and thus affects the subsequent characteristics of baroclinic waves and the incoming ISWs. A further complicating factor is that the dominant diurnal internal tides can somehow modulate the propagation of incoming ISWs, as was interpreted by Alford et al. (2010) who, by solving the Taylor-Goldstein equation which takes into account the background shear process (diurnal internal tides in this case), found that upon the upper continental shelf B waves moved faster than A waves, although the latter have larger amplitudes.

With further decrease of water depth, ISWs will finally reach the turning point where, theoretically, waves of elevation type start to take shape if the inclination of the slope is not large enough to induce wave breaking. In the northern SCS, measurements during ASIAEX have illuminated many fascinating results on the transformation processes of the incident waves. Such features were extensively studied by Duda et al. (2004), Ramp et al. (2004), who showed that beginning as large narrow ISWs of depression, they became much broadened when shoaling onto the continental shelf, accompanied by the trailing of oscillations and subsequent emergence of waves of elevation. Yang et al. (2004) reported four forms of ISWs during this process, including the near-breaking stage when they were in the transition zone that was very close to the temporally varying turning point. Two more intriguing polarity conversion events were presented by Orr & Mignerey (2003) with shipboard measurements in the ASIAEX area. Visualization of the acoustic flow from waves of depression to elevation is quite illustrative, and wave properties like position and width were described during the shoaling process to the shallower water.

Generated waves of elevation either break up or are dispersed depending on the changes of water depth and local stratification, which marks the termination of the life cycle of an ISW from its origin in the LS. Breaking internal waves at the shelf break and on the shallow shelf may be the primary source for turbulent mixing, which can effectively weaken the stratification and affect the local dynamic processes. 3D numerical efforts with realistic conditions have been lacking except one study by Shen et al. (2009), who simulated the shoaling process of ISWs in the ASIAEX area.

1.3 Motivations and aims

Investigation in the last decade has emphasized the significance of internal waves in the northern SCS. They have drawn much concern not only due to their large scales and regular occurrence,

but also for marine operational reasons. Although this phenomenon has been intensively studied, some issues still remain incomplete, for example, how are the waves generated and radiated in the LS, especially with a complex 3D bathymetry? What factors have the most significant influence on the generation and propagation of internal waves in this region? How do the waves evolve above the wide shoaling continental slope-shelf after taking shape in the deep water? And what role does the 3D topography and rotation play in such a process?

This dissertation aims to, basically by means of numerical modelling, explore characteristics of internal wave dynamics in the northern SCS which, specifically, consists of a complete understanding of:

- 3D generation processes and mechanisms of internal waves at LS, with a highlight of 3D modeling and the generated wave structures of multiple modes.
- the role played by various factors that determine the resultant wave fields; such factors include western ridge interference, asymmetric barotropic tides, rotational effects, etc.
- the wave shoaling process over the wide northern SCS slope and shelf that involves the evolution of both a first mode and a second mode ISW and addresses the effects of 3D topography and rotation.

To achieve this seemingly ambitious goal, the 3D Massachusetts Institute of Technology general circulation model (MITgcm), which features fully nonlinear, nonhydrostatic capacities, serves as the main tool to accomplish the numerical experiments. Model results are supported and corroborated by the classic weakly nonlinear theories, SAR imagery, and limited in-situ measurements.

1.4 Thesis outline

The structure of this dissertation is arranged as follows:

- Chapter 2 first looks back at the linear internal wave and internal tide generation problem. Nondimensional parameters that modulate the generation regimes and characteristics are listed and interpreted. Second, classic KdV theory and fully nonlinear theory of ISWs are briefly summarized. Third, the progress of internal wave dynamics in the northern SCS is reviewed.
- Chapter 3 begins with a briefing of MITgcm, followed by an introduction of SAR.
- Chapter 4 is the core section of the dissertation, viz., 3D modelling of ISW generation mechanism and process near the LS. Model setup, results, and some sensitivity experiments are presented, and this part serves as a foundation and starting point for the next few chapters.
- Chapter 5 focuses on a particular phenomenon that is delineated in Chapter 4: a specific structure of 'first mode ISW followed by a second mode ISW, on which some short first mode IWs ride'. A series of SAR images are analyzed and compared to the model results, and a robust consistency is reached.

- Chapter 6 emphasizes the role that played by the irregular and multi-harmonic barotropic tidal constituents in the LS and the resultant altering of ISW field. An alternation of A and B ISWs (as will be defined later) and a mutual transition are simulated, with the verification from both in-situ measurements and analytical linear formulations.
- Chapters 7 and 8 form the other key point of the dissertation: ISW shoaling process over the northern SCS slope and shelf. Chapter 7 tentatively studies the evolution of a second mode ISW over a two-dimensional (2D) shoaling slope that is typical of the northern SCS bathymetry, whereas in Chapter 8 experiments of a first mode ISW over realistic 3D bottom are performed, with emphases on the rotational and topographic effects on the shoaling wave profiles.
- Chapter 9 presents the summary and conclusions.

Chapter 2

Theoretical background

2.1 Linear internal wave theory

Internal waves can be treated as a perturbation of a background static state that only varies vertically,

$$p = p_0(z) + p'(x,y,z,t) \tag{2.1}$$

$$\rho = \rho_0(z) + \rho'(x,y,z,t) \tag{2.2}$$

where p and ρ are pressure and density, respectively. The fields with a prime denote the motion of internal wave. The background fields $p_0(z)$, $\rho_0(z)$ satisfy the hydrostatic balance:

$$\frac{dp_0}{dz} = -\rho_0 g \tag{2.3}$$

where g is the acceleration due to gravity.

The linearized Euler equations with the Boussinesq approximation in a continuously stratified fluid read

$$\frac{\partial u}{\partial t} - fv = -\frac{1}{\rho_*}\frac{\partial p'}{\partial x} \tag{2.4a}$$

$$\frac{\partial v}{\partial t} + fu = -\frac{1}{\rho_*}\frac{\partial p'}{\partial y} \tag{2.4b}$$

$$\frac{\partial w}{\partial t} = -\frac{1}{\rho_*}\frac{\partial p'}{\partial z} + b \tag{2.4c}$$

$$\frac{\partial u}{\partial x} + \frac{\partial v}{\partial y} + \frac{\partial w}{\partial z} = 0 \tag{2.4d}$$

$$\frac{\partial b}{\partial t} + N^2 w = 0 \tag{2.4e}$$

where $\mathbf{u} = (u,v,w)$ is the (perturbed) velocity field; ρ_* is a constant reference quantity; b is the buoyancy defined as

$$b = -g\rho'/\rho_* \tag{2.5}$$

f is the Coriolis frequency, and N is the buoyancy frequency defined as

$$N^2(z) = -\frac{g}{\rho_*}\frac{d\rho_0}{dz} \tag{2.6}$$

The five equations of (2.4) can be reduced to a single equation for w which reads

$$\frac{\partial^2}{\partial t^2}\nabla^2 w + N^2\nabla_H^2 w + f^2\frac{\partial^2 w}{\partial z^2} = 0 \tag{2.7}$$

where the Laplace operator ∇^2 and its horizontal component ∇_H^2 read

$$\nabla^2 = \frac{\partial^2}{\partial x^2} + \frac{\partial^2}{\partial y^2} + \frac{\partial^2}{\partial z^2} \tag{2.8a}$$

$$\nabla_H^2 = \frac{\partial^2}{\partial x^2} + \frac{\partial^2}{\partial y^2} \tag{2.8b}$$

An energy equation can be derived by manipulating equations (2.4):

$$\frac{1}{2}\rho_*\frac{\partial}{\partial t}[u^2 + v^2 + w^2 + b^2/N^2] + \mathbf{u}\cdot\nabla p' = 0 \tag{2.9}$$

The energy density E, which is the sum of kinetic and potential energy, is

$$E = \frac{1}{2}\rho_*[u^2 + v^2 + w^2 + b^2/N^2] \tag{2.10}$$

The term $\mathbf{u}\cdot\nabla p' = \nabla\cdot(\mathbf{u}p')$ in equation (2.9) denotes the divergence of the energy flux. Upon integrating equation (2.9) over a certain volume, it can be shown that the temporal variation of the total energy (kinetic and potential) is balanced by the fluxes through coming in/out of the faces of the volume.

Supposing the wave is temporally sinusoidal with a frequency ω, i.e.,

$$w(x,y,z,t) = \bar{w}(x,y,z,t)exp(-i\omega t) \tag{2.11}$$

Substituting it into equation (2.7), the following equation can be derived

$$\nabla_h^2\bar{w} - \frac{\omega^2 - f^2}{N^2 - \omega^2}\frac{\partial^2\bar{w}}{\partial z^2} = 0 \tag{2.12}$$

Without loss of generality, taking $\partial/\partial y = 0$, equation (2.12) can be written as

$$\bar{w}_{xx} - \frac{\omega^2 - f^2}{N^2 - \omega^2}\bar{w}_{zz} = 0 \tag{2.13}$$

The dispersion relation can be obtained by substituting $\bar{w} \sim exp\ i(kx + mz)$ into (2.13),

$$\omega^2 = \frac{N^2}{K^2}k^2 + \frac{f^2}{K^2}m^2 \tag{2.14}$$

where $K = \sqrt{k^2+m^2}$ is the length of the wavevector. The above expression can be formulated in polar coordinates, assuming $\mathbf{k} = (k,m) = K(cos\theta, sin\theta)$, where θ is the angle between the wavevector and its horizontal component. Then 2.14 becomes

$$\omega^2 = N^2 cos^2\theta + f^2 sin^2\theta \tag{2.15}$$

An important conclusion follows from the linear dispersion relation of internal waves, that is, the phase velocity $\mathbf{c}_p = \frac{\omega}{\mathbf{k}}$ is perpendicular to the group velocity $\mathbf{c}_g = \frac{\partial\omega}{\partial\mathbf{k}}$, i.e.,

$$\mathbf{c}_p \cdot \mathbf{c}_g = 0 \tag{2.16}$$

Equation (2.13) can be solved in two approaches: the method of characteristics and the method of vertical modes. The latter method requires a surface and a bottom boundary. For the latter, assume $\bar{w} = W(z)exp\ ikx$, and substitute it into (2.13), it gives

$$W_{zz} + k^2\frac{N^2(z)-\omega^2}{\omega^2-f^2}W = 0 \tag{2.17a}$$

$$W = 0 \quad z = 0, -H \tag{2.17b}$$

This is a Sturm-Liouville problem. Its solution consists of a series of eigenvalues k_n and the corresponding eigenfunctions W_n. For some special profiles of $N(z)$, W_n can be obtained analytically, otherwise the equation has to be solved numerically.

After obtaining W, the other variables, u, v, p, and b can be expressed similarly, following equations (2.4),

$$U = \frac{i}{k}W';\ V = \frac{f}{\omega k}W';\ P = i\rho_*\frac{\omega^2-f^2}{\omega k^2}W';\ B = -\frac{iN^2}{\omega}W \tag{2.18}$$

A simple and special case lies in the assumption of uniform stratification, i.e., $N = const$. In this case the solution of (2.17) is obvious and it takes the simple form of

$$W_n = sin(\frac{n\pi z}{H}) \qquad n = 1,2,3,\cdots \tag{2.19}$$

which is independent of ω with $N = const$. The dispersion relation is

$$k_n = \pm\frac{n\pi}{H}(\frac{\omega^2-f^2}{N^2-\omega^2})^{1/2} \qquad n = 1,2,3,\cdots \tag{2.20}$$

which can be rewritten as

$$\omega^2 = \frac{N^2k^2 + f^2(\frac{n\pi}{H})^2}{k^2 + (\frac{n\pi}{H})^2} \qquad n = 1,2,3,\cdots \tag{2.21}$$

The corresponding phase velocity c_p and group velocity c_g can then be subsequently derived.

2.2 Internal tide generation

Internal waves in the ocean mainly originate from the wind and the barotropic tide (Wunsch & Ferrari 2004, Simmons & Alford 2012). The former generates near-inertial internal waves (Alford 2001, Garrett 2001, Alford 2003), whereas the latter generates internal tides, which are the topic of this section. Internal tides, or baroclinic tides, are internal waves of tidal frequency, which are generated in stratified oceans by the interaction of barotropic tides with topographic features as underwater ridges, banks, seamounts, continental slope, etc. Unlike barotropic tides, internal tides can cause very large vertical displacement of density surfaces inside the ocean, which can reach tens or even hundreds of meters.

Some early theories of internal tide generation in the abyssal ocean were established several decades ago (Baines 1973, Bell 1975*a*,*b*), but understanding of its role in the real ocean was incomplete. However, this topic has lately received considerably wide interest in view of the availability of observation of satellite altimetry (Egbert & Ray 2000) and the recognition that internal wave breaking could play a significant role in determining the global energy flux budget and large scale ocean circulation (Munk & Wunsch 1998, Wunsch & Ferrari 2004). Garrett & Kunze (2007) gave a general review of the recent theoretical, observational, and numerical developments.

2.2.1 Generation regimes and models

Following Garrett & Kunze (2007), there are several non-dimensional parameters that define the regimes of internal wave generation. The dimensional parameters employed are three frequencies, ω, f, N, topographic height h_0 and horizontal scale k^{-1}, water depth H, and the current magnitude u_0.

The first parameter, ku_0/ω, is the tidal excursion parameter that is defined by the ratio of the tidal excursion u_0/ω to the topographic horizontal scale k^{-1}. The second parameter, ε, is a steepness parameter that is defined as $\varepsilon = kh_0/\alpha$, where kh_0 is the steepness of the topography, and $\alpha = \sqrt{(\omega^2 - f^2)/(N^2 - \omega^2)}$ is the slope of the internal tide characteristic. $\varepsilon < 1$, $\varepsilon = 1$, and $\varepsilon > 1$ are referred to as subcritical, critical, and supercritical slopes, respectively. These two parameters are the two most important ones, and will be elaborated below. The other parameters involve the frequency ratios, ω/f, ω/N, and a height ratio, h_0/H.

Figure 2.1 illustrates the parameter space based on ku_0/ω and ε. Five regimes are sketched in the figure. Regimes 1 and 2 correspond to the 'weak topography' limit of Bell's linear theory of internal tide generation (Bell 1975*a*). The topography slope is assumed to be small in an infinitely deep ocean, but there is no restriction on the magnitude of the tidal excursion. For small ku_0/ω (acoustic limit; regime 1), internal tides are mainly excited at the tidal frequency ω, whereas contributions from higher harmonics increase with larger finite excursion (regime 2). Very large value of ku_0/ω corresponds to the lee-wave regime.

On the other hand, for small ku_0/ω but finite ε (regime 5), which implies a weak flow and steep topography regime, the scenario is different, that is, while the frequency ω of the gener-

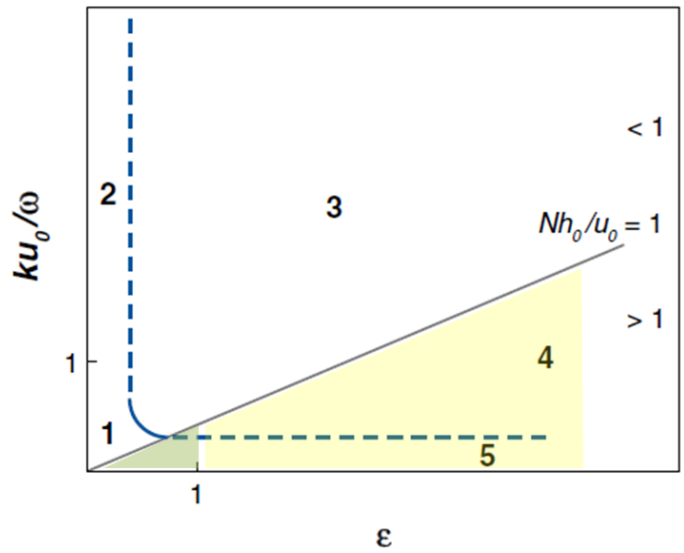

Figure 2.1: The parameter space characterized by ku_0/ω and ε. The solid line denotes $Nh_0/u_0 = 1$ and is explained in the text. This figure is adopted from Garrett & Kunze (2007). The green shading and the yellow shading respectively indicate the regimes to which the western ridge and the eastern ridge of the LS belong, as will be discussed in Chapter 4.3.

ated waves is essentially unchanged, there is generation of higher spatial harmonics that form clear tidal beams. Balmforth et al. (2002) extended the theoretical predictions to finite slope, and found a gradual increase in tidal energy conversion rate as ε approaches 1, where the conversion of a sinusoidal topography is 56% larger than Bell's weak topography estimate. For infinitely steep topography, Llewellyn Smith & Young (2002), St. Laurent et al. (2003) examined internal tide generation at a knife-edge ridge and found that for small h_0/H, a knife-edge topography can generate energy flux twice as large as Bell's prediction, and that energy flux increases as h_0/H increases. Using a Green's function approach, Pétrélis et al. (2006), Balmforth & Peacock (2009) investigated the energy conversion for isolated topography of arbitrary steepness and finite height. It was found that the calculations agree with the previous conclusions for a knife-edge topography and Bell's predictions with weak topograhy assumption. The transition between the two limits is gradual and monotonic for most h_0/H, and a knife-edge topography turns out to be a reasonable approximation for any isolated steep and tall ridges.

Another parameter, being not independent of the parameters listed above, is the topographic Froude number, which measures the obstruction of the flow by topography and turns out to be useful for analyzing the flow patterns (Baines 1995, Legg & Huijts 2006). It is defined as

$$Fr = \frac{u_0}{Nh_0} \tag{2.22}$$

which can be expressed as

$$Fr = \frac{ku_0}{\omega} \times \frac{\omega}{N} \times \frac{1}{kh_0} \sim \frac{ku_0}{\omega} \times \frac{\alpha}{\nabla h_0} = \frac{ku_0/\omega}{\varepsilon} \tag{2.23}$$

i.e., the ratio of the tidal excursion to the steepness parameter when $f << \omega << N$. For large Fr, the flow remains relatively unaffected by topography, whereas for small Fr, the flow is impeded by topography. Regime 4 of Figure 2.1 corresponds to the case for $\varepsilon > 1$ and $Fr < 1$. Numerical simulations of Legg & Huijts (2006), Legg & Klymak (2008) showed that this is a regime where highly nonlinear, breaking lee waves take place, and a large flow is conducive of such features. A couple of locations in the world's oceans were identified by Legg & Klymak (2008) to meet such conditions, and the induced energetic local mixing can significantly contribute to the global energy budget distribution. However, for $ku_0/\omega > 1$, $Fr > 1$ (Regime 3 of Figure 2.1), which corresponds to a low, narrow topography, no overturning was observed (Legg & Huijts 2006).

Bell's theory and many later works postulated that the ocean is infinitely deep, which implies that the radiated energy flux travels upwards without being reflected back by a surface. Bell (1975*b*) argued that the upward going waves would be dissipated by processes like shear instability and wave-wave interactions before being reflected. However, this point of view was questioned later, for example, St. Laurent & Garrett (2002) showed that the Richardson number of the internal tides is not small enough to lead to shear instability, and that the time scale of wave-wave interaction is relatively long compared to the propagation time of the internal tide. Particularly, the long-range propagation of low-mode internal tides with multiple reflections at the surface and bottom has been robustly shown by global and regional baroclinic models (Niwa & Hibiya 2004, Simmons et al. 2004). Given the flaws of infinite-depth assumption, Llewellyn Smith & Young (2002), Khatiwala (2003) theoretically extended Bell's formulation to finite depth by applying an upper boundary. The assumption imposes an upper limit for the possible horizontal wavelength, and it was shown that the presence of the upper boundary can significantly reduce the tidal conversion compared to that of an infinite ocean, especially for larger lengths of topography. St. Laurent et al. (2003) analytically studied the internal tide generation of a very steep ($\varepsilon \sim \infty$) knife-edge, a step, and a top-hat topography without assuming $h_0/H << 1$. The condition $h_0/H << 1$ was relaxed for any topography by Vlasenko et al. (2005), who formulated the analytical generation problem by using a transformed small 'effective' height of topography, which also takes the variation of stratification into account. Such a formulation makes it possible to consider large obstacle height that is comparable with the fluid depth, as long as the top of topography is under the pycnocline, which is usually the case in the oceans.

2.2.2 Numerical modelling

While the aforementioned analytical models are physically based and are instructive and illuminating in interpreting internal tide generation problem, they are often constrained from realistic situation, especially for the circumstance when nonlinearity is notable. Given that, numerical simulations can be employed to validate analytical models and to explore regimes where analytical solutions are invalid. Within recent years, the increasing development of massive ocean models and computational facility make the 3D regional or even global realistic simulation of internal tide generation and evolution possible. A number of hot spots in the world's oceans have been identified with conspicuous wave activities and energetics. Several prominent places include the northern South China Sea (Jan et al. 2008, Zhang et al. 2011), the East China Sea (Niwa & Hibiya 2004), the Hawaiian Ridge (Merrifield & Holloway 2002), the Monterey Bay (Kang & Fringer 2012), etc.

2.3 Internal solitary wave theory and models

2.3.1 Weakly nonlinear theory: KdV equation and its solution

The KdV theory is the most well-known model for the description of unidirectional weakly nonlinear waves in weakly dispersive water (Benny 1966, Lee & Beardsley 1974). For a progressive wave propagating in the x-direction, the Boussinesq equations yield the KdV equation: the wave profile $A(x,t)$ is governed by

$$A_t + cA_x + \alpha AA_x + \beta A_{xxx} = 0 \tag{2.24}$$

where subscripts x and t are respectively spatial and temporal derivatives. α, β, and c are the coefficients of nonlinearity, dispersion, and linear long wave phase speed, among which the sign of α determines the polarity of an ISW, with positive and negative values corresponding to waves of depression and elevation (first mode), respectively. In the Boussinesq approximation, α and β are expressed as

$$\alpha = \frac{3c}{2}\frac{\int_{-H}^{0}(d\Phi/dz)^3 dz}{\int_{-H}^{0}(d\Phi/dz)^2 dz} \tag{2.25}$$

$$\beta = \frac{c}{2}\frac{\int_{-H}^{0}\Phi^2 dz}{\int_{-H}^{0}(d\Phi/dz)^2 dz} \tag{2.26}$$

in which Φ and c can be solved by the linear eigenvalue problem

$$\Phi_{zz} + \frac{N(z)^2}{c^2}\Phi = 0, \tag{2.27}$$

$$\Phi(-H) = \Phi(0) = 0 \tag{2.28}$$

through numerical approach if the buoyancy frequency $N(z)$ is known.

In a two-layer case with the upper and lower layer depth equal to h_1 and h_2, respectively, c, α and β can be simplified as

$$c = \sqrt{\frac{g'h_1h_2}{h_1+h_2}} \tag{2.29}$$

$$\alpha = \frac{3}{2}c\frac{h_1-h_2}{h_1h_2} \tag{2.30}$$

$$\beta = \frac{ch_1h_2}{6} \tag{2.31}$$

where $g' = g(\rho_2-\rho_1)/\rho_2$ is the reduced gravity; ρ_1 and ρ_2 are the densities in the upper and lower layers, respectively.

KdV equation (2.24) is completely integrable, and the solitary wave solution, among others, is

$$A = a_\xi sech^2(\frac{x-Vt}{\lambda}) \tag{2.32}$$

where a_ξ is the wave amplitude; V and λ are respectively the nonlinear phase speed and width of the ISW:

$$V = c + \frac{\alpha a_\xi}{3} \tag{2.33}$$

$$\lambda = \sqrt{\frac{12\beta}{\alpha a_\xi}} \tag{2.34}$$

2.3.2 Weakly nonlinear theory: extentions of KdV equation

Despite the assumption of weak nonlinearity, the KdV solution has turned out to be capable of simulating wave evolution outside its valid range (Holloway et al. 1997). However, there are certain limitations of the KdV equation, one of which is that, as is seen from equation (2.30), the nonlinear coefficient α just vanishes when $h_1 = h_2$. In such a case near this point (the so-called turning point), the next cubic nonlinearity could be comparable in magnitude with the quadratic one, and a higher-order modification of the KdV equation leads to the extended KdV equation (Gardner equation):

$$A_t + (c + \alpha A + \alpha_2 A^2)A_x + \beta A_{xxx} = 0 \tag{2.35}$$

where α_2 is the coefficient of cubic nonlinearity and it has a much more complex form than α (Holloway et al. 1999).

The eKdV equation is also integrable and has a number of solutions. Opposing to the KdV solution, the amplitude of the eKdV wave cannot take arbitrarily large values. There is an upper boundary of the amplitude which is determined by h_1 and h_2. When approaching this boundary, the wave becomes increasingly broad, forming a wide plateau on top that terminates at each end by dissipationless bores (Helfrich & Melville 2006).

Despite the inclusion of a higher order nonlinear term, the eKdV equation is still formulated on the ground of weakly nonlinear assumption. Yet, it does show advantages in delineating the profiles of ISWs (Stanton & Ostrovsky 1998). Also, it turns out that the application of the eKdV equation is considerably beyond its original valid range. Comparison of the wave characteristics with fully nonlinear theories gives a fairly close agreement, given that h_1 and h_2 are not too different (Helfrich & Melville 2006).

Another limitation of the KdV equation is the assumption of weak dispersion, i.e., the waves are long compared to the water depth. Nonetheless, when considering a two-layer medium with a very deep lower layer, the long wave assumption is violated, and the nonlinear evolution equation appropriate in describing this system is the Benjamin-Ono (BO) equation (Benjamin 1967, Ono 1975) which has an algebraic soliton solution. However, largely being of theoretical interest, the advantage of the BO equation over KdV equation is unjustified, even in deep water. Moreover, there also exists a more general nonlinear equation that compromises with the two

extreme cases of shallow water and deep water: the intermediate depth wave equation, as was brought up by Joseph (1977), Kubota et al. (1978).

When studying mesoscale oceanic processes with spatial scales near the (internal) Rossby radius, rotational effects should be taken into account. Assuming small rotation, Ostrovsky (1978) first derived the rotation-modified KdV equation (rKdV, also referred as the Ostrovsky equation):

$$(A_t + cA_x + \alpha AA_x + \beta A_{xxx})_x = \gamma A \tag{2.36}$$

The background rotation is indicated by γ, which is given by

$$\gamma = \frac{f^2}{2c} \tag{2.37}$$

where f is the Coriolis parameter.

The above Ostrovsky equation has the linear dispersion relation, in the reference frame moving with the linear long wave speed c:

$$c_p = \frac{\omega}{k} = \frac{\gamma}{k^2} - \beta k^2 \tag{2.38}$$

where k, ω, and c_p are the wavenumber, frequency, and phase velocity for a sinusoidal wave, respectively. The corresponding group velocity is

$$c_g = \frac{\partial \omega}{\partial k} = \frac{\gamma}{k^2} - 3\beta k^2 \tag{2.39}$$

In seeking a localized solution of the Ostrovsky equation 2.36, some important integral constraints should be exerted, of which a most common one is the 'zero-mass' condition

$$M = \int_{-\infty}^{\infty} dx = 0 \tag{2.40}$$

Such integrals are valid for localized perturbations which shall vanish as $|x| \to \infty$.

An important feature of the Ostrovsky equation is the non-existence of a stationary localized solution (Leonov 1981). Under rotation, a KdV wave undergoes continuous decaying process by radiating inertia-gravity waves (*Poincaré* waves) backwards (Grimshaw et al. 1998). The leading wave annihilates in a certain time, as is expressed as

$$\frac{A}{A_0} = (1 - \frac{t}{t_d})^2 \tag{2.41}$$

where A_0 is the amplitude of the initial ISW; t is time and t_d is the scale of the terminal damping time. However, analysis of stationary solutions of the Ostrovsky equation can be conducted if the nonhydrostatic term is neglected (β=0 in equation (2.36)), which is valid for sufficiently

long waves. This new equation, called reduced Ostrovsky equation or Ostrovsky-Hunter equation, was first analyzed by Ostrovsky (1978), and its stationary solutions were later presented in more detail by Stepanyants (2006).

In addition to the stationary solutions, non-steady solutions of the Ostrovsky equation have also been explored. Gilman et al. (1996) found that, despite of the so-called 'anti-soliton theorem', non-stationary ISWs can co-exist with long, smooth background waves of small amplitude, whereas in the other regime of their calculation it was shown that an initial KdV wave decays by shedding long tails, which is as predicted by asymptotic theory (Grimshaw et al. 1998). The radiated long wave can steepen and form a new ISW with nearly identical parameters to the original wave, and this process repeats quasi-periodically.

The above-mentioned equations are all one-dimensional equations (x-direction). Assuming a slow variation of solutions in y-direction, the KdV equation is generalized to the two-dimensional Kadomtsev-Petviashvili equation - or KP equation (Kadomtsev & Petviashvili 1970), which is also completely integrable. The KP equation was further extended to the rotation-modified KP equation (Grimshaw 1985), with the form in a rotating channel

$$(A_t + \alpha A A_x + \beta A_{xxx})_x + \frac{1}{2} c (A_{yy} - \nu^2 A) = 0 \tag{2.42}$$

$$A_y + \nu A = 0, \quad y = 0, l \tag{2.43}$$

where $\nu = R_0^{-1} = f/c$ is the inverse internal Rossby radius which measures the strength of rotation. When omitting the transverse variations ($A_{yy} = 0$), equation (2.42) is reduced to the Ostrovsky equation (2.36).

Numerical calculations of the rotation-modified KP equation in a rotating channel were presented in a number of theoretical papers (Grimshaw 1985, Katsis & Akylas 1987, Grimshaw & Tang 1990, Akylas 1991, Sánchez-Garrido & Vlasenko 2009). It was generally concluded that an initially ISW with straight crest evolves into a wave with backwards curved wavefront that has exponentially decreasing amplitude, which is the characteristic of a Kelvin wave. The initial ISW attenuates quickly due to the radiation of secondary waves, with a feature much resembles the solution of the Ostrovsky equation.

2.3.3 Fully nonlinear theory

The previous KdV-type equations all treat nonlinearity as very small, in the sense that wave displacement is small compared to a depth scale, which can be the whole water depth, or one layer depth in a two-layer system. However, with a growing number of observed ISWs for which they are evidently large, the validity of KdV theory is questioned. Despite the aforementioned capability of KdV-type equations, especially eKdV equation, in delineating ISWs that are not within their valid range, fully nonlinear theories are ultimately needed to describe more accurately properties of the observed very large waves.

Fully nonlinear internal waves can be described by manipulating the basic hydrodynamic equations. Within the Boussinesq approximation, for 2D waves in a steady state and in a continuously stratified flow, the basic Euler equations can be reduced to only one single equation for the streamfunction Ψ. This is the so-called Dubreil-Jacotin-Long (DJL) equation, or Long equation (Long 1953):

$$\frac{\partial^2 \Psi}{\partial^2 \xi} + \frac{\partial^2 \Psi}{\partial^2 z} + \frac{N^2(z-\Psi/V)}{V^2}\Psi = 0 \tag{2.44}$$

where $\xi = x - Vt$, V is the phase speed; $N = N(z)$ is the known buoyancy frequency.

Using the DJL equation, Lamb (2002) numerically investigated the formation of trapped cores via ISW shoaling and studied the upper limits of wave amplitude in several scenarios. The extension of the DJL equation to include a mean background shear current was presented by Stastna & Lamb (2002), Lamb (2003).

To describe strongly nonlinear solitary waves, steady wave solutions have been achieved by directly solving the Euler equations, mostly in a two-layer fluid (Turner & Vanden-Broeck 1988, Evans & Ford 1996, Grue et al. 1999). It was found that there is a limiting amplitude at which an ISW has a flat top, in a manner similar to the case of the eKdV equation. In a Boussinesq fluid, at this limit the wave amplitude $\eta_{0\ lim}$ and velocity V_{lim} are

$$\eta_{0\ lim} = \frac{h_1 - h_2}{2} \tag{2.45}$$

$$V_{lim} = \frac{\sqrt{g'(h_1+h_2)}}{2} \tag{2.46}$$

where $g' = g(1-\rho_1/\rho_2)$.

Miyata (1985, 1988), Choi & Camassa (1999) derived the long-wave equation for fully nonlinear, weakly nonhydrostatic waves in a two-layer flow (MCC equation). This equation is of a similar nature to the DJL equation but is not necessarily stationary. It predicts wider and slower waves compared with the KdV equation. The MCC equation solution is shown to be in agreement with laboratory experiments and full numerical solutions of the Euler equations over a wide range of layer depths, as was illustrated by Ostrovsky & Grue (2003), who also derived a long-wave, strongly nonlinear model in the Boussinesq approximation which is equivalent to the MCC equation. Helfrich (2007) modified the MCC equation to accommodate rotation and studied the decay-return process of an ISW.

Moreover, there are a number of famous massive oceanic models that are more than capable of simulating the properties and dynamics of ISWs with fully nonlinear, fully nonhydrostatic schemes. Such modes include (nonhydrostatic) FVCOM, ROMS, SUNTANS, MITgcm, etc. However, such direct numerical computations are often computationally expensive and are hard to bring enough physical insight into the concerned problem.

2.3.4 Generation mechanisms of ISWs

There are a variety of ways that ISWs can be generated. The diversity of generation mechanisms can produce ISWs of different characters. Some review works have been carried out (Vlasenko et al. 2005, Helfrich & Melville 2006, Jackson et al. 2012), and it is briefly summarized in this section.

The most common mechanism is due to the interaction of barotropic tides with underwater bottom features, which can generate internal tides. This is most likely when the tidal excursion parameter ku_0/ω is small. During the outward propagation of the (low-mode) internal tides, if

sufficiently energetic, their fronts can gradually evolve into ISWs under the effects of nonlinear steepening and dispersion (Lee & Beardsley 1974, Gerkema & Zimmerman 1995, Helfrich & Grimshaw 2008).

A second mechanism is the 'lee wave mechanism' (Maxworthy 1979, Nakamura et al. 2000), that is, lee waves are formed in the ebb phase of the barotropic tides, and during this period they absorb energy from the background currents and grow in amplitudes. When barotropic tides slacken and gradually turn into flood tides, they are released and propagate upstream. This mechanism is likely to occur with larger tidal excursion, i.e., $ku_0/\omega >> 1$. For internal waves of higher modes that are generated locally, they have less chance to break through the background tidal currents due to the smaller phase speeds. They are therefore trapped near the generation site, where they die away and contribute to the local dissipation and mixing (Klymak et al. 2010).

A third mechanism was proposed by Gerkema (2001) who showed that the generated tidal beams can interact strongly with a moderate thermocline, which further leads to the 'local generation' of internal wave packets accompanied by downward energy leakage from the thermocline. It was found by Gerkema (2001) that a moderately stratified thermocline is necessary for such a mechanism to occur, whereas neither a strong or a weak thermocline is favorable for the generation.

A fourth mechanism was put forth by Maxworthy (1979), who observed that when the background currents are strong enough to induce mixing above bottom features, the collapse of mixed water can produce internal waves propagating out of the source region, which further develop into solitary waves through nonlinear steepening.

Some other mechanisms, albeit not very common, can also lead to the generation of ISWs, for example, through resonant generation, and river plume generation.

Chapter 3

Methodology

3.1 Massachusetts Institute of Technology general circulation model

The Massachusetts Institute of Technology general circulation model (MITgcm) is a numerical model designed for the study of both atmospheric and oceanic phenomena with various scales (Marshall, Adcroft, Hill, Perelman & Heisey 1997). Its numerical implementation is based on 3D incompressible Navier Stokes equations with fully nonhydrostatic terms. The governing equations, within a traditional vertical z-coordinate, are:

$$\frac{\partial u}{\partial t} + \frac{\partial p}{\partial x} = G_u \tag{3.1}$$

$$\frac{\partial v}{\partial t} + \frac{\partial p}{\partial y} = G_v \tag{3.2}$$

$$\frac{\partial w}{\partial t} + \frac{\partial p}{\partial z} = G_w \tag{3.3}$$

$$\frac{\partial u}{\partial x} + \frac{\partial v}{\partial y} + \frac{\partial w}{\partial z} = 0 \tag{3.4}$$

$$\frac{\partial T}{\partial t} = G_T \tag{3.5}$$

$$\frac{\partial S}{\partial t} = G_S \tag{3.6}$$

$$\rho = \rho(T,S,p) \tag{3.7}$$

where the zonal velocity u, meridional velocity v, and vertical velocity w, potential temperature T, salinity S, pressure p, and density ρ characterize the basic state and movement of the ocean. Equations (3.1), (3.2), and (3.3) are the momentum equations; (3.4) is the non-divergence continuity equation; (3.5) and (3.6) are the thermodynamic equations; (3.7) is the Equation of State. G_u, G_v, and G_w are tendency terms in the respectively zonal, meridional, and vertical directions that comprise of advection, metric forces, Coriolis, and forcing/dissipation, as are defined below from left to right in each equation (in spherical coordinates):

$$G_u = -\mathbf{v}\cdot\nabla u - \{\frac{uw}{r} - \frac{uv\tan\phi}{r}\} - \{-2\Omega v\sin\phi + 2\Omega w\cos\phi\} + F_u \tag{3.8}$$

$$G_v = -\mathbf{v}\cdot\nabla v - \{\frac{vw}{r} - \frac{u^2\tan\phi}{r}\} - 2\Omega u\sin\phi + F_v \tag{3.9}$$

$$G_w = -\mathbf{v}\cdot\nabla w + \frac{u^2+v^2}{r} + 2\Omega u\cos\phi + F_w - g\frac{\delta\rho}{\rho_{ref}} \tag{3.10}$$

where the last term in (3.10) is the buoyancy term in which $\delta\rho$ and ρ_{ref} denote a density derivation from the hydrostatically balanced state at rest and a constant value of density, respectively. g is the acceleration of gravity. $\mathbf{v} = (u, v, w)$ is the velocity vector, and ϕ is the latitude. ∇ is the gradient operator within the spherical coordinates. In the thermodynamic equations,

$$G_T = -\nabla\cdot(\mathbf{v}T) + F_T \tag{3.11}$$

$$G_S = -\nabla\cdot(\mathbf{v}S) + F_S \tag{3.12}$$

The above equations (3.1-3.12) are hence discretized and solved with the appropriate boundary conditions, and the strategies and algorithms will be briefed later.

Overall, depending on the scales and features of the fluid motions that studied and the concomitant simplification of the dynamical equations, there are three modes of equation sets formulated, viz., the hydrostatic, quasi-hydrostatic, and nonhydrostatic sets (Marshall, Hill, Perelman & Adcroft 1997). The first set is known as the 'hydrostatic primitive equations' in which the vertical momentum equation (3.3) is reduced to the state of hydrostatic balance (see equation (3.13)), and in which the 'traditional approximation' and the 'shallow atmosphere approximation' are made.

$$\frac{\partial p_{HY}}{\partial z} + \tilde{g} = 0 \tag{3.13}$$

where $\tilde{g} = g\frac{\delta\rho}{\rho_{ref}}$ is the reduced gravity. p_{HY} comes from the pressure p when the latter is decomposed into three components, viz., the surface pressure (p_S), the hydrostatic pressure (p_{HY}), and the nonhydrostatic pressure (p_{NH}),

$$p = p_S + p_{HY} + p_{NH} \tag{3.14}$$

In quasi-hydrostatic mode of the equations, the strict hydrostatic balance is relaxed, and in (3.10) the advection and forcing/dissipation terms are omitted, whereas all the other terms in the momentum equations are retained. The shallow atmosphere approximation is relaxed as well and all the metric terms are kept. The quasi-hydrostatic equations also treat the Coriolis terms fully. Despite the added terms, solutions of the quasi-hydrostatic mode is as computationally cheap as the hydrostatic mode, which is in sharp contrast with the nonhydrostatic mode that involves massive computational power. The nonhydrostatic equations reserve all the terms in the dynamic equation set, and thus is expected to be capable of studying the flows across the whole range of scales, from small scale convections (~100 m) to large scale global circulations (~10 000 km). However, its computational demanding has hampered the broad use for large scale motions, and in such a case hydrostatic, or quasi-hydrostatic equations can be a fine approximation.

The above three modes, of which the quasi-hydrostatic mode is relatively less used, shall be chosen appropriately based on the characteristics of the phenomena. A parameter that divides the hydrostatic and nonhydrostatic regimes is defined as (Marshall, Hill, Perelman & Adcroft 1997):

$$n = \frac{\gamma^2}{R_i} \tag{3.15}$$

where $\gamma = \frac{h}{L}$ is an aspect ratio of the motion, and $R_i = \frac{N^2h^2}{U^2}$ is the Richardson number. Here h and L are the vertical and horizontal scales of the system, respectively. U is the horizontal velocity scale, and N is the buoyancy frequency. When $n << 1$, the flow can be readily treated as hydrostatic, and the primitive equations are therefore sufficient to delineate the motions that are concerned. Nevertheless, it has been shown in MITgcm (Marshall, Adcroft, Hill, Perelman & Heisey 1997) that for $n << 1$, even when the nonhydrostatic equation set is employed, there is only slightly more computational efforts involved than those using hydrostatic equations.

The time-discrete form of the nonhydrostatic equations (3.1-3.6) with time step Δt is as follows:

$$\frac{u^{n+1} - u^n}{\Delta t} = G_u^{n+1/2} - \frac{\partial}{\partial x}\{p_S + p_{HY} + p_{NH}\}^{n+1/2} \tag{3.16}$$

$$\frac{v^{n+1} - v^n}{\Delta t} = G_v^{n+1/2} - \frac{\partial}{\partial y}\{p_S + p_{HY} + p_{NH}\}^{n+1/2} \tag{3.17}$$

$$\frac{w^{n+1} - w^n}{\Delta t} = \tilde{G}_w^{n+1/2} - \frac{\partial}{\partial z} p_{NH}^{n+1/2} \tag{3.18}$$

$$\frac{\partial u^{n+1}}{\partial x} + \frac{\partial v^{n+1}}{\partial y} + \frac{\partial w^{n+1}}{\partial z} = 0 \tag{3.19}$$

$$\frac{T^{n+1} - T^n}{\Delta t} = G_T^{n+1/2} \tag{3.20}$$

$$\frac{S^{n+1} - S^n}{\Delta t} = G_S^{n+1/2} \tag{3.21}$$

where n denotes the nth time step. $\tilde{G}_w = G_w + \tilde{g}$. The $G^{n+1/2}$ terms are treated explicitly using the quasi-second order Adams-Bashforth method that uses two time levels at n and $n-1$,

$$G^{n+1/2} = (3/2 + \varepsilon_{AB})G^n - (1/2 + \varepsilon_{AB})G^{n-1} \tag{3.22}$$

where ε_{AB} is a small value, and it would be second order accurate if ε_{AB} is taken zero, but this proves to be weakly unstable for certain circumstances.

The key algorithm of the model lies in a 'pressure correction' method which involves solving a Poisson equation for the pressure with the Neumann boundary conditions implemented. Detailed solving procedure is presented by Marshall, Adcroft, Hill, Perelman & Heisey (1997), Marshall, Hill, Perelman & Adcroft (1997), and will only be briefly summarized here. As is outlined in Figure 3.1, for hydrostatic, quasi-hydrostatic, and nonhydrostatic cases, a 2D elliptic equation is inverted to obtain the surface pressure p_S, and the hydrostatic pressure p_{HY} on one certain level is derived by integrating the weight of the fluid above that level, which requires the solution from the thermodynamic equations. Then under the hydrostatic and quasi-hydrostatic modes, the horizontal velocities u and v are stepped forward, and the vertical velocity w can be found diagnostically from the continuity equation. However, for nonhydrostatic dynamics, before forwarding the velocities, a further 3D elliptic equation must be inverted in order to obtain the solution of the nonhydrostatic pressure p_{NH}. This is the most computationally demanding part of the core algorithm, as was introduced earlier, but its overhead is minute when modelling flows that are within the hydrostatic limit. After p_{NH} is found, w is then stepped forward prognostically within the vertical momentum equation (3.18).

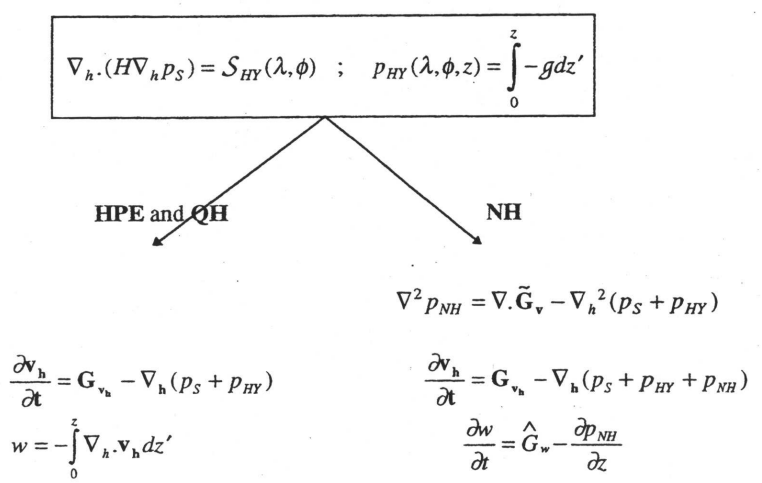

Figure 3.1: Schema of the solution strategy of MITgcm (adopted from Marshall, Hill, Perelman & Adcroft (1997)). HPE, QH, and NH denote hydrostatic, quasi-hydrostatic, and nonhydrostatic equations, respectively.

The 2D and 3D elliptic problems are inverted using a preconditioned conjugate-gradient iteration method, with physically-implicated preconditioners used for computational efficiency, which especially reduces the amount of calculation for the 3D inversion under the hydrostatic limit.

On the other hand, spatial discretization of MITgcm is carried out using the finite volume approach. This method treats the ocean as a number of 'volumes', and the variable fluxes are defined normal to the faces covering them. An 'intersecting boundary method', which allows for piece-wise shaved cells, is used to achieve a more accurate representation of the bottom topography.

A wide range of advection schemes for tracers (temperature, salinity, and others), linear and nonlinear, are available in MITgcm. This mostly serves to handle the instabilities developed at the discontinuous jumps whilst without adding too much numerical diffusion. The default scheme in MITgcm is the centered second order advection, which is apt to be noisy and needs some remedy of diffusion schemes. The model does offer a variety of eddy viscosity and diffusivity parameterizations. For example, in the later chapters, the following two parameterization schemes are implemented in the model setups. A very common scheme is a Richardson number-dependent parameterization (Pacanowski & Philander 1981) that is on a more realistic physical ground. It is used to calculate the vertical eddy viscosity γ and diffusivity κ:

$$\gamma = \frac{\gamma_0}{(1+\alpha Ri)^n} + \gamma_b, \quad \kappa = \frac{\gamma}{1+\alpha Ri} + \kappa_b \tag{3.23}$$

where $Ri = N^2(z)/(u_z^2 + v_z^2)$ is the Richardson number (N is the buoyancy frequency; u_z and v_z are respectively vertical shear of zonal velocity and meridional velocity). $\gamma_b = 10^{-5}\ m^2 s^{-1}$ and $\kappa_b = 10^{-5}\ m^2 s^{-1}$ are the background viscosity and diffusivity parameters, respectively. $\gamma_0 = 1.5 \times 10^{-2}\ m^2 s^{-1}$, $\alpha = 5$, and $n = 1$ are adjustable parameters. Such a scheme increases γ and κ in areas where Ri is small. The horizontal viscosity (A_h) can be calculated using the

scheme due to Leith (Leith 1996) in which viscosity is proportional to the magnitude of the horizontal gradient of the relative vorticity ($|\nabla\overline{\omega}_3|$) times the cubed grid spacing (L), where the overbar denotes a filter over the subgrid scale L:

$$A_{hLeith} = (\frac{viscC2Leith}{\pi})^3 L^3 |\nabla\overline{\omega}_3| \tag{3.24}$$

where $viscC2Leith$ is a tunable coefficient.

Sensitivity experiments on the implementation of these two schemes were performed, and the results showed that the essential features remained unchanged, but numerical noise could arise without any of the two schemes.

3.2 Synthetic aperture radar imagery

A satellite or aircraft mounted SAR can transmit signals with a variety of frequencies (0.4 to 10 GHz, wavelength 3 to 75 cm, designated by X, C, S, L, and P bands from high to low frequency) and receive returning signals scattered by the sea surface roughness that is about the order of the radar wavelength (typically several centimeters to a few meters). The roughness is primarily generated by the wind stress and is characterized from capillary to short gravity waves. Long gravity waves and currents can also affect the imagery in a somehow indirect way by modulating wind-generated waves. SAR signals are independent of solar illumination and are able to pass through the cloud freely without being affected. SAR also takes the advantage of controlling factors like frequency, polarization, incident angle, resolution, and swath, etc., and different imageries can be derived under the effects of different factors (McCandless & Jackson 2005).

After the launch of the first civilian SAR satellite, i.e., SEASAT, SAR imagery has revealed a wealth of atmospheric and oceanic motions with different temporal and spatial scales. Such phenomena include surface and internal waves, air-sea interactions, currents, slicks, bathymetry, etc. Some features may even appear simultaneously in one image and overlap with each other (Holt 2005). A summary of the groups of features by spatial scales, measurements from the features, imaging mechanisms, application range of wind speed, and some key characteristics was made by Holt (2005). Examining SAR images is complex, and the detailed view of the sea surface signature is not understood very well, since the sensitivity of imagery is greatly affected by numerous external factors, especially wind stress. Also note that application of sea surface imaging is hampered by temporal discontinuity, due to the fact that satellite sensors have periodic imaging normally separated by several days when passing by the same location. Regardless of the shortcomings, the archives of some ten years of SAR images from various missions (SEASAT, SIR-A/B, ERS-1/2, RADARSAT-1/2, ENVISAT, etc.) have provided great insight into the understanding of a variety of oceanic and atmospheric phenomena by the support of near real-time observation and monitoring.

Among the sea surface features that SAR imagery is able to capture, ISWs is probably one of the most easily recognizable oceanic phenomena. In fact, they were an unexpected result from SEASAT, and were further confirmed by the subsequent missions with a large quantity of images (Holt 2005). This has made the global ubiquitous feature of ISWs appreciated. Most ISWs exhibit the characteristics in SAR images that they propagate in separate packets that either contain a single wave or a wave train, with each packet being generated by diurnal or semidiurnal tidal currents. The leading wave in a packet usually possesses the largest amplitude, wavelength, and along-crest width. The arcs of the waves are often observed to be curved

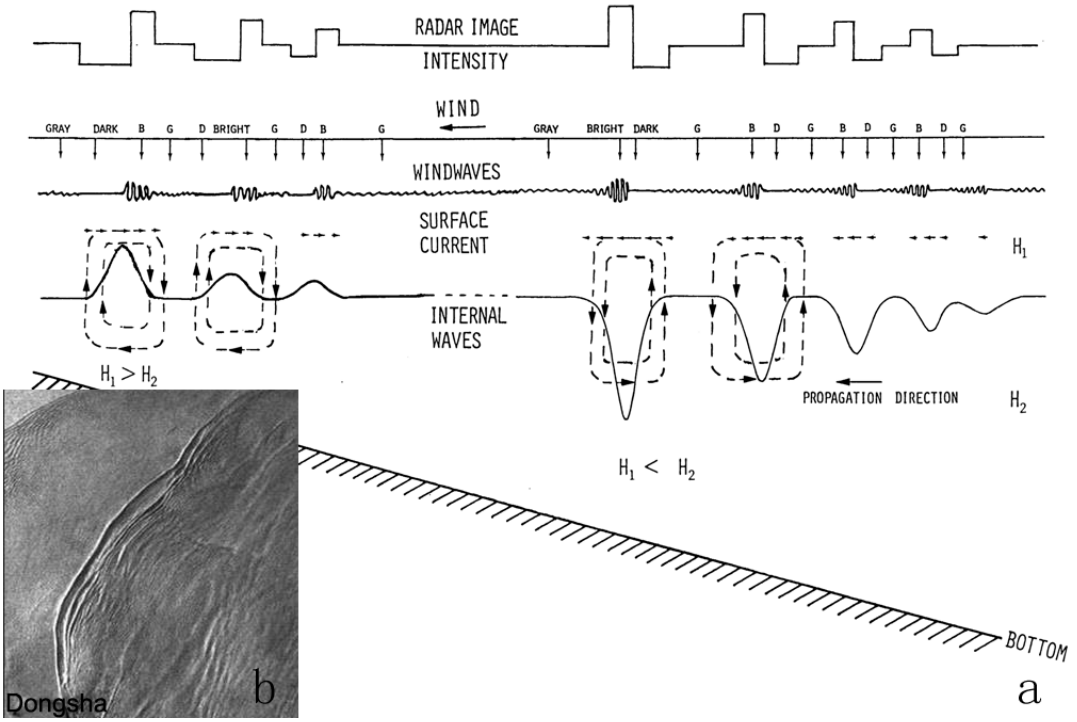

Figure 3.2: a) Schematic diagram of the motion of ISWs, the resultant surface response, and SAR image intensity variation (from Liu et al. (1998)); b) an example of an ASAR image featuring an ISW packet near the Dongsha Atoll.

backwards, and bright/dark stripes normally alternate in a packet.

Figure 3.2a is a schematic diagram of the motions of ISW packets on a slope and how their surface manifestations are detected by the SAR sensors. Figure 3.2b is an example of an ISW packet signature in an ASAR image. In a two-layer system, first mode ISWs are depressions when the lower layer is greater than the upper layer (the right wave packet in Figure 3.2a). The velocity structure of an ISW leads to a surface zone of convergence and divergence in the front and rear of the middle of the wave, respectively. Such zones modulate the surface roughness spectrum through the interaction of the current field with wind-generated waves and manifest themselves as bright/dark stripes in SAR images. To be more specific, the convergence zone makes the sea surface rougher, which indicates more radar signals being backscattered to the sensor, and a bright stripe is obtained. On the contrary, the divergence zone is associated with the dark stripe due to the relatively smoother sea surface caused by the dampening of short waves. On the other hand, for waves of elevation (the left wave packet in Figure 3.2a) the dark stripe is aligned in front of the bright stripe, due to the reverse of polarity and velocity field. Radar imaging theory of internal waves brought up by Alpers (1985) indicates that the brightness of signal that appears in SAR images is directly associated with the sea surface horizontal velocity gradient induced by ISWs. Typical values of this gradient for ISWs in the oceans are in the order of $10^{-4} - 10^{-3}\ s^{-1}$ (Alpers 1985).

Chapter 4

3D simulation of multimodal internal wave generation in the northern South China Sea

[1]

This section forms the fundamental and core part of this thesis. It concerns the simulation of ISW generation and properties in the northern SCS using MITgcm. The problems of multimodal wave structures and double-ridged effects are specially addressed. Sensitivity of wave field on some controlling parameters is discussed.

4.1 Model initialization

Due to the huge demand of computational resource, the model domain is only confined within the area between 20° and 21° N, and 117.5° and 122.5° N (see the area in Figure 1.3), which, zonally covers the double-ridged LS and the deep basin in the northern SCS, and meridionally covers the middle LS. Although the domain might be inadequate for the complete delineation of wave generation in the LS, which occurs across the whole strait (Jan et al. 2008), it was found from SAR compilations (Zhao et al. 2004, Zheng et al. 2007) that the main routes of the ISW propagation lie between 20° and 21° N, which justifies the selection of the model domain.

Bottom topography was derived from the 1' resolution ETOPO1 dataset. Given that the wave generation process is concerned in this section, water depth shallower than 3000 m in the far-field was all set to 3000 m, giving a deep basin with a constant depth. The Cartesian coordinate system $Oxyz$ was used, with the Oxy plane lying on the sea surface at rest, and with the Oz axis pointing vertically upward. Horizontal resolution in the eastward Ox direction was 250 m, whilst in the northward Oy direction the resolution was 1000 m. Four sponge layers with telescoping grids were implemented in the four open boundaries, where the resolution decreased exponentially to a very large value to ensure no waves, both barotropic and baroclinic, can be reflected back and pollute the interior solution. In the vertical direction, 90 layers were used, with the resolution equal to 10 m in the upper 500 m, followed by the resolution of 100 m in the intermediate 1000 m, and finally with the resolution of 150 m in the bottom 1500 m. Background stratification was designated horizontally homogeneous, and the data was obtained from the World Ocean Atlas (2005) for the summer stratification (see Figure 1.6). Time step was set to 12.5 s.

As has been shown in Figure 1.5, both diurnal and semi-diurnal tidal harmonics are very prominent at LS. Thus it would be reasonable to consider them all in the model. Nonetheless, the model domain is located very close to the critical latitude of the diurnal harmonics, i.e., about 30° N, which implies that the rotation shall greatly inhibit the generation of baroclinic waves and thus ISWs (Vlasenko et al. 2005). Meanwhile, the model domain is remote from the semi-

[1] This section is mostly based on the papers Vlasenko et al. (2010), Guo et al. (2011)

diurnal critical latitude (about 75° N), consequently effective baroclinic wave generation is foreseen. Hence, in this section only the semi-diurnal M_2 harmonic is taken into account, whereas the slight but non-neglectable diurnal modulation on the wave field will be scrutinized in Chapter 6.

The model was forced from quiescence by a periodic barotropic forcing in the horizontal momentum equations that takes the idealistic form of

$$F_x = UH_0/H(x,y)\sigma\cos(\sigma t), \quad F_y = UH_0/H(x,y)f\sin(\sigma t) \tag{4.1}$$

where H_0 is the depth where the barotropic tide has velocity U; H(x,y) is the local water depth; f is the Coriolis parameter; σ is the tidal frequency (M_2 is this case). An appropriate value of $U = 0.13\ ms^{-1}$ was chosen so that the strength of barotropic tide in the LS approximately matches with that predicted by the TPXO 7.1 model (Egbert & Erofeeva 2002).

4.2 Three-dimensional multimodal structure of baroclinic tides in the far field

For a panoramic view of the model output, the field of sea surface velocity gradient, which is a measure of sea surface water roughness and thus determines how obvious ISWs can be imaged by the SAR, is first displayed in Figure 4.1. The field shown is after five M_2 tidal periods. At a first glance of the figure, strong three-dimensionality with meridional intermittences is apparent near the generation site (east of 120° E), whereas west of 120° E the field is more or less meridionally homogeneous, with only slightly curved wavefronts. This is sort of contradictory with the observations acquired by the SAR (see Figure 1.3). Nevertheless, this would be readily attributed to the constant water depth set at the far-field and maybe also to the idealization of the barotropic forcing and the negligence of the Kuroshio. Given that this section concerns the generation process, this meridional straightness will not hamper the analyses that are given below.

To inspect the interior structures of the wave field, four zonal cross-sections (see the four dashed lines labeled *a*, *b*, *c*, and *d* in Figure 4.1) are chosen to illustrate the vertical distribution of the temperature field, as is shown in Figure 4.2. Some fragments are highlighted with shaded areas and the labels correspond to those in Figure 4.1. Overall, the four cross-sections exhibit qualitatively similar features, but also with clear variations, especially near the ridges. Take cross-section *b* for example, The leading wave packet is characterized by two first mode ISWs (A1) trailed by a second mode ISW (A2), on which some short internal waves ride. A scrutiny of fragment A1 is shown in Figure 4.3. Vertical temperature and zonal velocity fields are shown in this figure. It is clear that these are the first mode ISWs of depression. The leading wave has an amplitude of approximately 100 m and the reversal of the velocity direction occurs at a depth of about 800 m.

The counter-phase displacement of the isotherms in fragment A2 is indicative of an ISW of second mode. This is examined by comparing its vertical profiles with the KdV solution. In Figure 4.4, vertical profiles of the isothermal displacement, horizontal velocity, and vertical velocity from model output are calculated and compared with the KdV counterparts by solving a standard eigen-value problem. The coincidence between the two solutions justifies that fragment A2 can be treated as a second mode ISW. It has a maximum displacement of about 80 m, and the displacement reverses from depression to elevation at a depth of about 450 m.

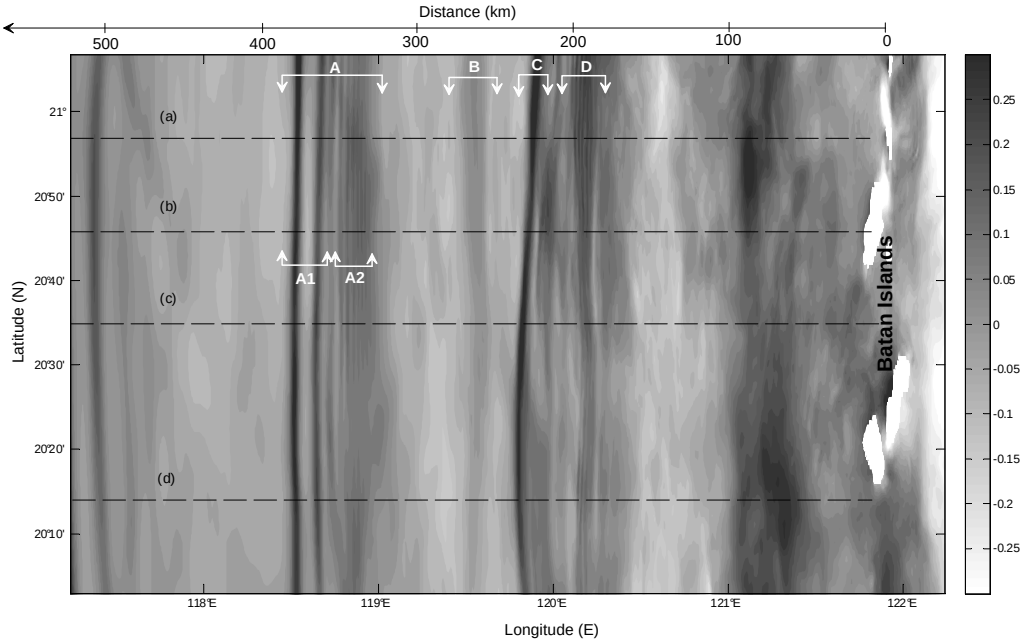

Figure 4.1: Model predicted sea surface height after 5 M_2 tidal periods. Internal waves are generated in the LS and propagate westward. The axis at the top indicates the distance from the eastern ridge in kilometers. Four fragments, A-D, are marked and denote some special structures that are analyzed in the text. Four cross-sections, (a)-(d), are chosen to illustrate the underwater structures and will be shown in Figure 4.2.

As for the short waves that ride on the second mode ISW, they merit further investigation, and this will be discussed in detail in Chapter 5. Returning to cross-section b in Figure 4.2, behind A1 and A2 there is another ISW of second mode (fragment B) and a single first mode (fragment C), which are apparently generated at later tidal cycles. The rightmost fragment (fragment D) comprises of some high modal non-stationary structures that will subsequently disintegrate. Qualitative picture of the waves in the far-field essentially remains unchanged in the other three cross-sections, whereas in the near-field it varies, due to the irregular and abrupt distribution of topography aligned meridionally.

4.3 Characteristics of baroclinic tides near the generation site

Various conclusions on the generation mechanism of internal wave generation from the LS have been reached, as was reviewed in section 1.2, which basically involves a debate of whether an 'internal tide release' or a 'lee wave' mechanism dominates. Two most pertinent parameters that control the internal wave generation were already previously discussed in section 2.2.1: the tidal excursion (ku_0/ω) and the slope parameter (ε). For $ku_0/\omega << 1$, linear baroclinic tides are excited; for $ku_0/\omega >> 1$, unsteady lee waves are generated. In the intermediate case, i.e., $ku_0/\omega \sim 1$, a mixed lee wave regime is obtained where both baroclinic tides and lee waves are present. The slope parameter α largely determines the conversion of barotropic tidal energy and the shape of the baroclinic fields (see section 2.2.1). It is known that tall and steep topography, which mostly implies a critical or supercritical slope, is favorable for the tidal conversion and the formation of obliquely radiated tidal beams, both upwards and downwards.

In the circumstance of the northern SCS, a rough estimation of ku_0/ω gives a magnitude of the order unity in the shallow water surrounding the islands, whereas the majority of the strait

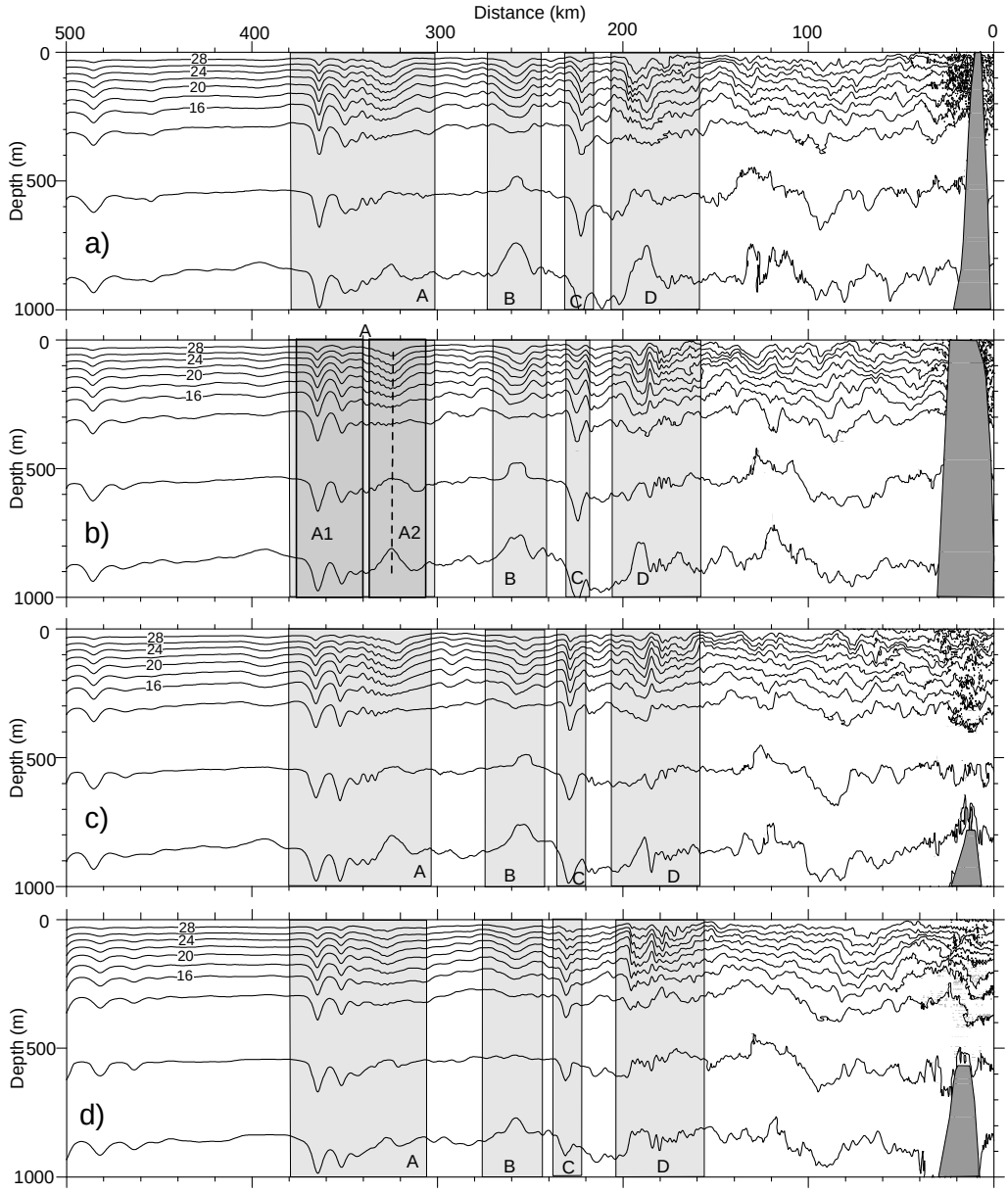

Figure 4.2: Model-predicted temperature fields along four cross-sections after 5 M_2 tidal periods. Panels a-d correspond to the four cross-sections in Figure 4.1. The fragments A-D also correspond to those in Figure 4.1.

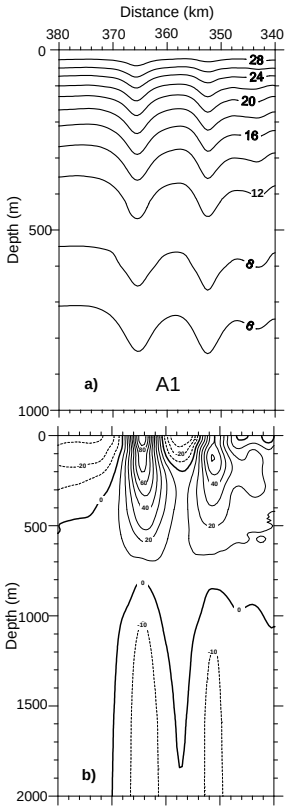

Figure 4.3: Temperature (panel a) and zonal velocity (cm/s; panel b) structures of of two first mode ISWs (see fragment A_1 in Figure 4.2b).

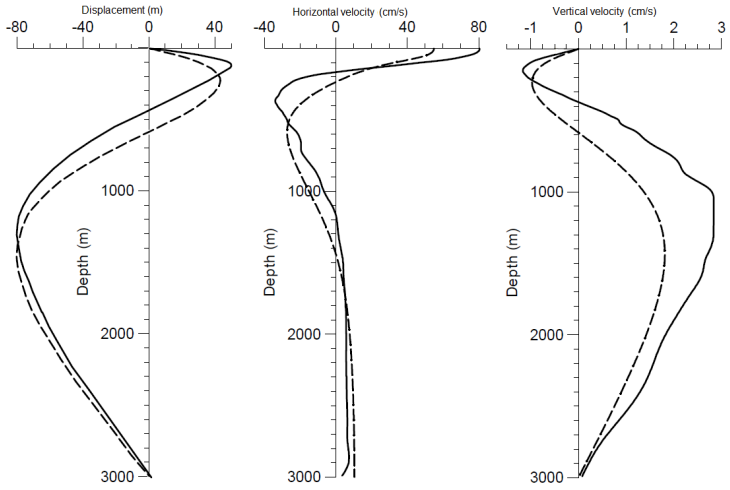

Figure 4.4: Comparison of the vertical profiles (from left to right, wave displacement, horizontal velocity, and vertical velocity) of the second mode ISW (see fragment A_2 in Figure 4.2b) predicted by the model (solid lines) and calculated by a standard eigen value problem (dashed lines).

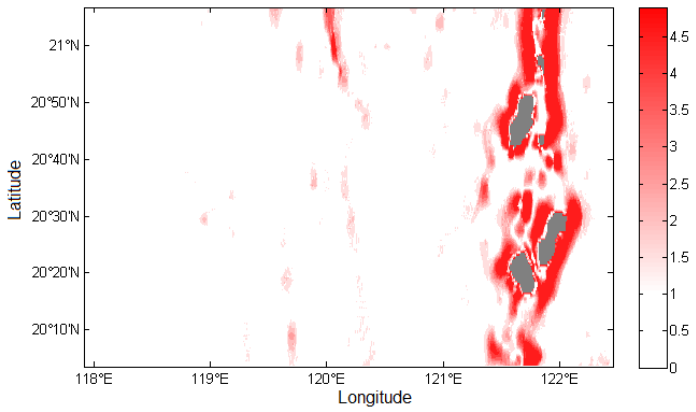

Figure 4.5: Distribution of the slope parameter ε (see explanation in Chapter 2.2.1) calculated for the M_2 tide. To make the figure more readable, values above five are all set to five, and those below unity are all set to unity.

features a value much smaller than unity, implying a regime suitable for the generation of internal tides. On the other hand, the distribution of the slope parameter ε in the LS is plotted in Figure 4.5. As is indicated by its spatial structure, critical and supercritical slopes are primarily aligned along the eastern ridge at LS, especially around the islands, whereas the rest of the strait is mostly under the subcritical condition.

Based on the estimate of ku_0/ω and ε in the LS, the regimes to which the two ridges belong are marked in Figure 2.1. Note that the topographic Froude number $Fr = u_0/Nh_0 >> 1$ for both ridges. It is readily seen from Figure 2.1 that the eastern ridge lies in regimes 4 and 5, whereas the western ridge lies in regimes 1 and 5. This implies that the western ridge is more in a linear internal tide regime and supports the generation of tidal beams. However, the situation is more complicated for the eastern ridge, namely, both internal tides and lee waves prevail; the slope parameter is nearly or far greater than unity, and the topographic Froude number is far greater than unity. The above features indicate that the eastern ridge is favourable for the generation of both linear internal tides and nonlinear, breaking lee waves, thus multiple scenarios are expected in the LS.

To have a full picture of the underwater wave structures, the zonal velocity field along cross-section b of Figures 4.1 and 4.2 is plotted and shown in Figure 4.6. In the figure, M_2 tidal beams, which are emitted from the two ridges and reflected by the upper and lower boundaries, are calculated from the initial stratification and superimposed on the velocity field. By scrutiny of the figure we can see that both ridges are able to radiate prominent tidal beams, which are later reflected at the thermocline and bottom and by nonlinearly interacting with the thermocline, the beams are scattered and ISWs of first and second modes gradually emerge. This feature resembles the findings by Gerkema (2001). Moreover, the distance between two adjacent intersections of the tidal beam with the thermocline is about 125 km, which is exactly the wavelength of the first mode internal tide.

A proper way to look at the generation process and mechanism is to inspect the initial stage of the generation process when the barotropic tide sets in from the state of rest and flows eastwards. Although the first M_2 tidal period is still within the model spin-up time, it is appropriate just to

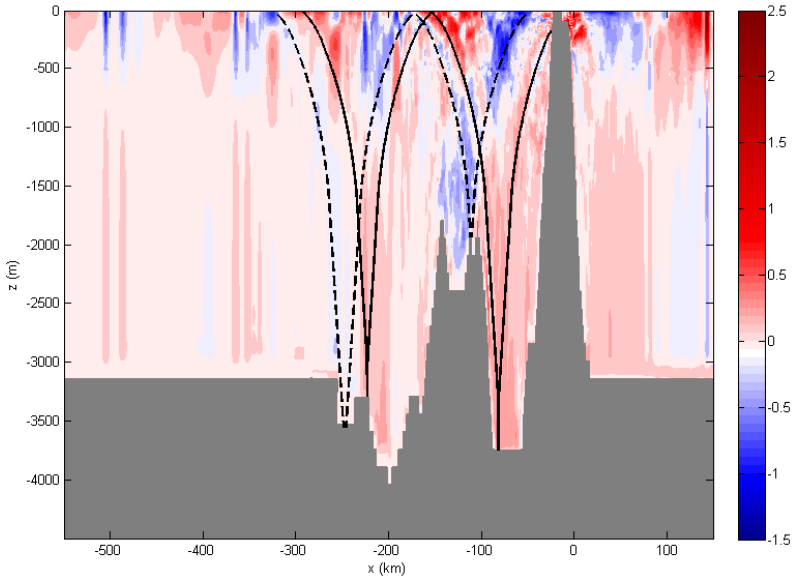

Figure 4.6: Zonal velocity field (m/s) along cross-section b (see Figure 4.1). Superimposed are several radiated tidal beams calculated from the background stratification. Dashed and solid lines correspond to the beams emitted from the western ridge and the eastern ridge, respectively.

see its qualitative feature at this initial stage, given that later wave evolution and the resulting turbulence and mixing will smear the general picture. It is seen that, for a cross-section with an underwater eastern ridge (not intersecting an island), an internal wave of depression is formed at the downstream side of the ridge. This wave is trapped there and grows in amplitude by draining energy from the background flow in the first quarter tidal cycle. However, when the eastward barotropic tide slackens and turns westward, the wave of depression is released and propagate westward. While these waves occur locally near the ridge peaks and much resemble the lee wave generation, meanwhile beyond the generation site, long waves of depression are radiated to both directions, clearly a sign of internal tide generation. The above discussion about the magnitude of ku_0/ω and ε, and the vertical wave evolution and structure all demonstrate features of both internal tides and lee waves, thus it denotes an intermediate case: mixed lee wave regime.

4.4 The effects of the double-ridge topography

The influence of the western ridge on the generation of internal waves has been discussed by a number of papers (Chao et al. 2007, Du et al. 2008, Jan et al. 2008, Warn-Varnas et al. 2009, Buijsman, McWilliams & Jackson 2010, Echeverri & Peacock 2010, Li & Farmer 2011, Alford et al. 2011, Zhang et al. 2011, Buijsman et al. 2012). However, inconsistent conclusions are drawn in terms of if it actually enhances or damps wave generation.

To first understand the separate role played by each ridge in determining the internal wave field near LS, two extra numerical experiments were conducted, each with one ridge truncated. The temperature cross-sections along $20°46' N$ (cross-section b in Figure 4.1) for the reference

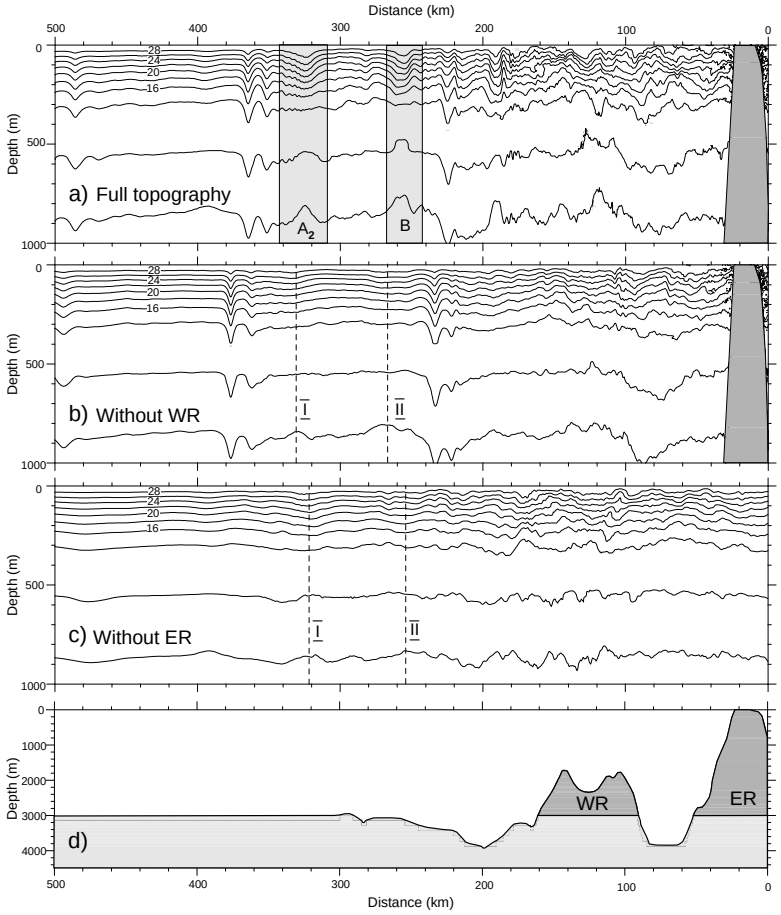

Figure 4.7: Temperature profiles along cross-section b (see Figure 4.1) after 5 tidal periods. The top three panels show the cases of a) real topography; b) without the western ridge; c) without the eastern ridge. The corresponding bottom profiles are shown in panel d.

experiments and the 'truncated experiments' are compared in Figure 4.7. It can be seen from the figure that without the western ridge (panel b), the first mode ISW packet with two waves is essentially unaffected except that it travels farther due to the removal of the blocking effect of the western ridge. Meanwhile, the second mode ISW, which is otherwise trailing the first mode packet in the reference experiment (A_2 in panel a), could hardly be discerned without the western ridge, neither could the other second mode (B in panel a). In the near-field of the generation site, without the western ridge the undulation of the isotherms shows a less high-modal structure and is more smooth.

On the other hand, when the eastern ridge is truncated, a rather different scenario is seen (panel c in Figure 4.7). The large first mode packet in the reference experiment vanishes in this case. Some weak oscillations are barely noticed in the far-field. However, localized above the western ridge, tidal beams emitting from the ridge peaks are obvious, despite that no efficient disintegration of first or second mode ISWs emerges.

Clearly, the total wave field is not merely a linear superposition of the signal generated by each

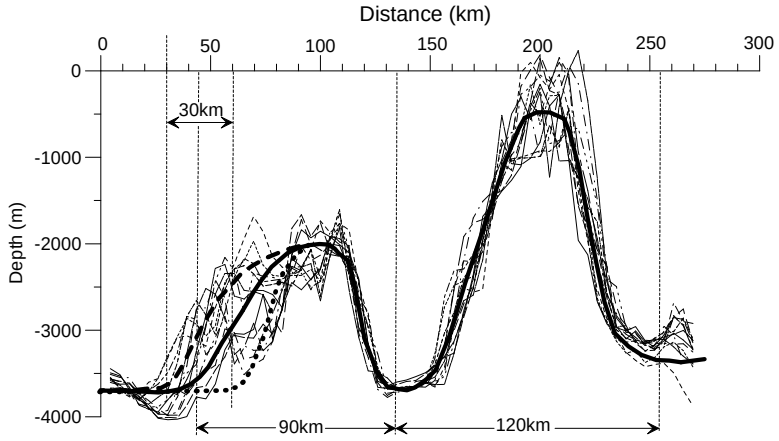

Figure 4.8: Zonal bottom profiles of the LS taken between 20.25° N and 20.75° N. The thick solid line denotes the average bottom profile, with the thick dashed and dotted lines showing the divergence.

ridge. Rather, nonlinear interference and superposition is likely to play a significant role. This is especially apparent for the second mode generation when one of the two ridges is truncated: their linear superposition amounts to a wave signal much weaker than that when both ridges are present. Nevertheless, for the first mode ISW, it is robust from Figure 4.7 that the wave packet is correlated with the eastern ridge and the western ridge plays little role.

The generation of first and second mode ISWs over the two ridges can be explained in terms of a resonant excitement of waves in a double-ridge system and their further nonlinear interference and amplification. A linear analytical model derived by Vlasenko et al. (2005) indicates that, beyond the topography the solution is a superposition of multiple propagating baroclinic modes, which, in terms of vertical displacement $\zeta(x,z,t)$, has the form:

$$\zeta(x,z,t) = \varepsilon_0 \sum_{j=1}^{\infty} a_j g_j(z) exp[i(k_j x - \sigma t + \varphi_j)] \tag{4.2}$$

where $a_j (j = 1,2,3,...)$ and φ_j are respectively the amplitude and phase of the jth baroclinic mode; $g_j(z)$ and k_j are the corresponding vertical profile and wavenumber, defined from a standard eigen-value problem. The small parameter ε_0 is an 'efficient' height of the bottom topography defined as:

$$\varepsilon_0 = \frac{\int_{-H+H_m}^{-H} N(z)dz}{\int_0^{-H} N(z)dz} \tag{4.3}$$

where H and H_m are the total water depth and ridge height, respectively; $N(z)$ is the buoyancy frequency. Detailed formulation and solution of the model are described in detail by Vlasenko et al. (2005).

For the case at LS, due to the remarkable three-dimensionality, a mean bottom profile was obtained by averaging 13 zonal cross-sections across the strait between 20.25° N and 20.75° N with a distance of 2.5′ (Figure 4.8). The dependence of the generated wave amplitude for the eastern ridge (a_j^e) and western ridge (a_j^w) on the ridge width (l) was calculated and the first

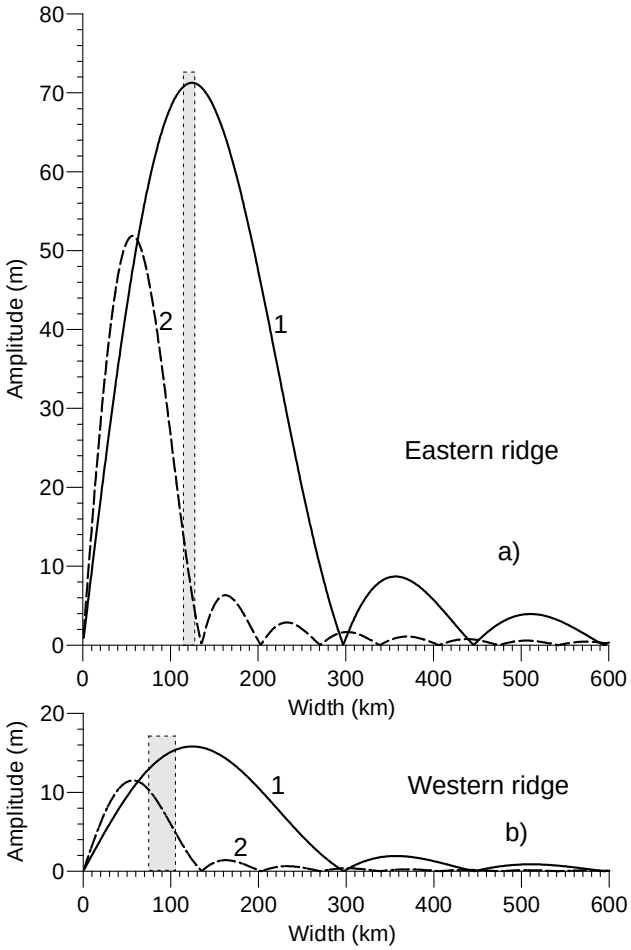

Figure 4.9: Predicted wave amplitudes of the first (solid line) and the second (dashed line) baroclinic modes generated by the a) eastern ridge and b) western ridge, respectively. The gray boxes indicate the likely variation of the ridge widths.

two modes are shown in Figure 4.9. For the eastern ridge and western ridge, l is estimated as 120 ± 5 *km* and 90 ± 15 *km*, respectively. Note that the position of the western ridge varies more significantly than the eastern one and hence exhibits more divergence.

It is evident from Figure 4.9 that wave amplitude $a_j(l)$ reveals clear resonant properties with the varying ridge width. For the eastern ridge with a width of 120 ± 5 *km*, the predicted first mode wave amplitude $a_1^e(l)$ is nearly at the maximum value (71 ± 1 *m*), whereas the second mode wave amplitude $a_2^e(l)$ is close to zero (only 8 ± 4 *m*). This is confirmed by Figure 4.7b in which the second mode is negligibly weak but the first mode is still very pronounced.

In a similar manner, for the western ridge with a width of 90 ± 15 *km*, the analytical prediction reveals weak yet comparable amplitudes of the first mode (14 ± 2 *m*) and second mode (7 ± 3 *m*), which explains the non-existent solitary wave and the clear beams in Figure 4.7c.

For the linear analytical model used here, the resulting total wave field is a linear superposition of the waves generated by the two ridges separately, which can enhance or suppress the total wave field depending on the phase shift $\varphi_j^e - \varphi_j^w$. As is shown in Figure 4.10, the final second mode wave amplitude varies substantially when the waves are in phase ($\varphi_2^e = \varphi_2^w + 2\pi n, n =$

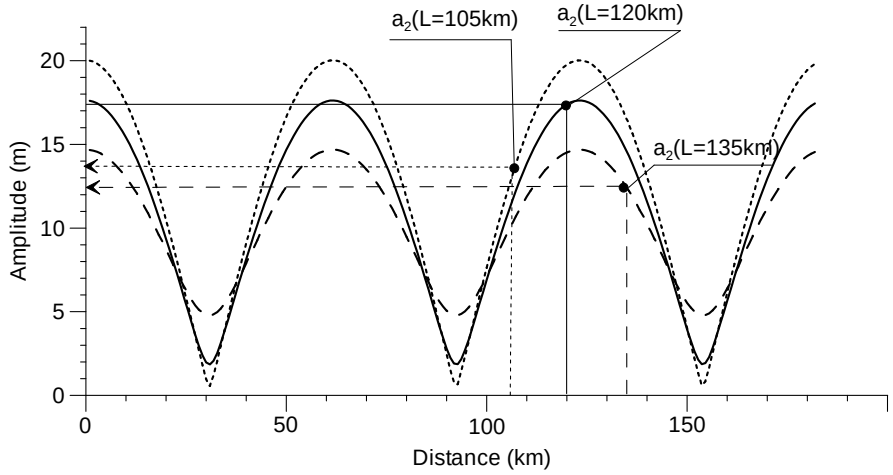

Figure 4.10: Wave amplitude of the second mode internal wave as a function of the distance between the two ridges. The solid, dashed, and dotted lines correspond to the line types in Figure 4.8

$0, \pm 1, \pm 2, ...$) and out of phase($\varphi_2^e = \varphi_2^w + (2n+1)\pi, n = 0, \pm 1, \pm 2, ...$). The distance between the two ridges roughly varies within the range of 97.5 to 112.5 km (Figure 4.8), over which the final wave amplitude variation can be clearly seen from Figure 4.10.

4.5 Sensitivity of the wave field to the basic controlling parameters: magnitude and frequency of the tidal forcing, stratification, and three-dimensionality

A couple of sensitivity experiments were conducted to explore the impacts of tidal forcing strength and frequency, stratification, and 2D/3D modelling. Figure 4.11a illustrates the response of the generated wave fields to three forcing strengths. It is seen that a reduction of 25% of the forcing leads to a slight weakening of the generated waves, but the essential features, including the high modal structures in the near-field, remain unaltered. However, a four-fold reduction of the tidal forcing could cause a substantial reduction of the wave signal. Solitary waves and high modes are nearly absent in this case.

Winter stratification (as shown in Figure 1.6) was implemented as a sensitivity experiment and the results are compared against the case with summer stratification in the reference experiment, as is shown in Figure 4.11b. Surprisingly, the comparison does not reveal any prominent discrepancy; ISWs in winter are slightly larger and travel more slowly that those generated in summer. This is contradictory to the SAR observations (Zheng et al. 2007) and in situ measurements (Yang et al. 2009, Ramp et al. 2010), which shows a much lower occurrence rate of ISWs in winter. However, Zheng et al. (2007), Huang et al. (2008) claimed that the low occurrence of ISWs on SAR images in winter has to do with frequent unfavorable high sea states that are likely to result in an underestimation of the number of ISWs captured.

Figure 4.11c illustrates the wave response to K_1 tidal forcing with the same strength. Not surprisingly, the wave field is fairly weak, due to that the location of the LS is close to the critical latitude of K_1 tide (about 30° N), above which wave group speed approaches zero and wave energy is not carried away from the generation site. Nevertheless, the effects of diurnal tides should never be neglected. Essentially, it modulates the timing of the propagating ISWs and leads to the appearance and alternation of A and B waves, as will be more thoroughly

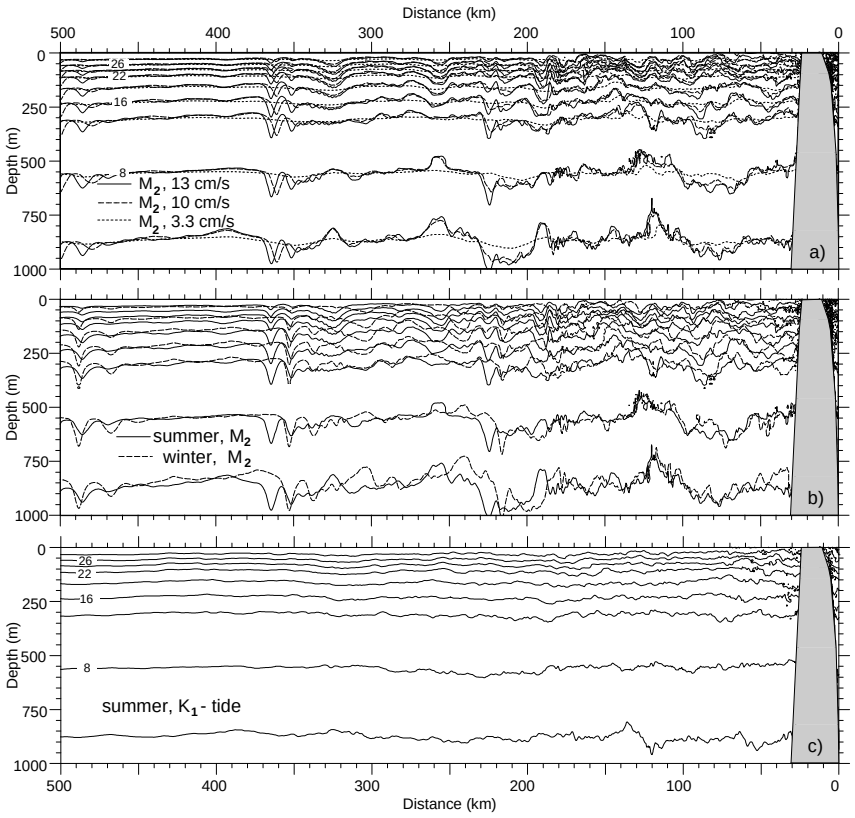

Figure 4.11: Vertical temperature fields along cross-section b in Figure 4.1 after 5 M_2 tidal periods. Sensitivity experiments are for a) three types of tidal forcing of different strength; b) summer and winter stratification; c) K_1 tidal harmonic.

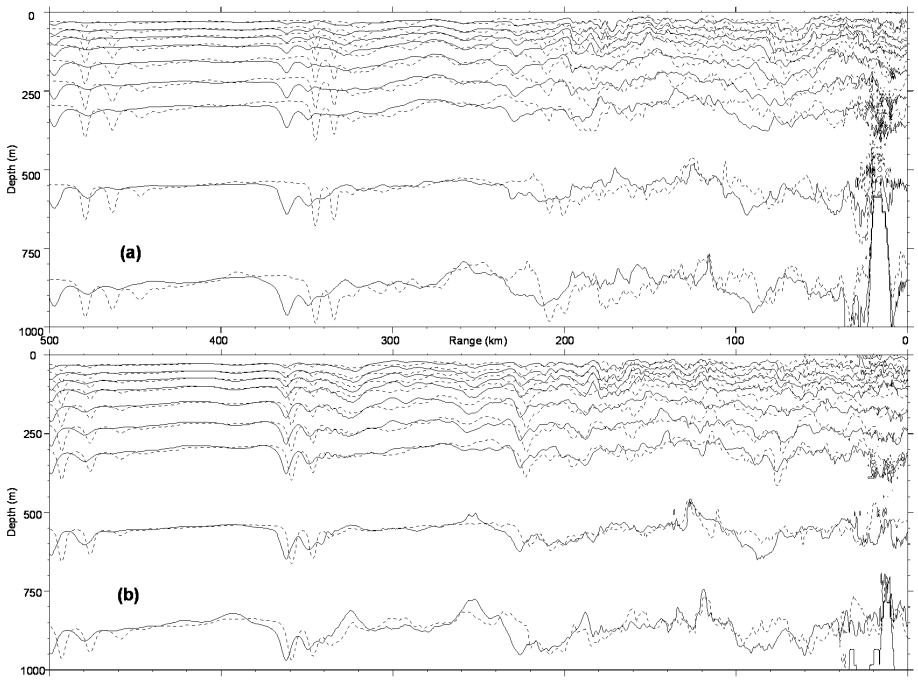

Figure 4.12: Comparison of the vertical temperature structures for the 2D (dashed line) and 3D (solid line) case after 5 M_2 tidal periods. Panels a and b correspond to cross-sections c and d in Figure 4.1, respectively.

inspected in Chapter 6.

From the 3D sea surface signature in Figure 4.1 and the corresponding underwater cross-sections (Figure 4.2) it can be seen that in the far-field the wavefront is nearly straight and homogeneous, which is inconsistent with SAR observations. The reasons can be attributed to the uniform water depth (3000 m) in the far-field, inaccurate representation of tidal forcing, and no implementation of Kuroshio, etc. However, 3D wave generation in the near-field is quite pronounced. In 3D cases, barotropic wave flows around the islands and floods into the channels, which augments the tidal flow between the islands. Also, uncertainties are added due to the sloping flanks of the islands. To see the discrepancy between 2D and 3D simulations, a couple of 2D experiments were performed and compared with the corresponding 3D cross-sections. In Figure 4.12, cross-sections c and d of Figure 4.1 after 5 M_2 tidal cycles were chosen. The isotherms display apparent disparities along cross-section c: in the 2D case, the ISW packet formed at the far-field has larger amplitude but spatially lagged the 3D case; in the near-field undulations are overall similar, and there is also a phase lag. On the other hand, the discrepancy along cross-section d is much less notable: the waves in the 2D case are slightly larger and slower. Hence, the above discussion reveals the 2D/3D discrepancies in wave amplitude and phase and highlights the necessity of 3D modelling.

4.6 Summary of the spatial structure of baroclinic tides

In this chapter 3D modelling of baroclinic tides in the northern SCS was presented, with the main focus on the wave generation mechanism and the multi-modal structures. A pronounced baroclinic tidal bore with inclined isopycnals (as will be shown later in Chapter 5) is formed

just west of the western ridge due to the superposition of internal wave fields generated by the two ridges. This tidal bore subsequently disintegrates into several types of wave forms. A huge (120 m) first mode ISW first forms and gets detached from the bore, followed by a clear second mode ISW (80 m). Both waves are compared with the KdV solutions and it shows reasonable agreement, confirming the robust existence of such multiple modes. Some short waves ride on the second mode ISW and propagates with the same phase speed, and this will be scrutinized in Chapter 5.

An interesting result was obtained in a series of experiments that aimed to identify the role of the eastern and western ridges in the generation process. It was found that without the western ridge, the eastern ridge can generate a first mode ISW packet in the far-field that is nearly as strong as that with the two ridges. However, the generated higher modes are much weaker and can hardly be spotted. This is unexpected, given that the eastern ridge is very tall and steep and is expected to radiate high-modal waves. An explanation was found in terms of a linear resonant theory of internal wave generation. The analytical solution shows that the average width of the eastern ridge is close to the value when the generation of the second mode wave is inhibited. At the same time, the analytical solution predicts comparable amplitudes of the first and second modes that are generated by the western ridge. Though both small, superposition of the two modes is able to produce obvious tidal beams above the western ridge, but no solitary waves can form beyond the generation site. In fact, the second mode wave signals produced by the two ridges interfere in the far-field, and their nonlinear superposition is substantially stronger than the two separate signals.

Chapter 5

Simulation and observational evidence of short-scale internal waves

[1]

In Figure 4.2 of Chapter 4 one can spot some short internal waves that are carried by a second mode ISW (for example, fragment A_2 in panel b). These short waves have wavelengths of about 1.5 km and amplitudes of 20 m, and only appear in the upper 500 m. In this chapter, the emerging processes and the underlying mechanisms are presented, with the corroboration from SAR images.

5.1 Model prediction of short internal waves trailing strong internal solitary waves

Before the discussion of the detailed generation process of the short internal waves, how they look in the numerical simulations is first shown in Figure 5.1 for the time t=2.875 M_2 tidal periods (=35.65 h). Panel a shows a map of the gradient of the simulated surface currents u in x-direction (du/dx) in the area $119°50' - 120°25'E$ and $20°0' - 21°5'N$. The modulation of the backscattered radar power and thus of the SAR image intensity (assuming a linear relationship between backscattered radar power and SAR image intensity) is proportional to the surface current gradient in the look direction of the SAR antenna (Alpers 1985). The map depicted in panel a can be viewed as a SAR image of an internal wave field at which the SAR antenna looks either from the left or the right onto the imaged area. Panel a shows to the west the sea surface signature of a long-crested ISW and to the east of the sea surface signatures of a packet of short internal waves. The distribution of du/dx along the transect $20°47'N$ (dashed line inserted in panel a) is depicted in panel b. It shows that the values of du/dx caused by the short internal waves are of similar strength as the ones caused by the frontal ISW. The depth profile of temperature depicted in panel c, which is taken along the same transect, shows that the internal wave field consists of a strong first mode ISW (amplitude 120 m), followed by a second mode ISW (amplitude 80 m) on which short first mode internal waves ride. A close-up view of the short waves is shown in Figure 5.2. It can be seen that the short internal waves have wavelengths of approximately 1.5 km and amplitudes of approximately 20 m. They are confined to the upper water layers down to a depth of about 500 m. Although these internal waves have shorter wavelengths and smaller amplitudes than the first mode ISW, they are associated with large surface current gradients (du/dx) that have the same order of magnitude as the ones of strong ISWs. This is the reason why they are associated with similar large modulations of the sea surface roughness as the ISWs and thus with a similar strong modulation of the radar backscattering. This renders them as clearly visible on SAR images as ISWs.

Analyses of the numerical runs reveal that these short internal waves are generated by two mechanisms: (i) the disintegration of a baroclinic bore, which is generated by the interaction

[1] This chapter is mostly based on the paper Guo et al. (2012)

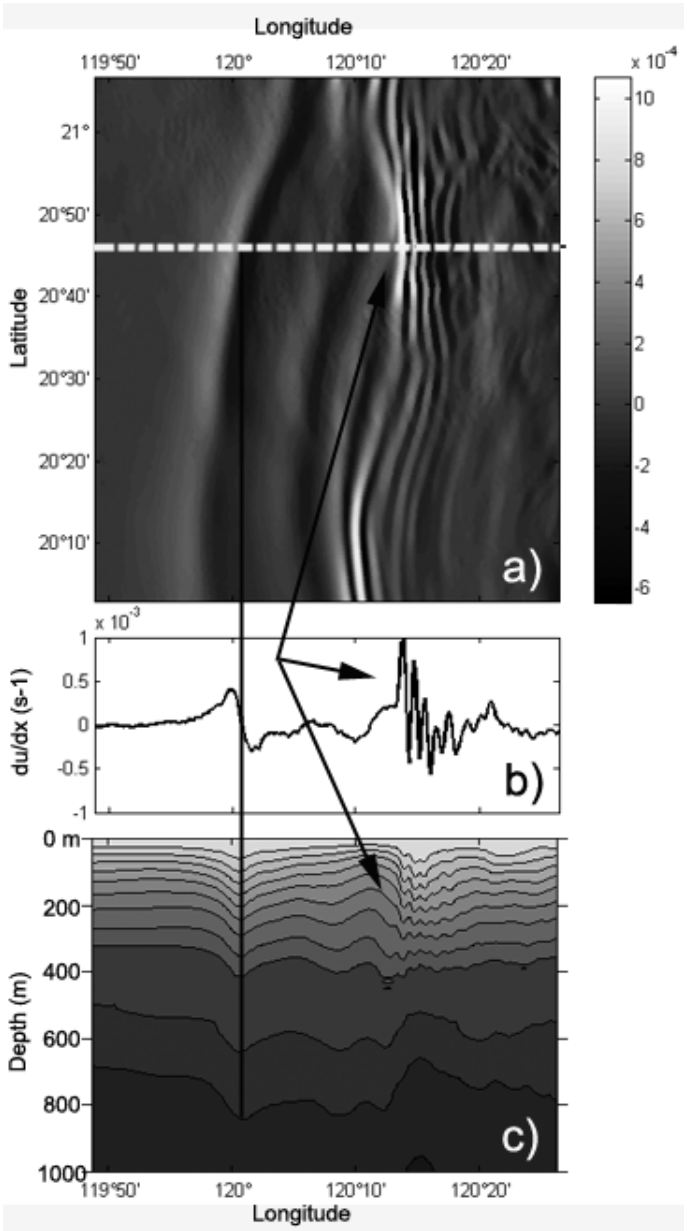

Figure 5.1: Simulated internal wave field after t=2.875 M_2 tidal periods. Panel a: Two-dimensional map of the simulated surface current gradient du/dx (s^{-1}) in x-direction (the horizontal direction) in the area $119°50' - 120°25'E$ and $20°0' - 21°5'N$. Panel b: Variation of du/dx along the transect $20°47'N$ marked by a bright dashed line in Panel a. Panel c: depth profile of temperature along the same transect. The x-coordinates are the same in all the three panels. The vertical solid line marks the location of the leading first mode ISW, whereas the three arrows indicate where the short internal waves are located.

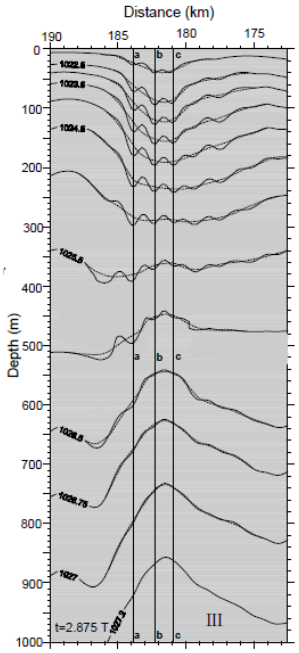

Figure 5.2: A close-up view of the structure of the short waves in Figure 5.1c. Shown are the isopycnals in the upper 1000 m. The dashed lines are the mean isopycnals of a second mode ISW after removal of the short waves. The three vertical lines bound two short waves.

of the tidal currents with the two-ridged topography of the LS. Short internal waves of this mechanism appear between 120°6′ and 120°30′E, which is entitled the near-field (Area N in Figure 1.3); (ii) the nonlinear interaction between the first and second mode ISWs when the faster first mode ISW overtakes the frontal second mode ISW of the previous tidal cycle. This occurs between 118°24′ and 119°6′E, which is entitled the far-field (Area F in Figure 1.3).

5.2 Generation mechanisms and spatial structure

The generation process of short internal waves in the near-field is illustrated in Figure 5.3. At the beginning of the tidal cycle, a baroclinic bore is formed just west of the western ridge of the LS, between 120°30′ and 120°50′E (shown by the dashed line in panel a). The bore consists of a large number of internal modes. The first mode being the fastest mode detaches from the tidal bore quickly (fragment 1 in panel b) and the second mode starts to leave the bore with the rest of the higher modes during the next three hours (fragment 2 in panel b). A quarter tidal period later (panel c), the second mode ISW, on which first mode short internal waves ride, can clearly be seen between 120°10′ and 120°30′E (fragment 2 in panel c). These short internal waves are generated during the disintegration of the baroclinic bore and travel with the same speed as the second mode carrier wave.

Since the first mode ISW travels faster than the second mode ISW, it will at some stage overtake the second mode ISW that was generated one tidal cycle earlier. The generation of short internal waves in the far-field after such a collision is illustrated in Figure 5.4. Panel b shows the depth profile of temperature as a function of longitude when the first mode ISW propagates (phase velocity c_1) behind the second mode ISW (phase velocity c_2) at the time t=4.125 M_2 after

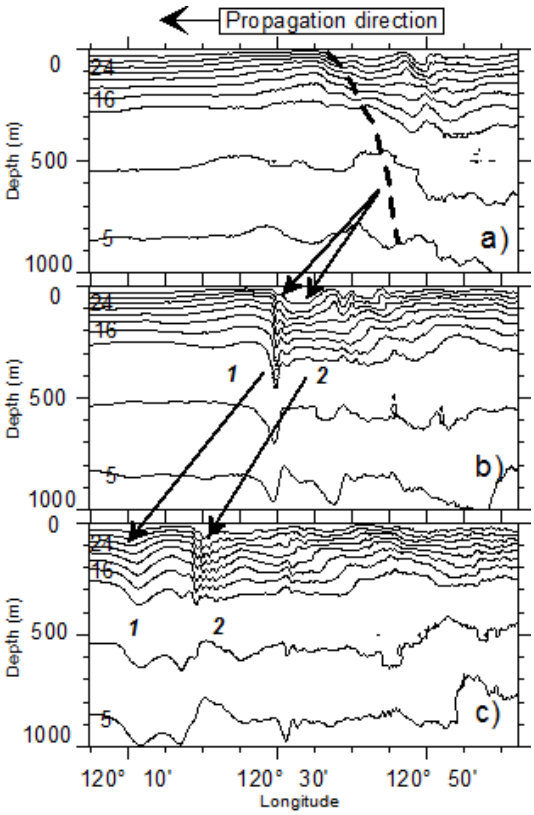

Figure 5.3: Simulated depth profile of temperature as a function of longitude showing the short internal wave field in the near-field for three different times. Panel a: t=2.25 M_2; panel b: t=2.5 M_2; and panel c: t=2.75 M_2. The dashed line in panel a denotes the tidal beam located west of the western ridge, whereas the numbers 1 and 2 in panels b and c denote the detachment of first and second mode ISWs. This figure shows how the short internal waves are generated by the disintegration of a baroclinic bore.

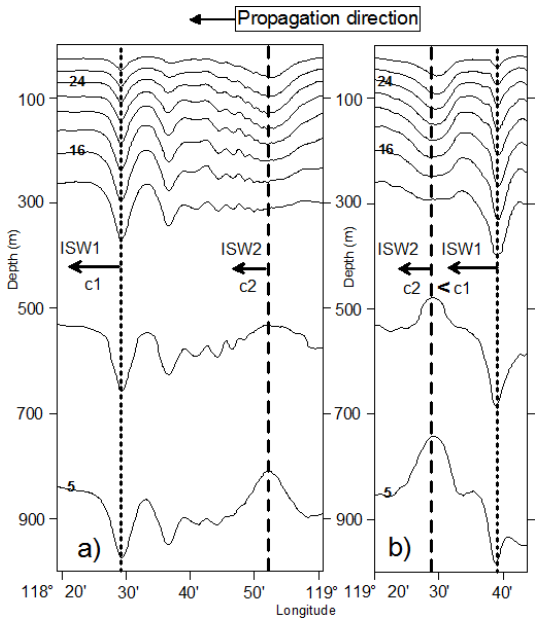

Figure 5.4: Simulated depth profile of temperature as a function of longitude for the upper 1000 m showing the generation of short internal waves in the far-field at two different times. Panel a: t=5 M_2 after the collision and panel b: t=4.125 M_2 before the collision. Note that the waves propagate leftward, and the dashed and dotted lines mark the center of the second and the first mode ISWs, respectively.

the run started ($c_1 > c_2$). Weakly nonlinear theory predicts that two colliding ISWs interact elastically and keep their individual shapes after collision (Zabusky & Kruskal 1965). However, for strongly nonlinear ISWs, as in this case, energy may leak into the other frequency bands. Such leaking can be seen in panel a, which shows the depth profile of temperature after the first mode has overtaken the second mode ISW. At this time the short internal waves riding on the second mode are fully developed.

5.3 Theoretical explanation

In order to get an insight into the physical mechanism causing the generation of the short internal waves riding on the second mode ISW, the Taylor-Goldstein equation that includes a background current $U(z)$ is considered:

$$\frac{d^2\psi_j}{dz^2} + \{\frac{N^2(z)}{(U(z)-c)^2} - \frac{U''(z)}{U(z)-c} - k^2\}\psi_j = 0 \tag{5.1}$$

Here z is the vertical coordinate, $N^2(z)$ is the square of the buoyancy frequency, c is the phase speed, ψ_j is the eigenfunction describing isopycnal displacement of the jth mode ($j = 1,2,3...$), and k is the wavenumber that can be estimated directly from the scale of the short waves. The boundary conditions at the surface and bottom (H) are:

$$\psi_j(0) = \psi_j(-H) = 0, j = 1,2,3,... \tag{5.2}$$

With the boundary conditions (5.2), equation (5.1) has eigenfunction solutions with discrete

eigenvalues c_j (wave speeds). The character of the solution is sinusoidal-like when the term in the curly brackets of (5.1) is positive and exponential-like when it is negative. Transition from the layers with positive values to the depth where the term is negative leads to the change of the character of the solution from oscillatory to exponential form. This transition is caused by the shear current profile $U(z)$ associated with the second mode ISW. In the simulations reported in this paper current reversal occurs at a depth of about 180 m (see Figure 4.4).

The values for the buoyancy frequency $N(z)$ and shear current $U(z)$ were taken from the middle of the second mode internal wave. The eigenvalue problem (5.1)-(5.2) was solved numerically with these values inserted. The solution shows that the eigenfunction ψ_j is nearly sinusoidal above 500 m, and decays exponentially below this depth. Similarly, the presence of short internal waves above 500 m and their decay below 500 m can be seen in Panel c of Figure 5.3 and Panel a of Figure 5.4.

Thus the existence of short internal waves riding second mode ISW has been confirmed by numerical modeling with the MITgcm and by solutions of the Taylor-Goldstein equation. Below observational evidence for the existence of short internal waves trailing strong ISWs in the northern SCS will be presented by using SAR images acquired by Envisat.

5.4 Observational evidence of short internal waves

As was introduced in section 3.2, SAR imagery gives information on internal waves via the variation in the sea surface roughness induced by internal waves. Internal waves are associated with horizontal gradients of the surface current velocity, which cause modulations of the sea surface roughness and thus leads to spatial variations of backscattered radar signal (Alpers 1985). This gives rise to characteristic wave patterns visible as image intensity modulations on SAR images. In convergent flow regimes, the SAR image intensity is increased, while in divergent regimes it is decreased. The caveat is that the surface films, which can damp Bragg waves efficiently, could play a substantial role in SAR signatures of internal waves (Da Silva et al. 1998), especially for those with short scales or in areas of high productivity (Pan et al. 2012). An ISW of depression shows up on SAR images as a bright band in front (with respect to the propagation direction) followed by a dark band. This sequence is reversed for an ISW of elevation. Typical values of surface current gradients associated with ISWs detectable by SAR are $10^{-4} - 10^{-3} s^{-1}$ (Alpers 1985).

Intuitively, one would expect that short internal waves will cause only very weak sea surface roughness modulations in comparison with ISWs with longer wavelengths and much larger amplitudes, and would be barely detectable by SAR. However, the simulations have shown that this is not the case. The convergences and divergences of the surface velocity field, induced by the short internal waves riding on a second mode ISW, are strong enough to cause strong modulations of the SAR image intensity. Indeed, they are of the same order as those of ISWs of longer wavelengths and larger amplitudes (see Panel b of Figure 5.1). Therefore short internal waves should be clearly visible on SAR images.

The Envisat ASAR archive of the European Space Agency (ESA) has been screened for sea surface signatures of short internal waves trailing a strong ISW in the northern SCS. A number of images were found showing this phenomenon. All ASAR images were acquired in the Wide Swath Mode and have a resolution of 150 m and a swath width of 405 km.

Sea surface signatures of short internal waves trailing a first mode ISW were encountered almost

always (with two exceptions) in the two distinct areas marked N and F in Figure 1.3. This is in agreement with model calculations.

Below six SAR images acquired by Envisat ASAR are compared in detail with model results. However, it should be noted that the coincidence between internal wave fields obtained from numerical modeling and from SAR images cannot be perfect because of the great variability of the oceanic conditions affecting the generation and propagation of internal waves captured by SAR images. The restriction of the model domain to the longitude band $20^\circ - 21^\circ N$ is not essential since the strong ISWs in the images are observed in this longitude band in deep water. Furthermore, it is also expected that the reduction of the tidal forcing to the semidiurnal tide has only a small effect on the modeled internal wave fields since they are forced mostly by the semidiurnal tide rather than by the diurnal tide (see Chapter 6).

Despite all of the above-mentioned uncertainties and limitations, the comparison between the ISW's features observed on the SAR images and obtained in model calculations provides sufficient evidence that short internal waves trailing strong ISW found in numerical modeling really do exist in the northern SCS. In the next two subsections six SAR images which substantiate this statement will be presented.

5.4.1 Short waves in the near-field

According to the modeling results, the short internal waves in the near-field are generated by the disintegration of an internal bore and are encountered in the longitude band $120^\circ 6' - 120^\circ 30' E$ (Area N in Figure 1.3).

To find the wavelength of ISWs and distance between the frontal ISW and the trailing short waves, the SAR image depicted in Figure 5.5 was analyzed. It was acquired at 0159 UTC on 9 July 2005 and is a typical example of a SAR image showing sea surface signatures of a first mode ISW followed by a packet of short internal waves. The zoom on the packet of short internal waves depicted in Panel b reveals that the waves in the packet do not have a uniform wavelength. The wavelength of the short internal waves in the packet was estimated along two transects marked by white lines in Panel b. For this, several sampling points on the bright lines along both transects have been chosen. The average wavelength along the upper transect was determined to be 0.85 km and along the lower transect to be 1.53 km. These values lie well within the range of the model predictions. Note that, unlike usual ISW packets, which consist of strictly rank-ordered solitary waves with decreasing amplitude and decreasing distance between the waves from front to rear in the packet, the short internal wave packets show a much less rank-ordered structure. The non-rank-ordered structure of the waves in the packet is clearly seen in Figure 5.1. In addition, the distance between the first mode ISW and the first short wave in the packet is 23 km (Figure 5.5). Also this distance lies well within the range of the model predictions (see Figure 5.1).

Figure 5.6 shows two more examples of SAR images with sea surface signatures of a first mode ISW followed by a packet of short internal waves (both images overlaid into one). The background image was acquired at 0150 UTC on 18 May 2007, and the inset is an ASAR image acquired at 1358 UTC on 16 May 2007. The internal wave fields visible on these two SAR images propagate in different directions: one westward and the other southwestward, as indicated by the inserted two thick black arrows. Short internal waves in both SAR images can be easily recognized (see the two thin black arrows). The wavelengths of the short internal waves were estimated to lie between 1.0 and 1.5 km. This value, together with the value of 25

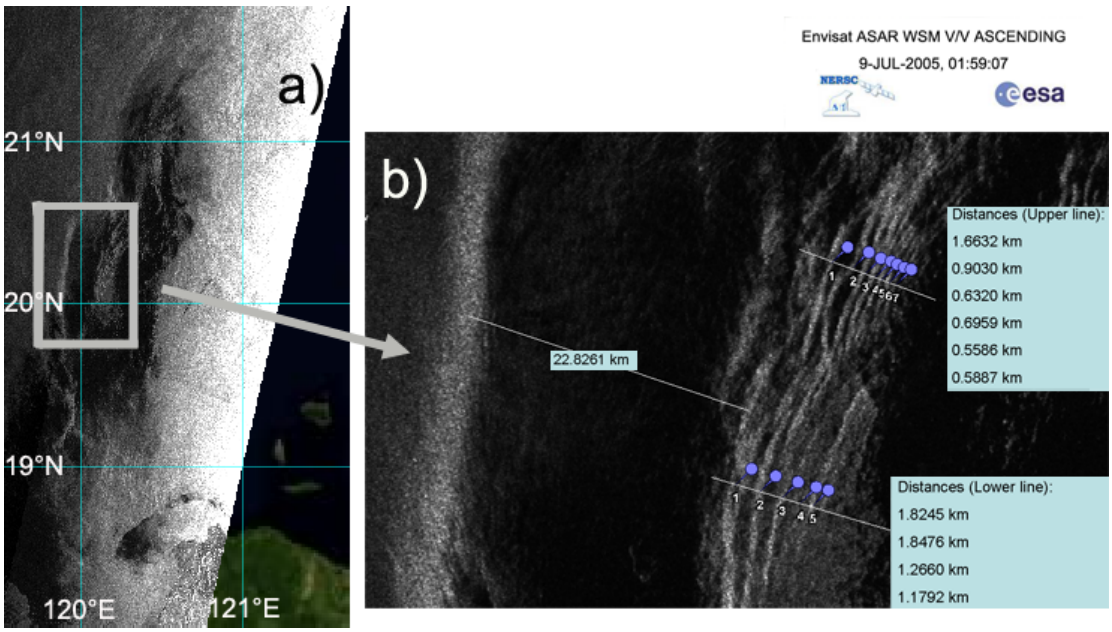

Figure 5.5: ASAR image acquired at 0159 UTC on 9 July 2005 over the near-field. Panel b shows a zoom on the wave pattern on which sea surface signatures of a first mode ISW followed by a packet of short internal waves are visible.

km for the distance between the first mode ISW and the first wave in the short wave packet, lies well within the range of the model predictions.

In situ measurements (Alford et al. 2010, Ramp et al. 2010) and numerical simulations (Vlasenko et al. 2010, Zhang et al. 2011) show that single long-crested ISWs are normally encountered only in the deep basin west of the LS. Packets with multiple ISWs are usually encountered near the shelf break, where ISWs interact with the shallow bottom topography and generate new internal waves. However, wave packets with multiple ISWs have also occasionally been observed on SAR images close to the LS near $120^{\circ}E$ (Zhao et al. 2004, Liu et al. 2006).

Panel a of Figure 5.7 shows such a packet with four ISWs close to the LS (see the black box). The zoom on the packet depicted in Panel b shows sea surface signature of a packet of short internal waves that follow the first mode ISW packet (thin black rectangle at the bottom of Panel b). This ASAR image was acquired at 0150 UTC on 11 August 2006 close to the LS near $120^{\circ}E$. Liu et al. (2006) have presented in their paper an image (their Figure 2) showing a similar internal wave pattern in this location together with in situ data. On their image, a wave packet with at least four bright lines is visible. The leading ISW in the packet has a crest length of more than 100 km, and subsequent ISWs have decreasing crest lengths. On our ASAR image of 11 August 2006 (Figure 5.7), the distances between two adjacent ISWs in the packet are 8.1, 6.1, and 4.1 km (see the four black dots along the transect marked black in Panel b). The short internal waves in the black box in Panel b have an average wavelength of 1.6 km. The packets of ISWs and short internal waves are located in the near field (area N in Figure 1.3).

According to the TPXO7.1 model (Egbert & Erofeeva 2002), the SAR image of 11 August 2006 (Figure 5.7) and the one of Liu et al. (2006) of 2 May 2005 were taken at spring tide when the semidiurnal tidal current was at its maximum. As was mentioned earlier, it is semidiurnal

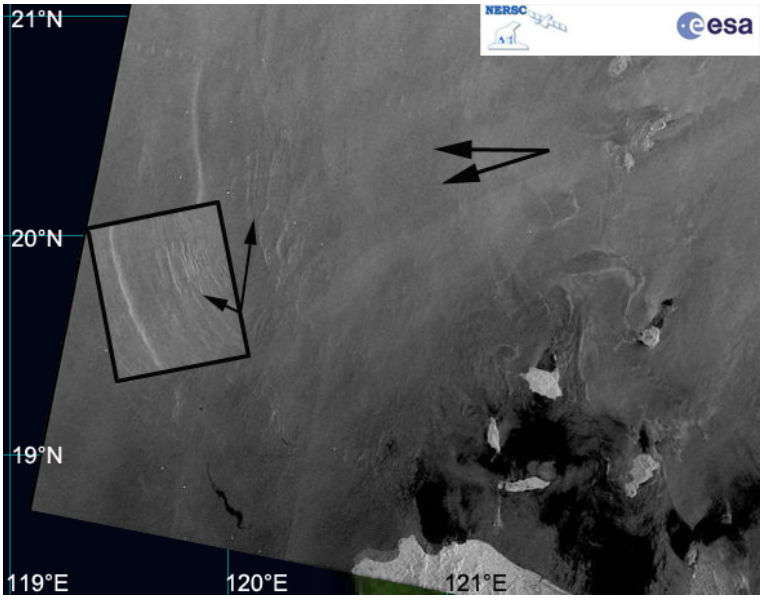

Figure 5.6: Overlay of two ASAR images acquired over the near-field. The background ASAR image was acquired at 0150 UTC on 18 May 2007, and the inserted one (in the rectangular box) at 1358 UTC on 16 May 2007. It shows on both images sea surface signatures of a first mode ISW followed by a packet of short internal waves.

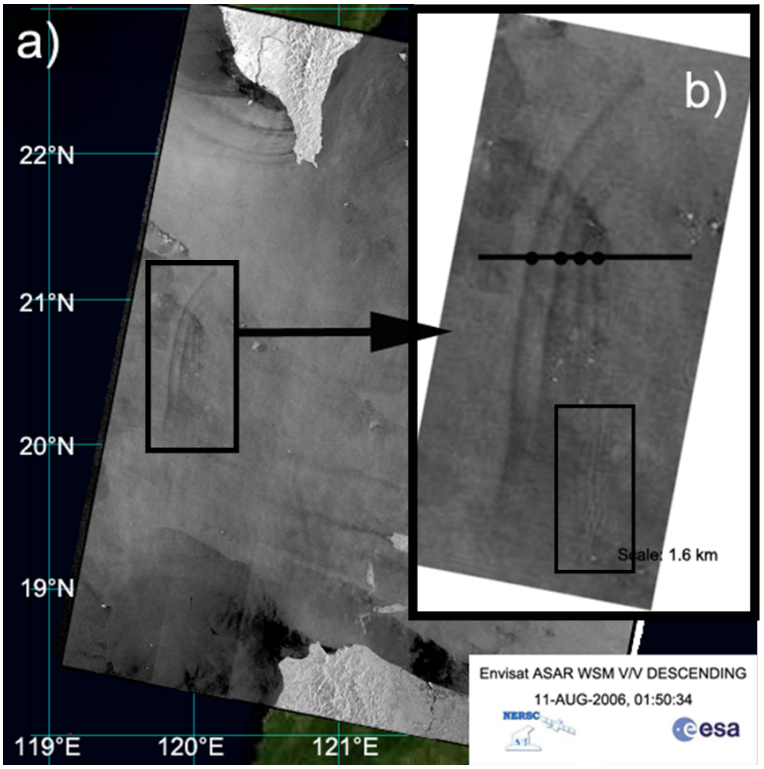

Figure 5.7: ASAR image acquired at 0150 UTC on 11 August 2006 close to the LS. The zoom on the wave pattern (Panel b) shows sea surface signatures of a wave packet with 4 ISWs and below, in the black rectangular box, a packet of short internal waves. ISW packets with multiple ISWs are rarely detected near the LS.

tide rather than diurnal tide that mainly determines the formation of ISWs in the northern SCS. Thus, a possible explanation for the generation of ISW packets in this area is that they were generated by an exceptionally strong semidiurnal barotropic tidal current in the LS. This is plausible because, according to the linear theory of internal tides generation (Baines 1973, Vlasenko et al. 2005), larger forcing leads to larger internal tides, which then disintegrate more easily into ISW wave trains due to nonlinear and non-hydrostatic effects.

Taking into account that the above experiments used the M_2 tidal forcing as predicted by the TPXO 7.1 model, it is clear that the amplitude of the generated internal waves would be larger if a stronger barotropic current was included in the model. In order to verify this hypothesis, a 2D simulation with 30% enhanced barotropic forcing and averaged bathymetry (between 20° and 21°N) was carried out. The results show that the baroclinic tides are subject to stronger nonlinearity, causing the generation of an ISW train before it reaches the western ridge of the LS. This wave train strongly interacts with the baroclinic bore that was previously formed west of the western ridge, causing reinforcement during the interaction process. Furthermore, the short internal waves riding on a second mode ISW have scales somewhat larger than those generated under normal tidal conditions. Figure 5.8 shows results of these simulations. In the lower panel the depth profile of temperature down to a depth of 1000 m is depicted, and in the upper panel the corresponding variation of du/dx (in s^{-1}) is shown. The x-coordinates are the same in the two panels. The plots depicted in Figure 5.8 show a large amplitude first mode ISW followed by a first mode ISW of smaller amplitude (see the two vertical dashed lines in Panel a), and then followed by a complex structure, which is the consequence of the superposition of high modal bands due to the strong nonlinear interaction of the first and the second mode ISWs. The two ISWs and this multi-modal structure produce strong current convergences and divergences at the sea surface. The convergences manifest themselves as the four peaks visible in the plot of the du/dx (see the four vertical dashed lines in Panel a). The distances between these four peaks are 11, 6.5, and 3 km (which, incidentally, are the similar distances as measured between the ISWs in Figure 5.7). The multi-modal structure is then followed by a second mode ISW on which short internal waves ride. As shown in Figure 5.1 (Panels a and b), also in this case, the short internal waves give rise to strong modulations of the surface current gradient field (see the dashed box in Panel a), which renders them visible on SAR images.

5.4.2 Short waves in the far-field

According to modeling results, packets of short internal waves trailing ISWs should also be present in the northern SCS in the longitude band between 118°24′ and 119°6′E (area F in Figure 1.3), where they are generated by nonlinear interaction between first and second mode ISWs when the faster first mode ISW overtakes the frontal second mode ISW generated in the previous tidal cycle. In this subsection two ASAR images showing observational evidence of this phenomenon in area F will be presented.

Figure 5.9 shows surface signature of solitary waves at 1407 UTC on 7 July 2005. The zoom on the black rectangle (Panel b) shows clearly three wide ISWs followed by a packet of short internal waves. The average wavelength of the short waves in the packet is approximately 1.5 km.

The results of the numerical modeling in the far field are shown in Panels c and d of Figure 5.9. Panel c shows the two-dimensional map of the simulated surface current gradient du/dx (in s^{-1}) in x-direction (horizontal direction) and Panel d shows its variation along the transect 20°40′N

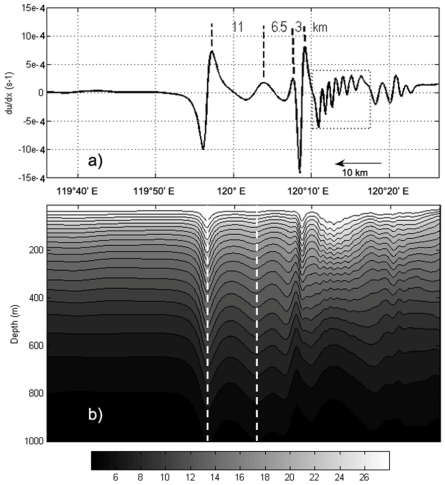

Figure 5.8: Simulated two-dimensional internal wave field near the LS at t=3 M_2, with the 30% larger barotropic tidal forcing and averaged bathymetry (between 20° and 21°N) in the model runs. Panel a shows the variation of $du/dx(s^{-1})$, and Panel b shows the corresponding depth profile of temperature down to a depth of 1000 m. The four vertical dashed lines in Panel a indicate the peaks of $du/dx(s^{-1})$, whereas the two vertical dashed lines in Panel b indicate where the first mode ISWs are located. The x-coordinates are the same for both panels.

(as is marked by a black line in Panel c). The simulation depicted in Panels c and d of Figure 5.9 shows the internal wave field after the collision of the first mode ISW with the second mode ISW (after five M_2 tidal periods). In Figure 5.4 are shown the depth profiles of temperature for the upper 1000 m before the collision (Panel b, t=4.125 M_2) and after the collision (Panel a, t=5 M_2). The depth profile of temperature depicted in Panel a of Figure 5.4 refers to the same time as the plots depicted in Panels c and d of Figure 5.9. Comparison of the SAR image intensity field depicted in Panel b of Figure 5.9 with the simulated surface velocity gradient field depicted in Panel c of Figure 5.9 shows an overall good correlation of the wave structures. However, while the average wavelength of the short internal waves on the SAR image is 1.5 km, it is 2.5 km in the simulations, which is still considered to lie within the margin determined by the uncertainties in the input parameters for the simulations. Furthermore, the wave field visible on the SAR image exhibits much more variability in the meridional direction than the simulated wave field, which can be attributed to the fact that ideal barotropic forcing and constant water depth in the deep basin were used in the simulations.

The ASAR image depicted in Figure 5.10, which was acquired at 1410 UTC on 21 June 2005, shows a strong ISW with a crest length of more than 200 km followed by a packet of short internal waves, whose wavelengths vary between 1 and 2 km, which is also in agreement with model predictions.

5.5 Summary of characteristics of short internal waves

About two decades ago Akylas & Grimshaw (1992) theoretically investigated the resonant effect of high mode ISWs with secondary short waves at the tail. They showed a striking acoustical image of such a phenomenon that occurred in nature, in which a second mode and some secondary wave ripples are coupled and propagate in resonance with the same speed. The underly-

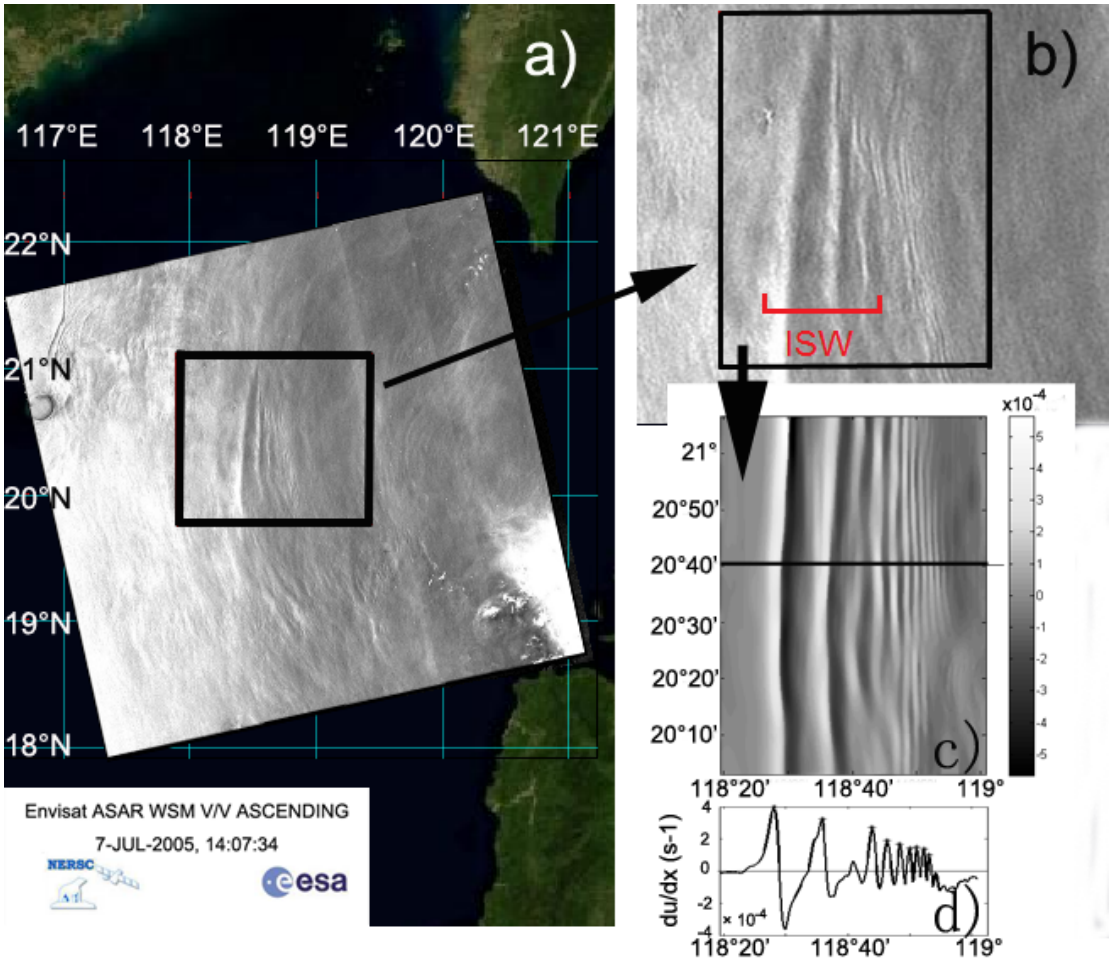

Figure 5.9: Panel a: ASAR image acquired at 1407 UTC on 7 July 2005 over the far-field. Panel b: Zoom on the area showing sea surface signatures of ISWs followed by a packet of short internal waves. Panel c: Two-dimensional map of the simulated surface current gradient $du/dx(s^{-1})$ in x-direction (horizontal direction). Panel d: Variation of the simulated gradient du/dx along the transect $20°40'N$ (marked by a black line in Panel c).

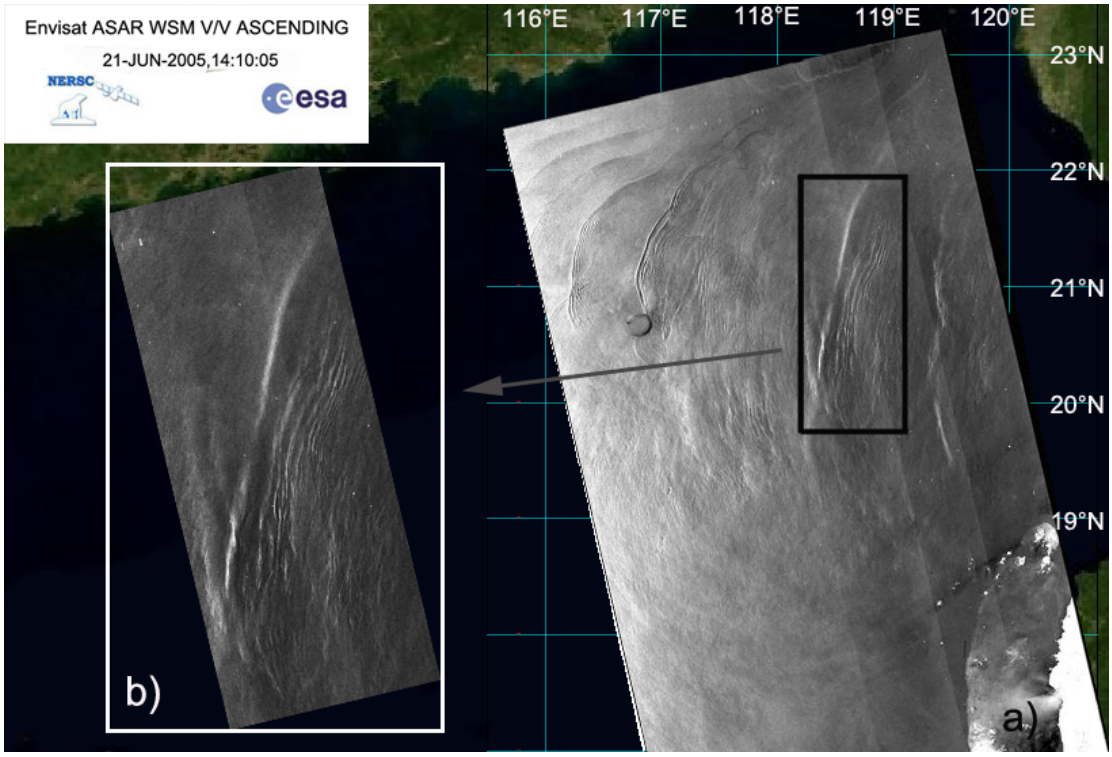

Figure 5.10: ASAR image acquired at 1410 UTC on 21 June 2005 over the far-field. The zoom on the wave pattern (Panel b) shows sea surface signatures of a single ISW followed by a packet of short internal waves.

ing physical mechanism is that the secondary short internal waves are nonlinearly coupled with the carrier second mode ISW, from which they absorb energy and grow in amplitude. Nonetheless, more robust evidence of such wave coupling has been lacking after Akylas & Grimshaw (1992). This work justifies the feasibility of studying such effects with synthetic aperture radar (SAR), which is a reliable tool for studying internal waves in the ocean, and it might be that this phenomenon is more common than previously thought but has not been properly appreciated in SAR images before.

The aim of this investigation was to find observational evidence for the presence of short internal waves trailing strong ISWs in the northern SCS which have been found in previous numerical simulations. These short internal waves ride on a second mode ISW. The wavelength and amplitude of the short internal waves turn out to be around 1.5 km and 20 m, respectively. The simulations carried out with the MITgcm as well as the solutions of the Taylor-Goldstein equation show that the generation of short internal waves trailing a first mode ISW requires the presence of a strong second mode ISW, which gives rise to a specific shear current profile $U(z)$.

Furthermore, the simulations show that the short internal waves riding on a second mode ISW and following a strong first mode ISW occur in two distinct areas, one close to the LS and the other further west. In the first area, they are generated by the disintegration of a baroclinic bore, which is generated by the interaction of the tidal current with the topography. In the second area they are generated by nonlinear interaction between ISWs of the first and the second modes. This interaction takes place when a faster first mode ISW overtakes the second mode ISW which was generated one tidal cycle earlier.

It should be noted that there also exists evidence from in situ measurements that short internal waves exist in the northern SCS. Klymak et al. (2006) observed short internal waves riding on a large amplitude first mode ISW of depression in the deep basin of the northern SCS. They speculated that the short internal waves are generated by shear instability or by the interaction of pre-existing short internal waves with the incoming ISW, which gives rise to wave amplification. However, due to the limitation of the temporal sampling of the measurements, and due to the intrinsic small scales of the short waves, it is not easy to capture the full picture of the short wave structure from in situ observations.

The simulations show that the short internal waves can produce strong convergence/divergence zones at the sea surface, giving rise to strong sea surface roughness modulation that renders the short internal waves visible on SAR images. However, one can extract from SAR images only information on the spatial configuration of the internal wave field, but no information on the wave amplitude. The ESA ASAR archive for SAR images was screened, in order to find sea surface signatures of ISWs trailed by packets of short internal waves in the northern SCS and several tens of them were found. The analysis revealed that, with only two exceptions, all packets of short internal wave trailing strong ISWs are encountered in two distinct longitude bands, one located close to the LS and the other further west, which is in accordance with the model calculations.

Six ASAR images showing the features under investigation were analyzed in detail. It was shown that the measured wavelengths of the short internal waves, the alignment of the wave packets, and the distance between the leading first mode ISW and the front of the short internal wave packet all lie well within the range of model predictions.

On two ASAR images, sea surface signatures of wave packets containing several ISWs followed

by a (weak) short internal wave packet close to the LS were found. It was conjectured that they are generated by enhanced barotropic currents in the LS. This was confirmed by simulations carried out with a 30% larger barotropic forcing.

It is hoped that the six ASAR images presented in this paper showing sea surface signatures of internal waves have provided sufficient evidence that short internal waves trailing strong ISWs do exist in the northern SCS as predicted by model calculations. As can be seen, strong tide-topography interaction, steep ridges, and double-ridge effects are indispensable for the appearance of such short waves in the northern SCS. However, it would be imprudent to conclude that this phenomenon is unique to this region. As was shown earlier, the western ridge alone, which is deep yet steep, could generate first and second mode signals with comparable magnitudes, although much weaker than the double-ridge case. Similar steep ridges in the ocean, not necessarily deep, can also generate multi-modal beams which subsequently disintegrate, and second mode internal waves and thus short waves are prone to emerge. It is expected that in the future also in situ data will be available to substantiate these theoretical findings.

Chapter 6

Simulation of A and B internal solitary waves observed in the northern South China Sea

[1]

Sections 4.4 and 4.5 discussed some factors that can affect the generation of internal waves from the LS, for example, the existence of the western ridge, the strength of the tidal forcing, etc. In this chapter, the influence of multiple tidal harmonics at LS on the resultant wave field will be looked into. As a matter of fact, it turns out that asymmetrical barotropic tides at LS, which are due to the superposition of diurnal and semi-diurnal tides, have great implications on the timing and magnitude of ISWs in the far field and produce the so-called A and B ISWs. A series of 2D experiments with realistic tidal forcing was configured with MITgcm and characteristics of A and B ISWs will be scrutinized.

6.1 Observational evidence of A and B waves and their correlation with the forcing in the Luzon Strait

The finding and notion of A and B ISWs originate from the ASIAEX experiment. Based on the mooring observations above the continental slope, Ramp et al. (2004) divided the observed packets into two types: A waves and B waves. ISWs belonging to A waves have larger amplitudes and arrive at the moorings regularly with a period of 24 hours, whereas B waves are relatively weaker and arrive about one hour later every day. It was found that the mixed barotropic tides featuring both diurnal and semidiurnal harmonics (see Figure 1.5), whose phase lag varies in time but all produce an asymmetric current, are responsible for the alternative appearances of such waves. In recent years, due to this east-west current asymmetry, there has been much debate about the alternate generation of A and B waves (Zhao & Alford 2006, Alford et al. 2010, Buijsman, Kanarska & McWilliams 2010, Buijsman, McWilliams & Jackson 2010, Ramp et al. 2010, Zhang et al. 2011), which appear both in the deep basin and on the continental slope and shelf. These papers have been trying to correlate A and B waves with either the eastward or westward current peaks in the LS, accompanied by the diverse conclusions on the generation processes and mechanisms.

Zhao & Alford (2006) analyzed the arrival times of ISWs at two moorings, and related A and B waves to the tidal forcing over the eastern ridge in the middle LS. The comparisons showed that every ISW packet can be associated with a westward current peak in the LS rather than an eastward one, and they suggested that the packets of ISWs are produced due to nonlinear steepening of internal tides rather than the developments of lee waves. By contrast, using the non-hydrostatic ROMS, Buijsman, Kanarska & McWilliams (2010) found that westward propagating ISWs follow strong eastward barotropic tidal currents in the LS. This is further corroborated by mooring measurements near the two ridges by Alford et al. (2010), who showed that

[1] This chapter is mostly based on the paper Vlasenko et al. (2012)

westward propagating A/B ISWs align with eastward strong/weak tidal peaks. However, at the same time they also addressed the potential difficulty in assessing the phase of the generated waves with the complicated current field above the ridges. By correlating observational data in the northern SCS and in the LS, Ramp et al. (2010) drew a different conclusion that much stronger eastward tides at LS correspond to the generation of more nonlinear A waves, whereas B waves are associated with the weaker westward tides at LS. This idea was later corroborated by the 3D numerical simulation by Zhang et al. (2011), who also proposed that both types of ISWs arise from the nonlinear steepening of semidiurnal internal tides from the LS instead of lee wave mechanism. Zhang et al. (2011) attributed the stronger A wave generation at the southern LS to the augmentation of semidiurnal A waves by the diurnal internal tidal beams, whereas stronger B waves in the north LS result from the resonant effect of the two ridges whose distance is approximately the wavelengh of semidiurnal internal tide.

This investigation was motivated by the fact that inconsistent conclusions on the generation and propagation of A and B waves in the northern SCS are reached. In attempting to explain this phenomenon, the 2D MITgcm model was used again as the numerical approach. Model-predicted wave fields are presented and compared to in situ measurements, and the conclusions are reinforced by a linear multi-harmonic tidal generation model.

6.2 Analysis of historical mooring data

The main goal of the analysis of historical mooring data is to find a correlation between the baroclinic tidal signal recorded at moorings in the northern SCS and the intensity of the barotropic tidal forcing in the LS. At first glance the correlation is evident: the stronger the current is, the larger the internal waves are. This tendency was reported in the majority of the papers devoted to ISWs in the northern SCS. However, the correlation is not so evident if one takes into account the spectral characteristics of the barotropic tidal forcing. In fact, 8 principal tidal harmonics contribute to the generation of internal waves: 4 diurnal, K_1, O_1, P_1, Q_1, and 4 semidiurnal, M_2, S_2, N_2, K_2. The LS is located between 19° and 22°N, which is not far from the latitude critical for the diurnal tides (about 30°N). It is known (Gerkema & Zimmerman 1995, Gerkema 1996) that strong rotation at high latitudes suppresses the generation of internal tides, so it is expected that the diurnal baroclinic tidal signal should be weak in the northern SCS. On the other hand, the location of the LS is far from the critical latitude for all the semidiurnal tidal harmonics (approximately 75°N), and thus the influence of the rotation is less important for the internal waves generated by these harmonics.

Some historical long-term mooring time series are compared in Figure 6.1 against the intensity of the tidal forcing in the LS in two different frequency bands: semidiurnal and diurnal. Figure 6.1a represents a time series (Yang et al. 2004) of the horizontal velocity recorded in April, 1999 at 30 m depth at mooring M ($21°2.8'N, 117°13.2'E$) (sampling interval was 30 s). The zonal barotropic water transport shown in Figures 6.1b-d was calculated at point $20°N, 122.5°E$ using the TPXO 7.1 model. The test point was deliberately shifted by 0.5° to the east of the LS to avoid any influence of the islands. Yang et al. (2004) reported that the soliton activity appears as cluster of spikes in the mooring data that is marked by the rectangle in Figure 6.1a. The soliton signal beyond the rectangle was not recorded.

The comparison of the observed wave velocities (Figure 6.1a) with the total (Figure 6.1b), semidiurnal (Figure 6.1c), and diurnal (Figure 6.1d) tidal forcing in the LS shows quite an interesting result. First of all, the time of the highest soliton activity observed on 15-18 April

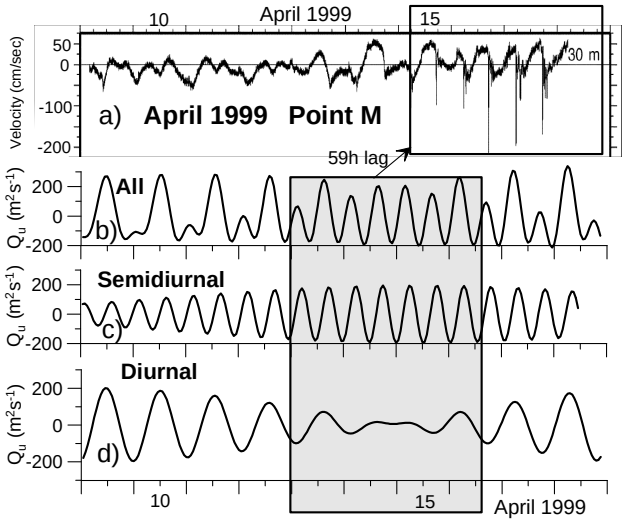

Figure 6.1: a) fragment of the zonal velocity observed at 30 m depth at mooring M ($21°2.8'N, 117°13.2'E$) in April, 1999 (Yang et al. 2004). TPXO 7.1 model predicted zonal barotropic water discharge at point $20°N, 122.5°E$ produced by all (b), semidiurnal (c), and diurnal (d) tidal harmonics. The shaded area in panels b,c, and d represents the tidal forcing corresponding to ISWs observed on 15-18 April (the rectangle in panel a).

does not coincide with the period when all the tidal harmonics in the LS produce the strongest signal (compare Figure 6.1a,b). Instead, the strongest waves were generated between 13 and 16 April when the diurnal barotropic tidal transport decreased to its minimal value (close to zero, in fact). In this analysis a time lag of 59 hours between the mooring records and the tidal signal at the LS, i.e., the travel time of ISWs from the LS to the mooring M estimated by Yang et al. (2004), is taken into account. The answer can be found in terms of a multi-harmonic approach of tidal generation considering water transport of diurnal and semidiurnal harmonics separately. The absence of solitary waves during 9-14 April is seen when the appropriate water transport of the diurnal harmonics was maximal. At the same time the period of strong ISW activity at mooring M is correlated with the maximum of semidiurnal forcing (Figure 6.1c).

These remarks also concern the ADCP mooring data collected in September, 1990 by Ebbesmeyer et al. (1991) at Point L ($21°27.88'N, 116°37.75'E$), as shown in Figure 6.2a; the passage of ISW packets is clearly seen here as clusters of spikes. Zonal tidal components of semidiurnal and diurnal harmonics are shown in Figures 6.2b and c, respectively. Two series of ISW packets are marked by the rectangles (Figure 6.2a). Similar rectangles are shown in panels b and c. A 3-day time lag (the travel time of internal waves from the LS to Point L) is taken into account. Figure 6.2 shows a strong correlation between ISW events observed at Point L and the maximum of the semidiurnal tidal water transport. The diurnal tidal forcing during these periods was weak or even close to zero.

Similar comparison analysis of the observational data was conducted for several other published long-term mooring time series (for instance, the data shown by Zhao & Alford (2006), Farmer et al. (2009), Li et al. (2009)). They were compared against the tidal currents produced in the LS by semidiurnal, diurnal, and all tidal harmonics. Strong correlation between ISW events recorded at the moorings and the maximal amplitude of the semidiurnal barotropic tidal currents

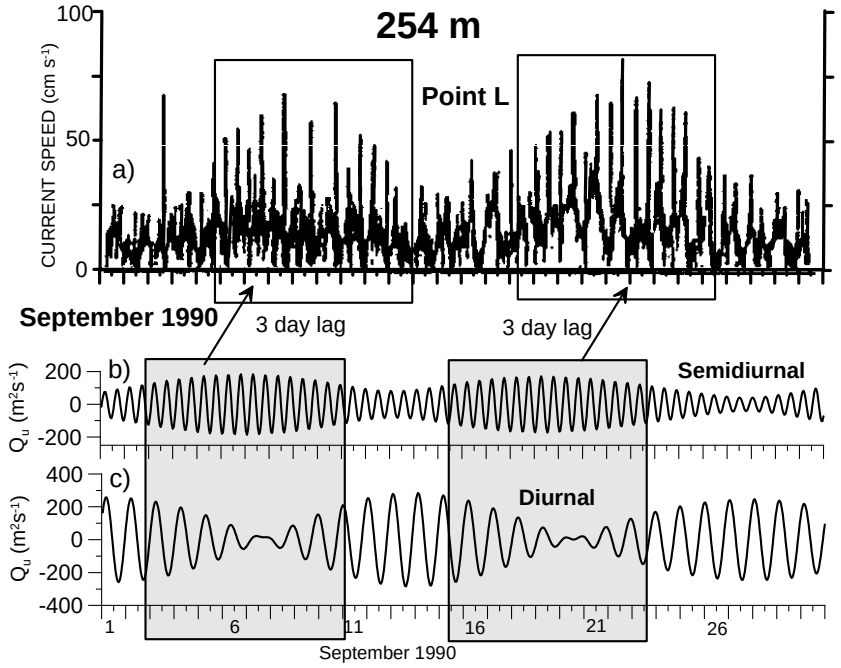

Figure 6.2: a) Current speed recorded at 254 m depth at Point L($21°27.88'N, 116°37.75'E$) in September 1990 (Ebbesmeyer et al. 1991). Panels b and c show the zonal barotropic water discharge for semidiurnal and diurnal tidal components at the LS at position $20°N, 122.5°E$.

in the LS (as shown in Figures 6.1 and 6.2) was established in the analysis. At the same time considerably weaker ISW activity was recorded when the diurnal tidal forcing in the LS was maximal.

6.3 Model reproduction of A and B internal solitary waves

The conclusion on the predominately semidiurnal nature of ISW generation in the northern SCS is supported by all the observational data sets considered here. Note, however, that the semidiurnal forcing alone cannot generate A and B waves. Hence, one might conjecture that the diurnal harmonics can be important in their production. In this section the modulation of the diurnal harmonics and the resultant characteristics of A and B waves are simulated with MITgcm.

An averaged 2D topography (Figure 4.8) was used for the model initialization. The model was driven by a superposition of eight principal tidal harmonics, which were implemented into the model as an external force on the right hand side of the momentum equations. The reproduced barotropic tidal flow closely coincides with the TPXO 7.1 model prediction (Figure 6.3). Internal waves are generated over the bottom topography and propagate eastward and westward. Telescoping grids were implemented in the east and west open boundaries to avoid wave reflection. Water depth beyond the two ridges was set to 3000 m. Background stratification is shown in Figure 1.6 (summer).

Cartesian coordinate was used in the model. The horizontal resolution was set to 250 m. In the vertical direction, 90 layers were used, with a resolution of 10 m in the upper 500 m layer

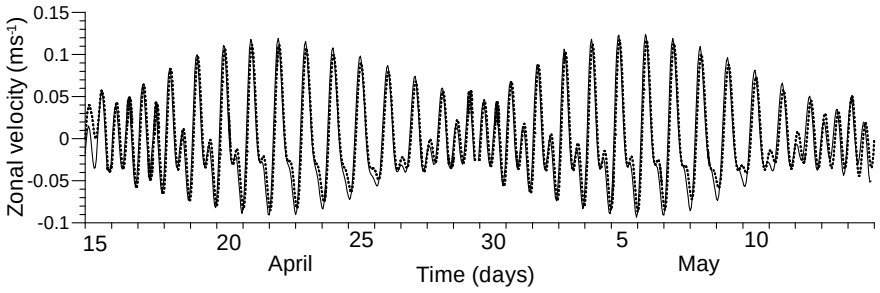

Figure 6.3: Zonal barotropic tidal velocity in the deep part of the model domain predicted by the TPXO 7.1 (solid line) and reproduced by the MITgcm (dashed line).

(below the main thermocline), followed by 20 intermediate layers with 50 m resolution, and another 20 deep layers with a resolution of 150 m. Time step was set to 12.5 s.

Figure 6.4 shows the one-month model predictions calculated from 17 April to 14 May, 2007. Left column of the figure shows the horizontal velocity at the free surface taken at point MP1 ($20.919°N, 117.895°E$; see Alford et al. (2010)), which is located about 430 km away west of the eastern ridge. Similar time series but for the point 430 km east of the eastern ridge is shown in the right column. The whole one-month time series is split into daily fragments. The corresponding one-month TPXO 7.1 barotropic tidal predictions of the zonal water discharge for all tidal harmonics, and separately for the semidiurnal and diurnal harmonics at $20°N, 122.5°E$ above the eastern ridge are shown in the middle column of the figure.

The shaded areas in Figure 6.4 represents two periods of strong semidiurnal tidal activity when large amplitude ISWs are mostly generated. However, during the unshaded 'white' periods, when the diurnal currents over the ridges are much stronger than the semidiurnal counterpart, much weaker internal waves are generated. Low ISW activity on 25-30 April and 10-14 May (only one wave packet is generated a day) is consistent with the aforementioned conclusion about the predominantly semidiurnal nature of the generation mechanism.

Before analysing the characteristics of A and B ISWs, the terminology of Ramp et al. (2004) is used but is not totally alike: no matter if the ISW arrives at the same time or 1 hour later every day, the wave packet will be marked A (a) if it contains two or more waves, and B (b) if it contains a single wave. Two wave packets pass by the control points every day, and are distinguished by one capital and one lower case letter. They represent two different families of ISWs, as are connected by the dashed lines in Figure 6.4. To provide a unique marking of each particular packet, the subscripts that denote the number of the day were introduced for A (a) and B (b) waves.

Figure 6.4 shows that the model reproduces both types of waves, as were classified by Ramp et al. (2004). More specifically, during the first 6 days (17-22 April), the model output shows two groups of ISW packet. The first packet arrives 1 hour later each day (waves $a_1 - a_4, b_5 - b_6$), and the second packet (waves $A_1 - A_6$) arrives almost at the same time each day. A waves are greater in amplitude than a waves; they are recorded regularly as groups of rank-ordered ISWs that arrive at the same time each day.

To the east of the LS, the waves marked by the lower case letters arrive at the control point 1.3-1.4 hours later each day (17-22 April), not 1 hour later as it was for the western control point. So, the B waves delay discussed by Ramp et al. (2004) is captured by the model, but this effect of later arrival should be attributed to the wave family, rather than to the wave type (see

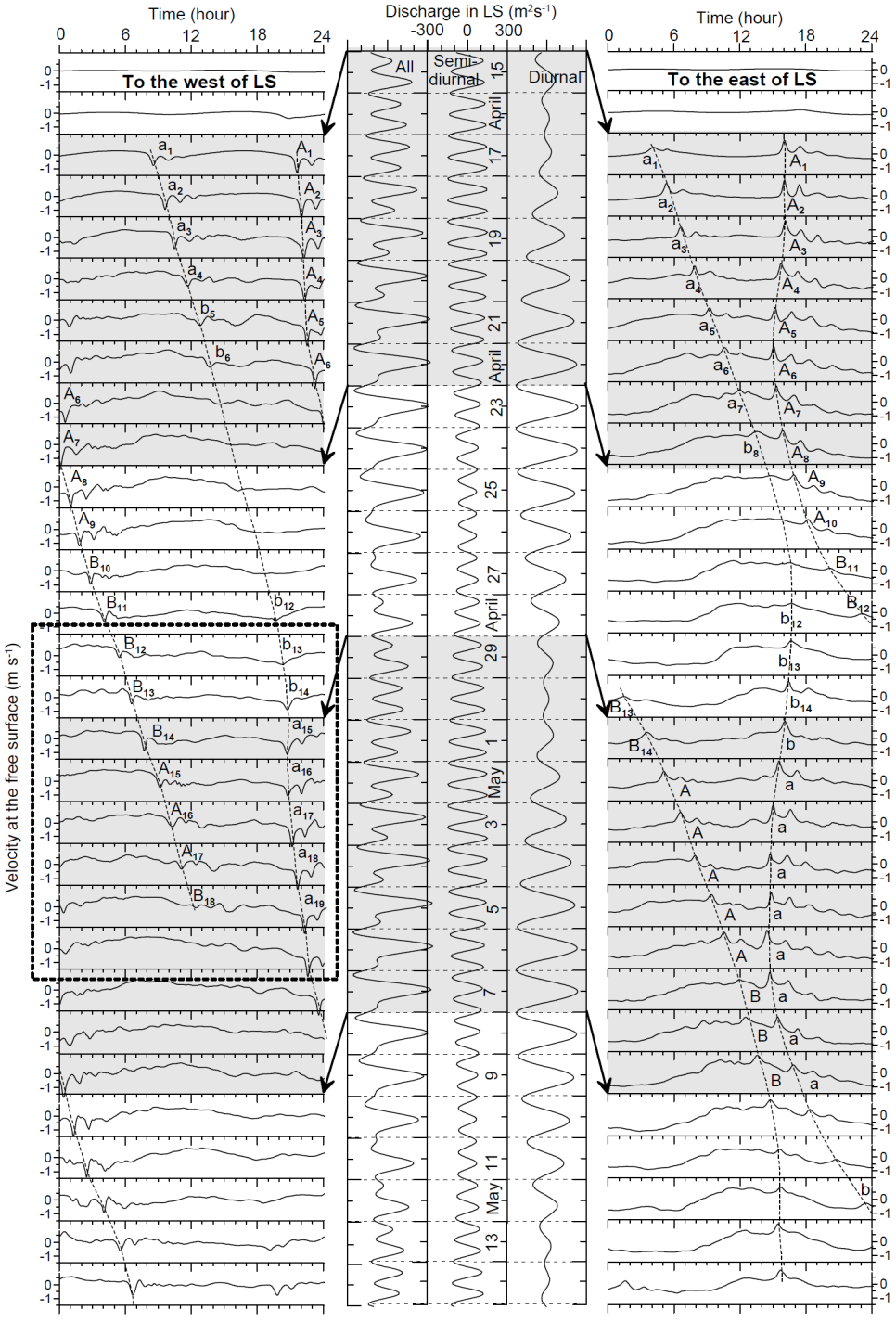

Figure 6.4: Time series of the horizontal velocity at the free surface 430 km to the west (left column) and 430 km to the east (right column) from the LS for the time period 17 Apr-14 May,2007. Waves A(a) and B(b) are marked by the appropriate letters. Three graphs in the middle represent east-west discharge predicted by TPXO 7.1 for all semidiurnal and diurnal tidal harmonics (marked accordingly). Arrows show the time lag between tidal forcing in the LS and the signal in the control points.

Figure 6.4).

Note also a quantitative difference in the delay time to the west and to the east of the ridge. The waves of the family marked by capital letters in the left column are recorded roughly at the very same time each day (waves $A_1 - A_5$), but at the eastern control point the arrival time of A waves varies. It is the same on 17-19 April (waves $A_1 - A_3$), but on 20-22 April A waves are recorded earlier each day (find waves $A_4 - A_6$). An interesting consequence of such an early arrival of A waves is that the time span between the recording time of the waves of different families gradually decreases to its minimal values of 2.5 hours (find waves b_8 and A_8 on 25 April). Partly this convergence of two wave families is explained by the later arrival of a-b waves. The situation changes to the opposite on 25 April when A waves start to arrive later each day (waves $A_9, A_{10}, B_{11}, B_{12}$).

An interesting finding that can be drawn from Figure 6.4 is the reconstruction of the wave type from A (or a) waves into B (or b) waves and vice versa. Figure 6.4 shows that the transition of A (a) waves into B (b) waves normally takes place as the amplitude of the semidiurnal tidal forcing is decreasing. The transition from B (b) to A (a) usually occurs when the semidiurnal forcing increases. It is interesting that the time series presented by Zhang et al. (2011) in their Figures 11 and 12 can be treated as 'A-B-A-B' wave transition as well, but this process was not properly acknowledged.

The model output obtained for April-May, 2007 was compared against the observational data reported by Alford et al. (2010). The left column of Figure 6.5 represents a one-week fragment of Figure 6.4 (shown in dotted rectangle), and the right column shows the zonal velocity recorded at mooring MP1 in April-May, 2007. The original numbering of ISW packet used in the aforementioned paper and the titles of the model-predicted wave packets are retained in this figure. It is seen from the comparison analysis that the arriving time of the model-predicted and observed ISW packets at the control point MP1 reveals similar characteristics. ISWs that belong to the lower-case-letter family are recorded nearly at the same time in both cases during the time period 30 April-4 May. Starting from 5 May these waves arrive half an hour later each day, and this tendency appears both in theoretical and observational data sets. The capital letter wave family reveals a one-hour delay in wave arrival each day, and this delay is typical of both theoretical and experimental data sets.

Another example of model validation is shown in Figure 6.6. The model-predicted and experimentally recorded mean subsurface zonal velocity at control point MP1 is presented here as a single time series (without splitting it into one-day pieces) in order to show the timing of the wave events and to compare the wave type in both cases. The wave marking here is the same as in Figure 6.5. As it is seen from Figure 6.6, the timing of the wave events in panels a and b is very good. The dashed lines show that theoretically predicted arrival time is consistent with the experimentally recorded time. The type of the generated waves is also captured by the model quite accurately. The intensity of the wave events gradually increased from the left side to the middle of Figure 6.6, and as a result, the single-wave B waves shown in panels a and b on 29 April-1 May turn to A waves on 2-5 May, and this transition takes place in both theoretical and experimental time series.

Thus, the comparative analysis shows that the model output is consistent with the observational data. Taking into account that the model-predicted wave fields were obtained using a 2D version of MITgcm, but the real three-dimensionality of the wave process can introduce some substan-

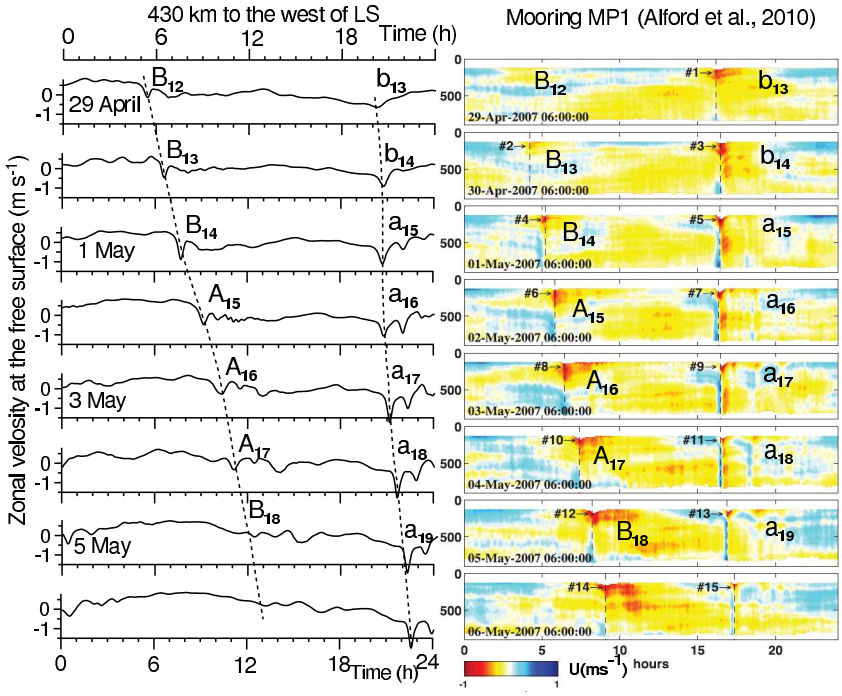

Figure 6.5: Zonal velocity predicted by the model at the free surface (left column), and measured by Alford et al. (2010) at mooring MP1 (right column). Original numbering of the aforementioned paper is shown by integer numbers. The wave titles corresponding to the model-predicted wave packets shown in Figure 6.4 are depicted by the capital and lower case letters with subscripts.

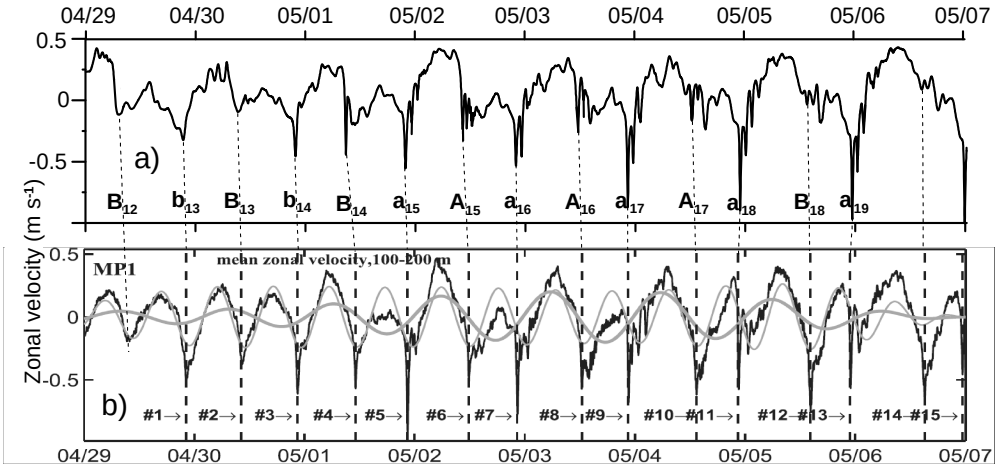

Figure 6.6: Mean sub-surface zonal velocity at mooring MP1 predicted by the MITgcm (panel a) and reported by Alford et al. (2010) (panel b). Wave numbering of in situ measured and model-predicted internal wave packets is the same as in Figure 6.5.

tial spatial variations along the wave fronts (e.g., Zhang et al. (2011)), the consistency of the model results with the observations can be qualified as very good.

Another model run was conducted for July, 2010 when the generation conditions were different from those in April-May, 2007. The basic difference between these two cases was that the maximum of the semidiurnal and diurnal forcing in July, 2010 nearly coincided, whereas in April-May 2007 they were out of phase. This difference leads to quite a drastic change in the performance of A and B waves, as is shown in Figure 6.7. First of all, in terms of A and B waves classification as was suggested by Ramp et al. (2004), it is not clear what type of waves is presented in the left column (to the west of the LS). All waves (both A (a) and B (b)) arrive at the control point with a 0.7-0.75 hour time lag each day, which is mostly consistent with the semidiurnal nature of their generation. Note that on 3-6 July the lower-case wave packets contain only one ISW, so they can be classified as b waves, but after that period (7-17 July) the wave packets contain two or more ISWs and can be identified as a waves. Similar effect of wave transition happens to the A (B) wave family: A waves transform to B waves (5-6 July), or B waves transform to A waves (14-15 July).

So, the considered examples reveal that the classification of A and B waves suggested by Ramp et al. (2004) does not cover all scenarios. Moreover, the behavior of waves to the east of the ridges (right column in Figure 6.7) cannot be explained by this classification. One solitary wave packet B (b) arrives nearly at the same time each day (12-23, July) and gradually transforms into A waves which arrive 1 hour later each day (24-30 July).

6.4 Theoretical solution of A and B wave generation

As was reviewed in section 1.2.3, there has been a wide argument about the generation mechanism of internal waves in the northern SCS. Both 'evolutionary' internal tide and 'release' lee wave regimes are considered and discussed. According to section 4.3, the tidal excursion ku_0/ω, which characterizes the generation regime, is in the order of unity around the islands but turns out to be magnitudes lower in the majority of the strait, which implies it is overall favorable for the generation of internal tides.

The scenario of the far-field appearance of ISWs is confirmed by simple quantitative estimations. The measure of nonlinearity of the generation mechanism in the LS can be estimated using the following parameter (Gerkema & Zimmerman 1995):

$$\varepsilon_1 = \frac{tidal\ excursion}{topographic\ length\ scale} \times \frac{topographic\ height}{fluid\ depth}$$

The second ratio in this formula is close to unity, whereas the first one estimated for typical generation conditions gives the value of about 0.05 or less (depending on the day of the neap-spring cycle), which suggests a weakly nonlinear regime of wave generation. Under such conditions the baroclinic tidal waves permanently radiate from the LS as freely propagating long internal waves. Far from the generation site they steepen and disintegrate into packets of ISWs (Gerkema & Zimmerman 1995). In the subsequent analyses this scenario will be taken as a hypothesis for the explanation of the characteristics of A and B waves.

6.4.1 Multi-harmonic solution

The problem of the generation of internal waves by a periodic barotropic tidal flow was discussed in section 4.4. Beyond the generation area where the water depth H is constant, the wave field is a superposition of a barotropic tidal flow and a series of baroclinic modes:

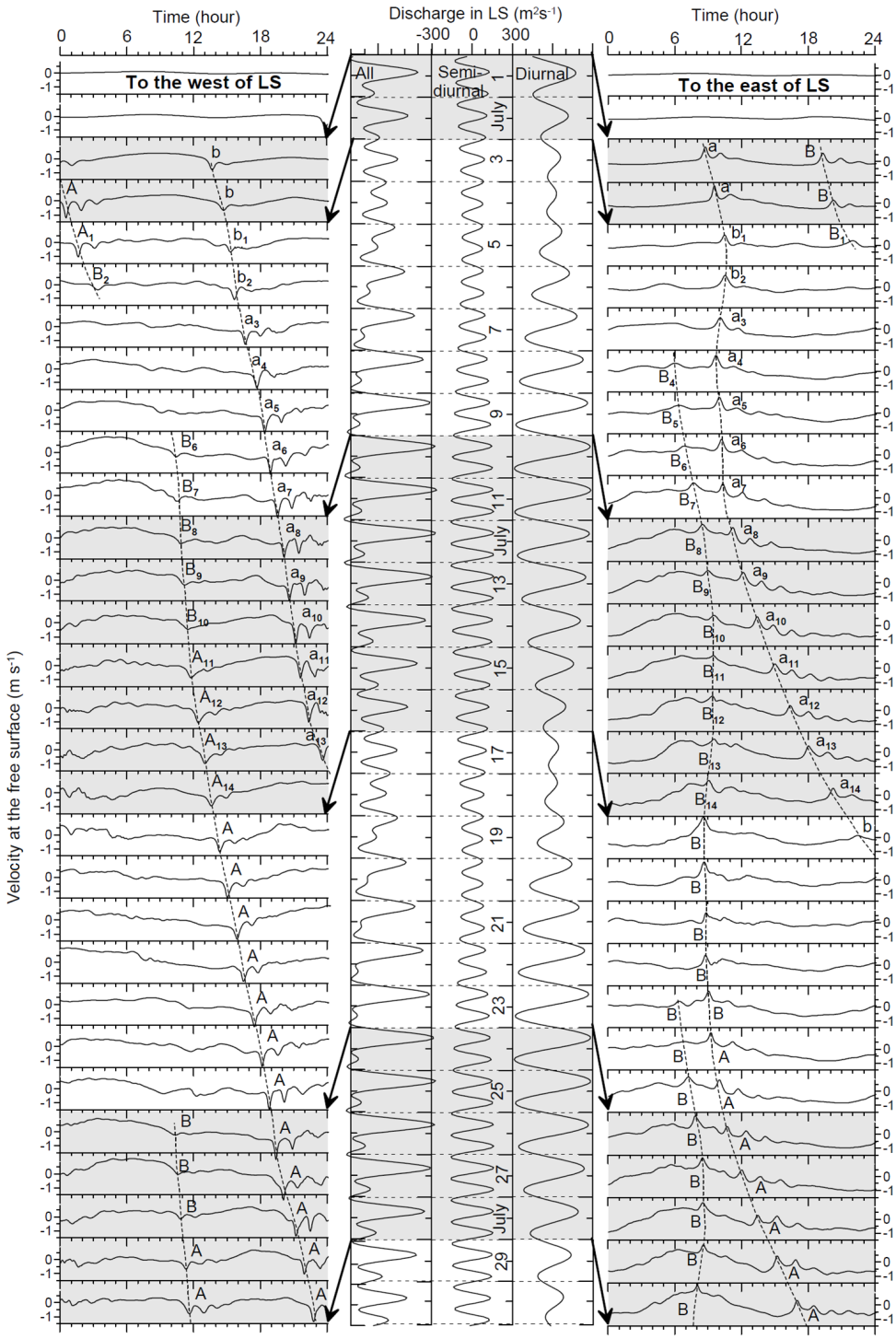

Figure 6.7: The same as in Figure 6.4 but for July, 2010.

$$\Psi(x,z,t) = \Psi_m(1+z/H)exp(-i\sigma t) + \sum_{j=1}^{\infty} a_j g_j(z) exp[i(k_j x - \sigma t + \varphi_j)] \tag{6.1}$$

where Ψ_m is the amplitude of the barotropic tidal flow, and the other variables are explained in equation (4.2).

The above linear solution is valid for one particular tidal harmonic, but the baroclinic tide in the SCS is generated by several tidal constituents. In the framework of linear theory the wave field produced by all the principal harmonics is just a linear superposition of several elementary solutions (6.1). This property only takes place only if the condition $N^2(z) >> \sigma^2$ is valid for the whole water column, which is the case of the northern SCS (see the stratification in Figure 1.6). If so, one can take a superposition of solutions (6.1) obtained separately for every tidal harmonic and build a desirable combination valid for the conditions of the northern SCS.

Notice that series (6.1) contains an indefinite number of baroclinic modes, but not all of them equally contribute to the resulting wave field. In the first instance only the first mode internal waves which are the most energetic, are considered.

The next step is the calculation of the wave parameter, which are the wave amplitude a_1 and phase φ_1. In doing so the problem of wave generation was solved separately for the semidiurnal and diurnal constituents. The details of the mathematical procedure are described by Vlasenko et al. (2005). The value of the input parameter Ψ_m for the period of April-May, 2007 and July, 2010 was taken from the TPXO 7.1 model predictions. Due to the neap-spring tidal variability this value varies with time, as were shown in Figures 6.4 and 6.7. This is the reason why the amplitude a_1 of the dominant first mode internal wave changes in time with neap-spring periodicity. The dependence of $a_1(t)$ on time is shown in the upper panels of Figures 6.8 and 6.9, both for the semidiurnal (solid line) and diurnal (dashed line) constituents.

A two-fold variation of the amplitudes of the semidiurnal wave (vertical isopycnal displacements at the depth where function $g_1(z)$ has maximum), i.e., from 24 m to 54 m over one neap-spring cycle in April, 2007, and from 27 m to 57 m in July, 2010 was found from the linear theory. The appropriate amplitudes of the diurnal harmonics in April, 2007 ranged from 2 m to 32 m (Figure 6.8a), and from 5 m to 39 m in July, 2010 (Figure 6.9a). An obvious difference between these two cases is that the maximum and minimum of the semidiurnal and diurnal baroclinic wave activities in July, 2010 nearly coincide in time (the dashed and the solid lines in Figure 6.9a are in phase), whereas in April-May, 2007 they are shifted in time for a 5-day span (the dashed and solid lines in Figure 6.8a are out of phase). This shift has a drastic implication on the structure of the generated waves.

6.4.2 Evolutionary mechanism

Beyond the source of generation the internal wave field can be presented as a superposition of diurnal and semidiurnal progressive waves:

$$\zeta(x,z,t) = a_1^s g_1(z) exp(k_1^s x - \sigma^s t + \varphi_1^s) + a_1^d g_1(z) exp(k_1^d x - \sigma^d t + \varphi_1^d) \tag{6.2}$$

where a_1^s and a_1^d, k_1^s and k_1^d, φ_1^s and φ_1^d are the wave amplitudes, wavenumbers, and the phases of the first mode internal waves. The superscripts s and d denote semidiurnal and diurnal harmonics, respectively. Note that with the assumption $N^2(z) >> \sigma^2$, which is valid for the whole

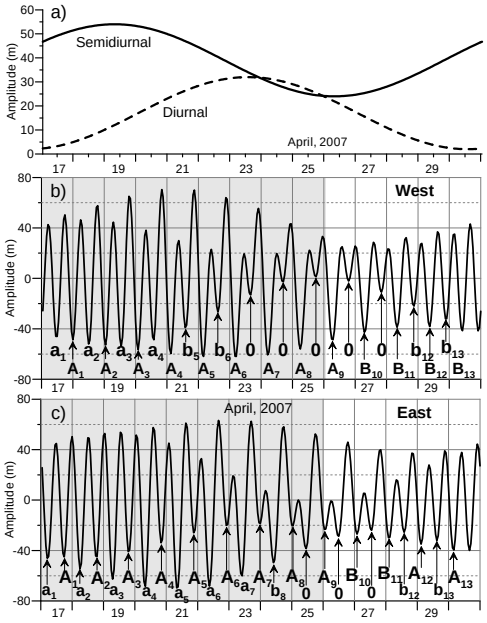

Figure 6.8: a) Amplitude of the first baroclinic mode (a_1) calculated for April, 2007. The solid lines correspond to the semidiurnal constituents, the dashed line to the diurnal. Superposition of semidiurnal and diurnal internal waves at two control points: to the west (panel b) and to the east (panel c) of the eastern ridge with their amplitudes predicted by the analytical solution (panel a).

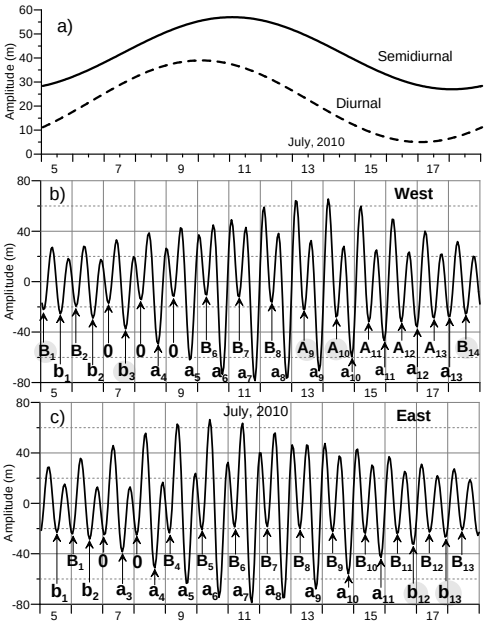

Figure 6.9: The same as in Figure 6.8 but for July, 2010.

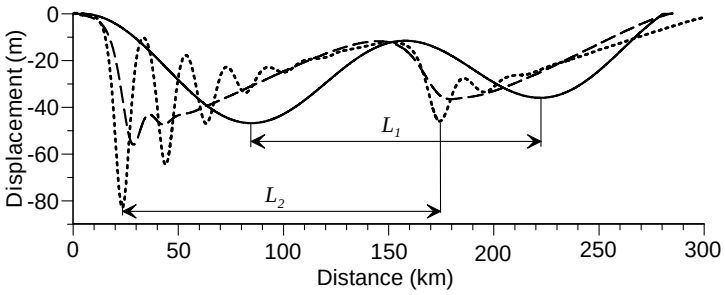

Figure 6.10: Evolution of an initial two-wave profile (solid line) calculated using the KdV equation for the parameters typical to the SCS. Dashed and dotted lines represent the wave profiles after 25 and 50 h of wave propagation, respectively.

water column in the northern SCS, the vertical structure functions $g_1(z)$ for the semidiurnal and diurnal harmonics coincide, which is why only one symbol $g_1(z)$ was used for both.

Superposition of waves (as expressed by equation 6.2) with the amplitudes $a_1^s(t)$ and $a_1^d(t)$ taken from Figures 6.8a and 6.9a produces the wave displacements that are presented in Figures 6.8b-c and 6.9b-c. These time series show an alternation of large and small peaks which holds for the whole period in July, 2010 and for the most part of the neap-spring cycle in April, 2007. Similar intermittency of the wave amplitude is expected in space as well. If so, the progressive wave with an irregular profile can steepen and disintegrate, as is shown in Figure 6.10. In this experiment the wave profiles were calculated using the KdV equation with the parameters of nonlinearity and dispersion typical for the northern SCS.

The number and intensity of ISWs emerging from an initial perturbation depend on several parameters. Some observations (Ramp et al. 2010) suggest that ISWs are generated when the tidal velocity in the LS exceeds some critical level below which no ISW activity can be recorded. Moreover, some observations (Yang et al. 2004) showed that the transition from no waves to large amplitude ISW regime is quite sharp, whereas some revealed quite a monotonous transition from high to low ISW activities (Ebbesmeyer et al. 1991), which correlates with the gradual changes in the semidiurnal tidal forcing shown in Figure 6.2b.

As it follows from the inverse scattering problem, the number of the new-born ISWs in a two-layer system can be predicted by the following formula (Whitham 1974, Gerkema & Zimmerman 1995):

$$N < \frac{1}{2}\left[\sqrt{1+\frac{6a\varepsilon(1-2\alpha)}{\gamma^2\delta}}+1\right] \tag{6.3}$$

where a is the nondimensionalised initial wave amplitude (by the water depth H), $\varepsilon = \frac{U_0\varepsilon_b}{\sigma L_b}$ is a parameter of nonlinearity (U_0 and σ are the strength and frequency of the barotropic forcing,

respectively; L_b is the topographic length scale; ε_b is a nondimensionalised topographic height scale (by the water depth H) and is assumed $\varepsilon_b << 1$), $\alpha = \frac{H_1}{H}$ is the nondimensional depth of the interface (H_1 is the upper layer depth), $\delta = (\frac{\sigma H}{c})^2$ is the dispersion parameter (c is the long wave phase speed), and $\gamma = \sqrt{\alpha(1-\alpha)}$.

For the conditions of the northern SCS, the position of the interface should be taken between 500 and 700 m, in order to provide the best fit of all the basic wave parameters to observations. For 700 m depth equation (6.3) predicts a 40 m threshold of the wave amplitude when two or more solitary waves can emerge from a propagating long wave. Hereafter 40 m amplitude is used as a boundary to distinguish A waves from B waves. Note that this value is consistent with Figure 6.10, in which the wave disintegration is shown as a direct evolutionary process.

Applying the amplitude threshold to the wave profiles shown in Figures 6.8b-c and 6.9b-c, every depression was marked as A wave if its amplitude is greater than 40 m, or B waves otherwise. Similar to Figures 6.4 and 6.7 one capital and one lower case letter are used for marking the wave troughs within every 24 hours time span. Note that the displacements with amplitudes less than 10 m are marked as 0, implying that such waves are too weak to be disintegrated near the generation site (less than 3 wavelengths), and require longer distance for ISW formation (longer length of nonlinearity). The subscript of every particular wave trough in Figures 6.8 and 6.9 is similar to those shown in Figures 6.4 and 6.7.

The perfect correlation takes place between the type of the ISW events to the west of the LS shown in the left column in Figure 6.4 and the type of the waves predicted by the linear theory in Figure 6.8b. The name of every single wave event coincides in both figures. Note that the correlation holds for the whole neap-spring cycle. The perfect coincidence between wave events also takes place to the west of the LS (right column in Figure 6.4 and Figure 6.8c). Thus the 'evolutionary' mechanism proposed here based on the steepening and disintegration of the propagating internal tidal waves is confirmed by the results of numerical modelling with a good accuracy.

Comparison of Figures 6.7 and 6.9 shows that the vast majority of the wave events coincide: i.e., 82% at the western observational point, and 93% at the eastern one. The restricted number of cases shown by the shaded circular spots in Figure 6.9 has different type of waves than that in Figure 6.7. Such a discrepancy could be a consequence of a number of factors such as inaccurate calculation of the amplitude threshold, idealized topography, etc. However, the 'evolutionary' method looks quite adequate and robust to give a reliable prediction of A and B waves.

6.4.3 Arrival time

The model output suggests that the arrival time is not a unique characteristic of any particular type of ISW. It follows from Figures 6.4 and 6.7 that there is no strict relationship between the wave arrivals, their types, and any particular phase of tidal forcing. For instance, the small letter waves reveal mostly doubled M_2 periodicity on 17-22 April, 2007. They appear at the western control point roughly one hour later every day from a to b waves (see Figure 6.4). The capital letter waves at the very same period of time are recorded with nearly diurnal periodicity (they arrive every 24.2 hours) and exhibit quite persistent A wave nature (i.e., two or more waves in the packet). However, after a short transition period on 23-24 April, the arriving periodicity increases to $\sim$25.1 hours and holds for quite a long period (till 5 May). During this time span the wave type changes three times, A$\rightarrow$B$\rightarrow$A$\rightarrow$B. In the end of this period the signal became so weak that it was not possible to identify any type of wave at all. This wave family became

visible again a week later (on 13 May) when the semidiurnal constituent of the tidal forcing increased.

The situation with the arrival time at the eastern control point (right column in Figure 6.4) is mostly the same as discussed above but with some differences. One can identify similar doubled M_2 periodicity ($\sim$25.3 hours) for the lower case family of waves on 17-24 April, and for the capital letter waves on 1-9 May. The change of wave type also takes place here. As far as the other two wave branches are concerned, A waves on 17-22 April and the lower case family waves on 29 April-5 May reveal $\sim$23.4 hours periodicity, which is even shorter than any doubled semidiurnal harmonics.

This drastic increase of the arrival time of A waves from 23.4 hours on 22 April to 26 hours on 28 April correlates with a two-fold weakening of the semidiurnal tidal forcing in the LS on 20-26 April (two days' time lag has been taken into account). Similarly, the semidiurnal wave amplitude in Figure 6.8 also decreases two times during this period, which can have an effect on the propagation speed due to the nonlinear wave dispersion.

The weakly nonlinear theory predicts 3.32 m/s of the phase speed for a 100 m amplitude ISW that propagates in a basin of 3000 m depth with the summer stratification in the northern SCS. The linear phase speed is equal to 3.16 m/s. Simple calculations show a 1.8 hours time lag between the arrival of the linear and nonlinear internal waves at the control point MP1 that is located at the distance of 430 km from the LS.

The effect of nonlinear dispersion is clearly seen in Figure 6.10, which illustrates a 50-hour evolution of two wave troughs. Initially the distance L_1 between the large and small waves was equal to 136 km. However, after 50 hours' evolution it increases to L_2 =152 km. Simple calculations show that it takes 1.4 hours more for the second wave to propagate the same distance to the control point.

The wave amplitude is not the only parameter that controls the arrival times. It is also important how far from the LS that the process of nonlinear disintegration takes place. The ISWs generated closer to the LS propagate longer distance with the nonlinear phase speed and arrive at the control point earlier.

6.5 Summary of characteristics of A and B internal solitary waves

Basic conclusions of this chapter can be formulated as following:

1. Analysis of the historical mooring data (Ebbesmeyer et al. 1991, Yang et al. 2004, Zhao & Alford 2006, Farmer et al. 2009, Li et al. 2009) shows a very strong correlation between the ISWs observed in the northern SCS and the intensity of the semidiurnal tidal harmonics in the LS. Much stronger diurnal constituents do not reveal any substantial influence on the appearance of ISWs. This conclusion on the predominantly semidiurnal nature of baroclinic tides in the northern SCS is supported by nearly all the published observational data sets and can be explained in terms of the rotational dispersion: production of ISWs in high-latitude seas (the LS is located between 19° and 22°N, which is close to the critical latitudes for the diurnal harmonics) is suppressed by the rotation (Gerkema 1996, Helfrich & Grimshaw 2008).

2. The role of the diurnal tidal harmonics lies in the modulation of the generated internal wave fields in such a way that a diurnal periodicity is introduced into the ISW signal known as A and B waves. The classification by Ramp et al. (2004) who coined the large amplitude rank-ordered

ISW packets as A waves and single weak ISWs as B waves, was applied in this study. It was found that the appearance of A or B waves is not directly linked to strong or weak tidal current peaks in the LS.

3. The MITgcm that was forced by a superposition of all the principal tidal harmonics reproduces both types of waves. The numerical experiments conducted for April-May, 2007 and July, 2010 show that the number of ISWs in A and B wave packet varies with neap-spring periodicity. Most clearly this periodicity is seen in a gradual transition of A waves into B waves, and B waves into A waves. The arrival time of A and B waves at any fixed observational point is also not a unique characteristic of any particular type of wave. It varies both for A and B wave packets depending on the forcing conditions in the LS.

4. The effect of A-B-A-B wave transition is treated here in terms of a multi-harmonic evolutionary mechanism. Analysis of the generation conditions at LS supports the idea that tidally generated internal waves freely radiate from the ridge. The radiated waves are a superposition of semidiurnal and diurnal internal tidal harmonics. The amplitudes of the most energetic first-mode internal waves were calculated using the linear theory of tidal energy conversion. Being superimposed, these two progressive waves (semidiurnal and diurnal) produce an intermittent baroclinic signal with large and small wave troughs that alternate in space. In the course of nonlinear evolution these large and small wave troughs steepen and ultimately disintegrate into A and B wave packets, respectively. Direct comparison of the multi-harmonic wave evolution with the results of the MITgcm modelling revealed a perfect correlation between the types of waves predicted by both methods.

Chapter 7

Simulating shoaling of a large amplitude second mode internal solitary wave

[1]

Chapters 4-6 are focused on the wave generation and wave structures at LS and in the deep basin. After ISWs propagate out of the generation region, they are often observed to propagate towards either the open ocean or into shallower waters, such as continental slopes, where the environment (depth, stratification, dissipation, stability, etc.) may differ significantly from that in deep water. This chapter (Chapter 7) and the next chapter (Chapter 8) will shift the focus on the wave evolution above the shoaling topography in the slope-shelf area of the northern SCS. This chapter tentatively studies the shoaling process of a second mode ISW, whereas the next chapter concerns the shoaling of a first mode ISW, with an emphasis on the rotational effects.

7.1 A review of internal wave shoaling and up-to-date study in the northern South China Sea

ISW shoaling processes have been studied in a number of papers (Helfrich et al. 1984, Kao et al. 1985, Helfrich & Melville 1986, Helfrich 1992, Michallet & Ivey 1999, Vlasenko & Hutter 2002, Vlasenko & Stashchuk 2007, Scotti et al. 2008). A basic conclusion that can be reached from the above studies is that the fate of an incident ISW is mainly determined by the water depth, stratification and wave amplitude, and the polarity of a wave may change during the adjustment process. On the other hand, when large amplitude waves impinge slope topography with steep inclination, wave breaking may take place, and such a process is essentially a kinematic instability rather than a shear one (Helfrich et al. 1984, Helfrich & Melville 1986, Vlasenko & Hutter 2002). Using a generalized KdV equation with continuously stratified water, Helfrich & Melville (1986) examined the behavior of an incident wave for a wide range of topography, stratification, and wave amplitude, and agreement between theory and experiment was reached. They found that weak shearing and strong breaking (overturning) instabilities strongly depend on the incident wave amplitude and stratification, and a kinematic instability mechanism on the wave breaking was proposed. This result was further corroborated by Vlasenko & Hutter (2002) who theoretically studied the transformation of large amplitude ISWs over a shelf-slope topography based on the full system of Reynolds equations, which can be accurately employed to investigate large waves beyond the limit of the classic weakly nonlinear theories. A breaking criterion of the ISW over the slope, which incorporated environmental factors like local water depth, stratification, incoming wave amplitude, and slope inclination, was derived by Vlasenko & Hutter (2002) as well. They showed that large waves and steep topography tend to result in steepening and overturning of a rear wave face, while in the opposite case the wave just evolves onto the shelf as a dispersive wave packet without any breaking.

[1] This chapter is mostly based on the paper Guo & Chen (2012)

Helfrich & Melville (1986) illustrated with laboratory experiments the mechanism by which the breaking of a first mode ISW is able to excite an apparent second mode ISW which can propagate onto the shelf before being damped. The semi-analytical method developed by Vlasenko et al. (2005) was employed to investigate the scattering of linear internal tides in slope-shelf regions. It was found that the incident wave, with the manifestation of resonance characteristics in wave diffraction, tends to radiate energy into neighboring baroclinic modes. The steeper the topography is, the more efficient such energy transfer will be. Taking into account the nonlinear nature of solitary waves, one can speculate that such splitting process of the incident wave must be even more pronounced when large amplitude ISWs are considered, an idea which is fundamental in the present work.

Compared with first mode ISWs, second mode ISWs are less common and have only been occasionally observed in the oceans (Konyaev et al. 1995, Duda et al. 2004, Moum et al. 2008, Yang et al. 2009, Shroyer et al. 2010, Yang et al. 2010). Theoretically, second mode ISWs possess a three-layer structure with two nodes for the horizontal current velocity and a two-layer structure with one node for the vertical current velocity (for more detail, see Vlasenko & Hutter (2001), Vlasenko et al. (2005), Yang et al. (2010)). Previous studies of second mode ISWs were mainly based on weakly nonlinear theories (Benjamin 1967, Davis & Acrivos 1967, Vlasenko et al. 2005), and their shapes have also been reproduced in laboratory experiments (Davis & Acrivos 1967, Helfrich & Melville 1986, Vlasenko & Hutter 2001). Pioneering investigations on this type of wave, including theoretical investigations, laboratory experiments, numerical analyses, and field observations, were summarized by Yang et al. (2010), and the readers are referred to the literature therein.

As for the case in the northern SCS (Figure 7.1), unlike first mode ISWs, second mode ISWs in this area have attracted much less concern due to the rarity of their wave types in the world's oceans. Following Yang et al. (2010), two types of second mode ISWs can be identified according to the shape of isopycnals in the upper and lower layers, i.e., concave and convex waves. A concave (convex) wave undergoes an increasing (a decreasing) and then a decreasing (an increasing) temperature evolution in the upper layer and the opposite evolution in the lower layer (Figure 7.2). Almost all of the observed second mode waves are of the convex type, and the first documentation of a concave type was reported by Yang et al. (2010) in which four such waves were recorded on the continental shelf of the northern SCS.

Modeling results in Chapter 4 have shown that concave waves as large as 80 m (amplitude of the isopycnal vertical displacements for the lower part of the wave) can be formed in the deep water of the northern SCS basin, due to the nonlinear superposition of wave signals generated by the two ridges in the LS. These waves can travel a long distance until they reach the shelf area. Meanwhile, a long-term mooring, which was located on the continental shelf with the local water depth being 350 m, was deployed in 2005 and 2006 under the joint Taiwan/US programs VANS and WISE (Yang et al. 2009, 2010). The mooring successfully recorded 78 instances of convex waves and 4 instances of concave waves, marking the first documentation of the latter type in nature. Early in situ measurements (Duda et al. 2004, Ramp et al. 2004) based on the ASIAEX around the shelf break of the northern SCS showed that no strong wave signals were generated locally. Thus it can be speculated that the observed second mode waves propagate from the deep ocean and experience gradual transformation along the decreasing topography, or even the transition of polarity, i.e., from the concave type to the convex type.

Apart from the above-mentioned observations of concave ISWs with a mooring, events of a

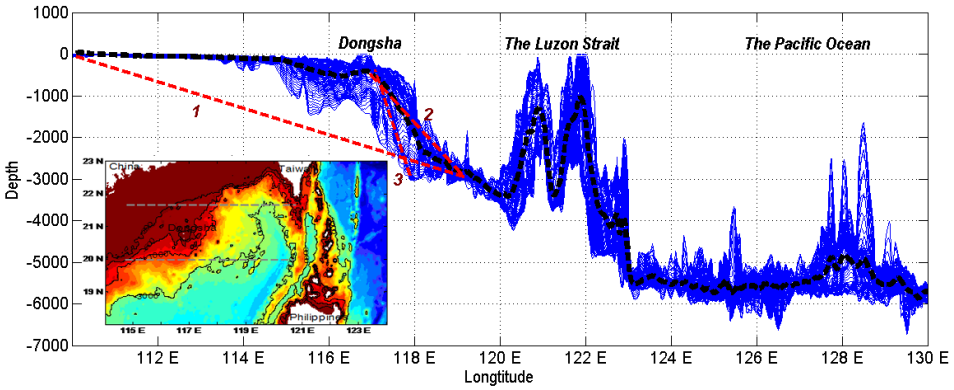

Figure 7.1: Zonal bathymetry in the northern SCS and the western Pacific Ocean (blue lines). The dashed black line is the averaged bathymetry, and dashed red lines 1-3 are its three representative linear slopes that will be used in the model configuration. The inset is a plane view of the bathymetry of the northern SCS, and two gray dashed lines bound the domain where the blue lines are chosen.

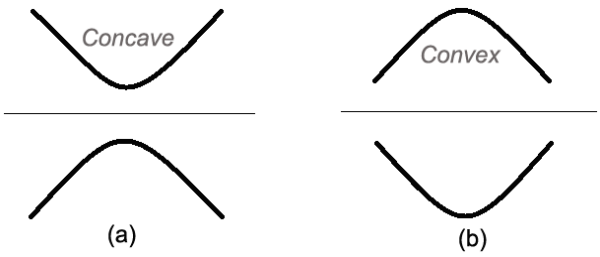

Figure 7.2: Sketch of a second mode ISW: a) a concave wave; b) a convex wave.

concave ISW and a multi-layered high mode were also recorded during a cruise measurement that was carried out in 2007 (see section 7.2). This work was inspired by the fact that second mode ISWs have been successfully reproduced with numerical models in deep water (Chapter 4) and observed with long-term moorings (Yang et al. 2004, 2009, 2010) and cruise measurements (section 7.2) in shallow water, and the fact that there is insufficient understanding of the shoaling process of second mode ISWs from the deep part of the ocean onto the shelf. A very large incident second mode ISW, which is far beyond the applicability of classic weakly nonlinear theory, is chosen to illustrate the idea of the shoaling process of second mode ISWs, regarding the specific case in the northern SCS.

7.2 Observational evidence of a concave wave and a high mode in the northern South China Sea

From June to July 2007, an in situ cruise measurement of ISWs was carried out in the northern SCS by R/V No.2 Dongfanghong. During this experiment, based on the 75 kHz RDI OS-75 ADCP, not only were several first mode depression waves captured, but a second mode concave wave and a multi-layered high mode were also detected. The sampling interval of the RDI OS-75 ADCP was 1 min. The vertical spatial resolution was 16 m.

Figure 7.3 is an event of a second mode concave wave that was recorded between 20:25 and 20:55 on July 19th 2007 around $116.5°E$, $21°N$. The left panel is the track of the research vessel when the ISW passed by, while the right panel is the temporal variation of the zonal velocity. Although part of the velocity field was smeared by the background flow or the instrument itself, a three-layered structure can still be clearly identified, with the maximum velocity in the cores of the three layers equal to -0.75, 0.55, and -0.22 m/s, respectively.

On July 16th 2007, the RDI OS-75 ADCP captured another fascinating wave at $117°E$, $20°N$, when the vessel headed northward between 11:35 and 13:10 (see Figure 7.4). A very complex structure, with three salient cores of westward flowing currents, can be established from the zonal velocity field. Despite the fact that the contoured zonal velocity profile does not strictly comply with the KdV theory, according to which the directions of the neighbouring two layers alternate, the multi-layered structure is undoubtedly the product of high modes.

The observation of such a concave wave and a high mode serves as one of the motivations for the numerical simulations, and their generation and structures will be further discussed later after the simulation results are presented.

7.3 Model configuration for the shoaling of a second mode internal solitary wave

The bathymetry data in the SCS was derived from ETOPO1 Global Relief Model, with a spatial resolution of 1'. Considering that the slope-shelf area in the northern SCS is quite irregular and spans a wide range in both zonal and meridional directions (Figure 7.1), the band between 20° and $21°40' N$ was chosen and then made an average of the west-eastward transect topography (see the dashed black line in Figure 7.1). In the numerical experiments, specific bottom profiles relating to the northern SCS were not chosen due to their wide variety, but only linear slopes with inclination angle α (with respect to the horizontal direction) were used. Three slopes which are representative of the topography inclination were selected (see the three dashed red lines), with line 2 being close to the realistic case, and lines 1 and 3 corresponding to the gentle and steep topography, respectively. Water depth in deep water and on the shelf was set to 3000 m and 400 m, respectively. An ideal schematic diagram of our computational area is shown in

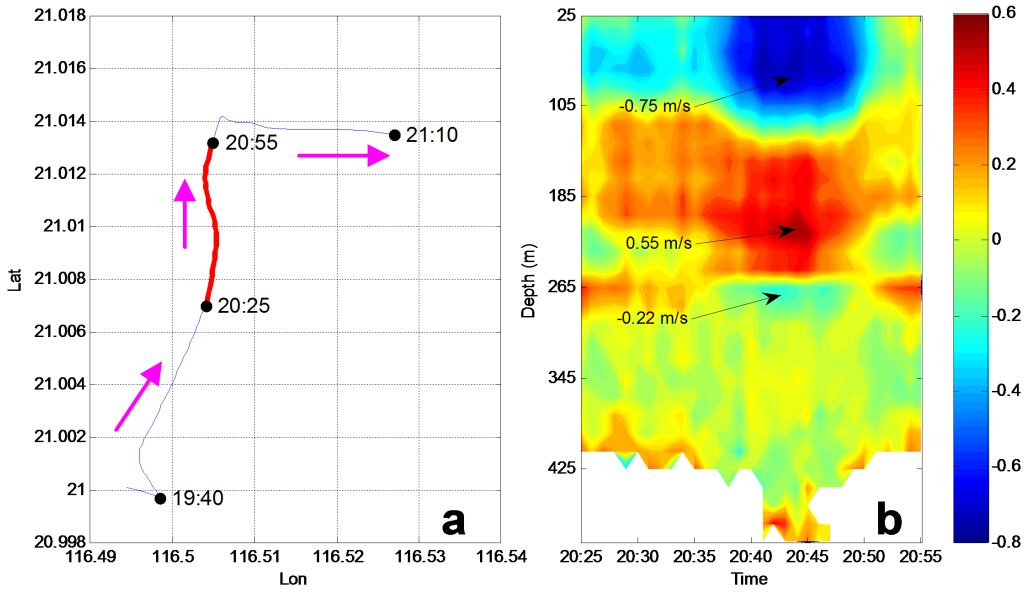

Figure 7.3: a) The track of the research vessel when the ISW passed by on 19th, July, 2007 around 116.5°E, 21°N. The red line corresponds to the time interval in b), and the arrows indicate the navigation direction of the vessel; b) zonal velocity field of the measured concave wave (m/s).

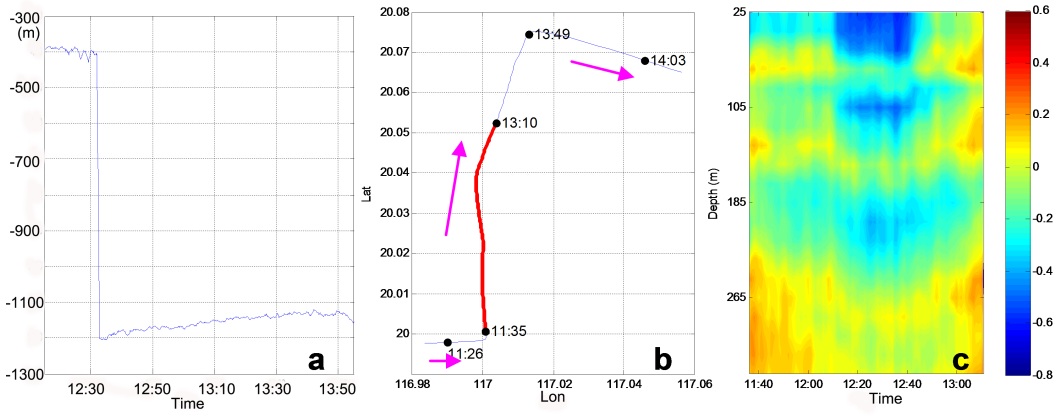

Figure 7.4: a) Local water depth measured by the research vessel when the ISW passed by on 16th, July, 2007 around 117°E, 20°N; b) the track of the research vessel when the ISW passed by. The red line corresponds to the time interval in c), and the arrows indicate the navigation direction of the vessel; c) zonal velocity field of the measured high mode (m/s).

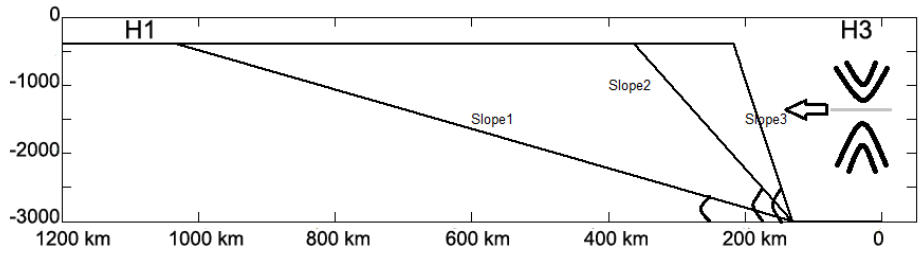

Figure 7.5: Schematic diagram of the computational area. The inclination angles of the three slopes are 0.1°, 0.645°, and 1.737°, respectively.

Figure 7.5.

MITgcm was employed to perform the 2D experiments. Spatial resolution of the model was 50 m and 10 m in the horizontal and vertical directions, respectively, and two sponge areas were added to the lateral boundaries with a decrease of resolution from 50 m to 10^5 m in order to avoid any reflections of internal waves from the boundary. There were 200 grid points in each sponge area and the grid therein was telescoped exponentially to obtain a smooth change of the resolution. The value of the time step was 12.5 s, which was short enough compared to the typical time scale of a second mode ISW. Background temperature and salinity profiles were shown in Figure 1.6, and summer stratification was used. The Earth's rotation was taken into account, with the value of the Coriolis parameter taken at the latitude of 20.5° N, which crosses the middle of the LS.

An important issue is the preparation of the initial model fields, i.e., the incident wave in the deep water. Apparently, a KdV wave cannot be directly used as the impinging shoaling wave, as it does not satisfy the Boussinesq equations solved by the MITgcm. However, the following two steps can be taken to obtain a proper initial wave: firstly, a basin with a constant depth (3000 m) was considered. Within the constant depth, a mode-2 concave KdV ISW was implemented into MITgcm by providing KdV solutions of horizontal velocity, temperature and salinity. In this first step, given the incompatibility of the weakly nonlinear and non-hydrostatic KdV solution to the fully nonlinear, non-hydrostatic MITgcm, the initial KdV-type profile evolves towards a new stationary second mode wave, solution of the Boussinesq equations of MITgcm. The modelled evolution process of the first step (figures not shown here) showed that the initial KdV wave with large amplitude was immediately modified, and a first mode depression wave appeared and propagated out faster than the rest of the waves. Behind the first mode ISW, a new concave wave was formed and continually evolved until this wave reached the new stationary solution. This stationary second mode concave ISW comes from the evolution of a KdV wave but satisfies the MITgcm equations. Secondly, this new stationary second mode ISW was then cut out from the rest of the wave field and, by implementing the shoaling topography, was then used as the initial incident wave for the problem of the interaction of a concave wave with the linear slope bottom topography.

7.4 Transformation of a large amplitude second mode internal solitary wave over the slope and shelf

First of all, KdV theory was re-examined (section 2.3.1). For first mode ISWs, KdV theory shows that positive and negative values of the quadratic coefficient α_1 (equation (2.25)) corre-

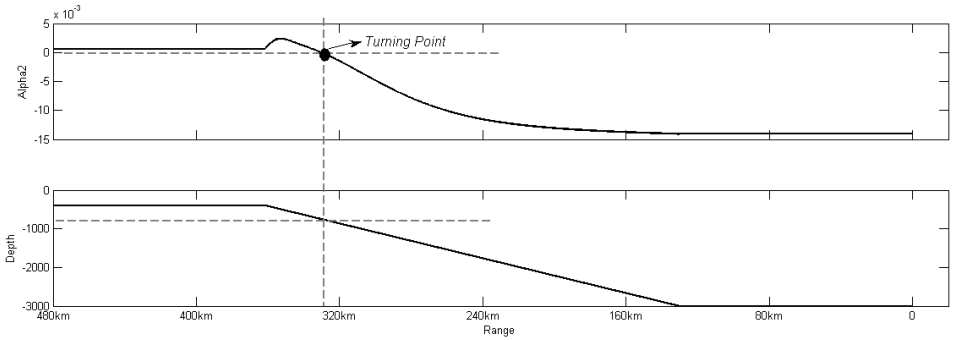

Figure 7.6: a) Coefficient of the quadratic nonlinearity of the KdV equation (second mode) calculated for the b) topography in the reference experiment.

spond to waves of elevation and depression, respectively. For mode-2 ISWs, positive α_2 and negative α_2 are related to convex and concave ISWs, respectively.

In this case with an incident concave wave and a straight slope (red line 2 in Figure 7.1), Figure 7.6 illustrates the dependence of the quadratic nonlinearity α_2 on the horizontal coordinate. It is clear that the coefficient changes its sign from negative to positive value at the depth of about 800 m, which implies that, under the circumstances of weakly nonlinear theory, an incident concave wave is supposed to change polarity from this turning point, and only internal waves of convex type can exist on the shelf. However, below one can see that when the incident wave is large, the transformation process extends a long distance from the turning point, and the incoming wave experiences several stages before it finally reaches a steady convex form on the shelf.

This section describes numerical experiments which were carried out to reproduce the shoaling process of the second mode concave ISWs. Input parameters, such as the stratification, inclination of the slope (0.635°) as well as the depth on the shelf (400 m) and in the deep water (3000 m) were taken close to those of the northern SCS slope-shelf area. The incident wave amplitude after initialization is about 100 m, which is a little bit larger than that predicted in Figure 4.2 with the 3D model. Below the evolution process of the incoming wave in three stages will be discussed: its evolution over the slope, transformation around the shelf break, and further development on the shelf.

7.4.1 Evolution over the slope

Figure 7.7 displays the vertical isotherm displacement and zonal velocity profiles of the incident concave wave after the adjustment process of the KdV solution, as was introduced in the previous section. One can see from this figure that the zonal velocity reaches its maximum value in the middle layer at the depth of 350 m, where the displacement of the isotherms changes sign (the nodal point). Below how the nodal point moves in the vertical direction can be seen. Using an analytical three-layer KdV model, Yang et al. (2010) concluded that the thickness of the middle layer plays a decisive role in the resulting waveform of a second mode ISW, and only the concave type could be generated when the thickness of the middle layer is greater than half of the total water depth. However, in the current model with continuous stratification, which is far from a three-layer structure, concave waves with very large amplitudes are reproduced, demonstrating to some extent the limitations of a three-layer model in the framework of weakly

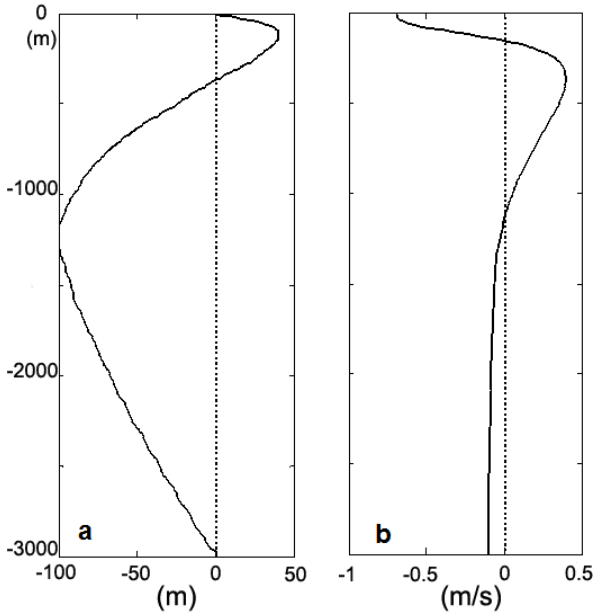

Figure 7.7: Vertical profiles of the a) isotherm displacement (m), and b) the zonal velocity (m/s), after the initialization of the KdV type wave.

nonlinear theory.

Figure 7.8 schematically illustrates how an incoming concave wave penetrates onto the slope-shelf. The figure shows the consecutive transformation process of the wave, with a time interval of 6 hours. Six representative isotherms were chosen to demonstrate this process. The rightmost wave in the dashed rectangle is where the initial wave is located. The initial wave profile keeps almost unchanged in the deep part of the slope until it reaches the depth of about 1500 m (at x=265 km), where it begins to undergo a pronounced transformation process. In this particular case with bottom inclination equal to 0.645°, the wave shoaling lies in a dispersive regime where ISWs disintegrate into a packet of secondary waves without any breaking events.

The rear face of the uppermost isotherm, T=24.7 °C, gets steeper and steeper and even becomes vertical above the shelf break. Afterwards, it disintegrates into a series of mode-2 waves of the more common convex type. Meanwhile, the frontal face of this isotherm begins to slope more gently and evolves towards a solitary wave-like structure (more details on the phenomena that occur in the shallow water will be elaborated on in the following sub-sections). The 20 °C isotherm, however, experiences much smoother changes in the wave profile. The frontal wave becomes extremely flat near the shelf break, and after short adjustment on the shelf, the whole wave shape is nearly flat, indicating that it is now located around the depth of the nodal point. The 15.2 °C isotherm, originally located slightly above the depth of the nodal point, becomes flat above the depth of 1200 m, and gradually develops into a wave structure that has the opposite polarity from the 24.7 °C isotherm on the shelf. The 12.4 °C isotherm, which is flat (almost at the depth of the nodal point) at the initial position, gradually gets elevated on the slope and finally forms a similar structure to the 15.2 °C isotherm. The lower two isotherms, i.e., T=8.5 and T=4.25 °C, maintain their shapes until they reach the bottom, where they break

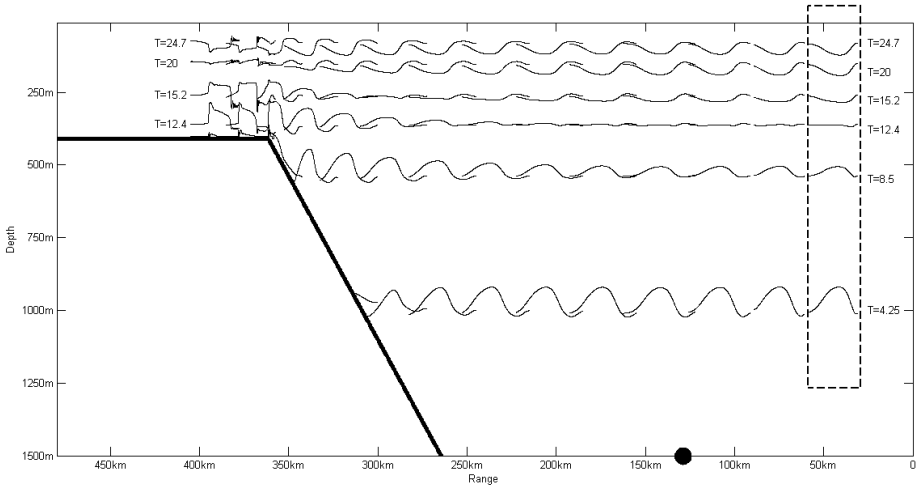

Figure 7.8: Transformation process of an incoming concave ISW (rofile plotted at time intervals of 6 hours). The wave in the dashed rectangle is where the initial wave is located. Six isotherms, T=4.25, 8.5, 12.4, 15.2, 20, and 24.7 °C are chosen to illustrate the process, and only the upper 1500 m is shown (the black dot is the place where the linear slope starts).

and dissipate.

The vertical position of the nodal point, which is a function of the stratification and local topography, changes significantly during the shoaling process. This change is particularly apparent when the wave starts to reverse its polarity. The initial position of the nodal point resides at the depth of 350 m, and starts to move upwards at about x= 250 km. This is accompanied by the gradual formation of a convex wave in the rear face of the incident concave wave. The nodal point can finally reach 140 m after the wave penetrates onto the shelf.

Recall that weakly nonlinear theory predicts that a concave wave should convert to a convex wave (i.e., polarity reversal) after it passes through the turning point (see the beginning of section 7.4). However, when the incoming wave is strongly nonlinear, as is the case with the fourth wave profile from the left in Figure 7.8 which is above the approximate depth of 800 m, the frontal face of the wave becomes much more gently sloping and a very pronounced convex-like wave can be registered at the rear face. This shows the tendency for the change of wave polarity. Later, it can be seen that the still existing concave wave will gradually 'disappear' after it penetrates onto the shelf.

7.4.2 Transformation around the shelf break

Figure 7.9 displays the wave profile in detail at 4 snapshots: T=64 h, 66 h, 70 h, and 78 h. The initial concave wave penetrates along the slope without any essential changes until it comes close to the shelf, where the leading edge is flatter and the rear face steeper (Figure 7.9a). Similar behavior of wave shoaling process for first mode depression waves was previously reported both in numerical (Vlasenko & Hutter 2002, Vlasenko & Stashchuk 2007, Scotti et al. 2008) and experimental efforts (Helfrich 1992, Michallet & Ivey 1999). Note that in front of the concave wave and the trailing convex waves, a very weak first mode-like wave is produced and prop-

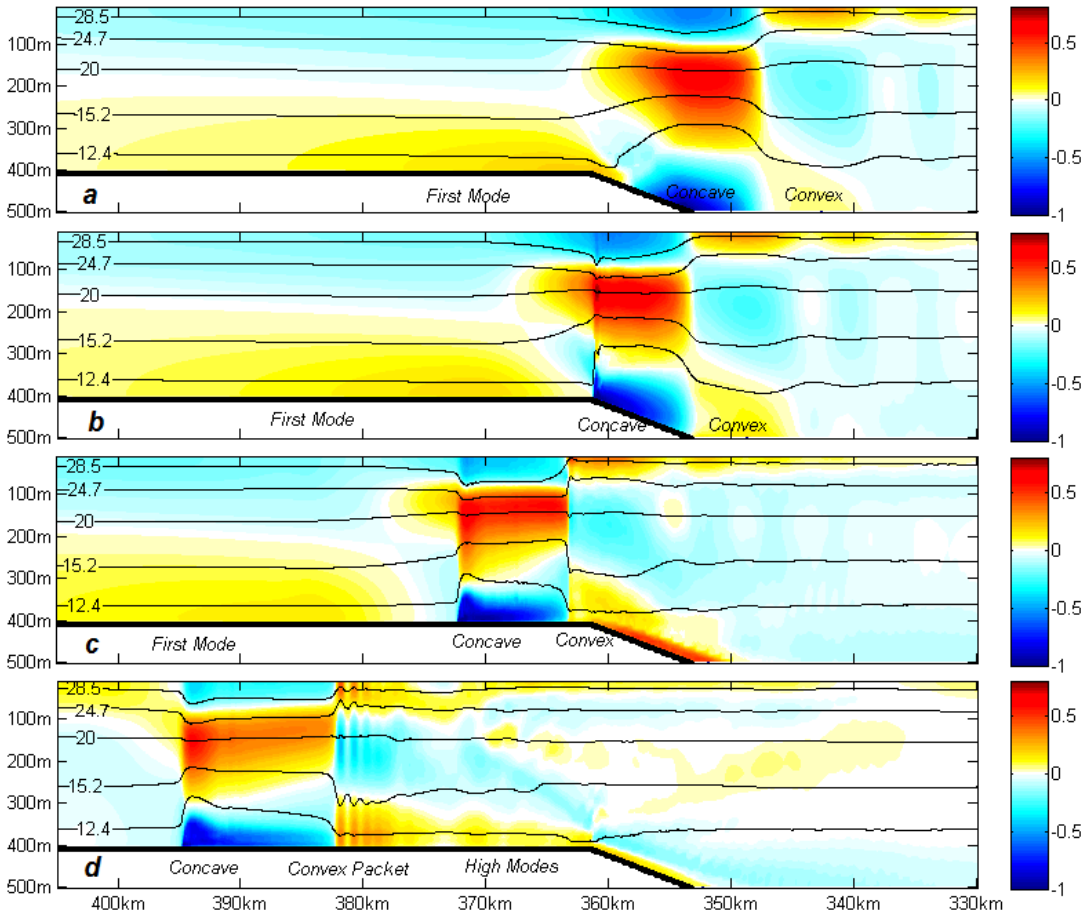

Figure 7.9: Wave zonal velocity fields (m/s; positive/negative corresponds to eastward/westward motion) on which five isotherms (°C) are superposed around the shelf break at 4 snapshots, T= 64, 66, 70, and 78 h (from top to bottom).

agates away onto the shelf. Such an energy transfer to the neighboring modes is particularly salient in our model and will be discussed in the next sub-section.

At T=66 h (Figure 7.9b), the frontal face of the concave wave suddenly becomes very steep at the shelf break (see isotherms 28.5, 15.2 and 12.4 °C). The 12.4 °C isotherm even appears to be vertical. Meanwhile, the rear face of the concave wave continues to steepen, and the trailing convex waves become more pronounced. Notice that the wave structure located at about x=342 km much resembles a secondary wave of the concave type if merely judging from the temperature field, but in fact, such a structure is produced by the undulation of the two ambient convex waves, as can be clearly seen from the zonal velocity field. At T=70 h (Figure 7.9c), the wave has just passed through the shelf break and starts to adjust to the new circumstances on the shelf. The incident concave wave, although still maintaining its three-layer structure for velocity, has deviated seriously from a standard concave ISW. The isotherms are almost flat and lower (higher) than the surrounding environment in the upper (lower) layer. The rear face of the concave wave has become very steep and is about to disintegrate into solitary wave trains of convex type. The frontal face of the wave, however, has become smoother and the

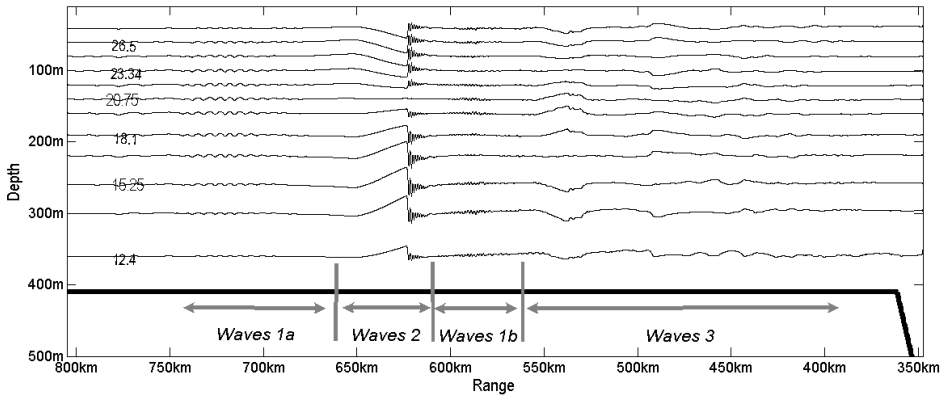

Figure 7.10: Isotherms at T=176 h. Three types of waves are classified, i.e., Waves 1a and 1b, Waves 2, and Waves 3

current velocities larger than the previous structure. Also note that the fluid motion on the slope is quite intense at this moment, with velocities as high as 0.55 m/s. In fact, such a zone with pronounced off-shore velocity spans almost half of the slope area, and is undoubtedly a place potentially efficient for diffusion and mixing, and thus affects the dynamical or biological processes above the continental slope in the real ocean.

Figure 7.9d shows that at T=78 h a packet of convex ISWs has formed, behind which are some very complex structures due to the superposition of high modes that will disintegrate after further development on the shelf (see the next sub-section). The distance between the frontal face of the concave wave and the rear convex packet has increased from 8.5 km in Figure 7.9c to 12 km at this moment. Also, the energy is mainly focused in the frontal part of the wave at this instant, which may make one surmise that it will evolve towards a new ISW of concave type with smaller amplitude. This gives rise to some questions about the fate of the concave wave, which seems to be sustained in spite of the prediction of the KdV model.

7.4.3 Further development on the shelf

Further evolution of the leading concave wave (not an ISW any more) is consistent with our prediction made in the beginning of section 7.4, i.e., it does not evolve towards an ISW, but instead, the leading edge of the concave wave becomes more and more gently sloping compared with that at T=78 h. As a consequence, the rear convex soliton packet catches up with the frontal concave wave and eventually moves forward together with it as a whole.

Figure 7.10 is an episode at T=176 h, when the waves have traveled for quite a long distance on the shelf. Three types of waves can be identified in this figure, i.e., some small-scale waves (Waves 1a and 1b), the coupling concave wave and a packet of convex waves (Waves 2), and some prominent high modes (Waves 3). Zonal velocity fields of Waves 2 and 3 are shown in Figure 7.11, and the generation process of Waves 1a, Waves 1b, and Waves 2 are shown in Figure 7.12. Detailed analyses and descriptions of these waves are separately exhibited below.

7.4.3.1 Structure of Waves 2

As can be seen from Figure 7.10, previously separated frontal concave wave and rear convex wave packet 'rejoin' again (the detailed process will be shown later), and the leading edge of

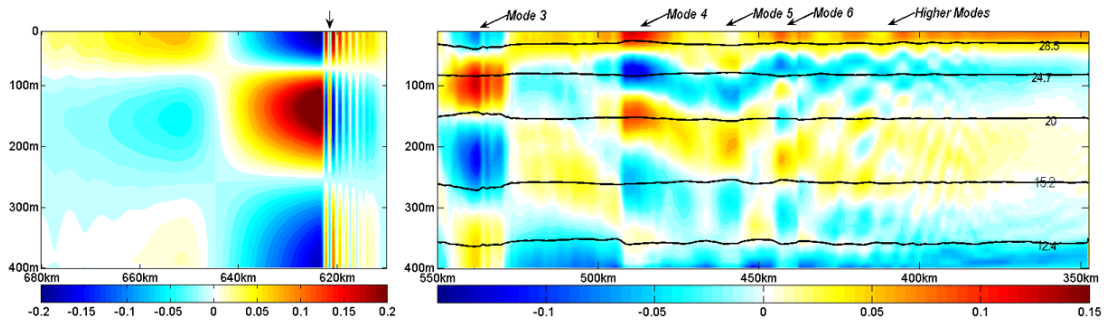

Figure 7.11: a) Velocity field (m/s) of Waves2 (left panel); and b) velocity field (m/s) of Waves 3 on which five isotherms (°C) are superposed. Higher modes can be identified and are labeled in the figure.

the initial concave wave slopes very gently. A close-up view of Waves 2 is shown in Figure 7.11a, and one can clearly see from the zonal velocity field that the concave wave has been largely deflected from the standard shape of an ISW, and it is followed by a train of convex waves which are not rank-ordered (see the arrow in Figure 7.11a). However, such waves will become rank-ordered as soon as the interaction between the frontal wave and the rear packet is finished.

7.4.3.2 Generation process of Waves 1a, 1b, and Waves 2

Figure 7.10 shows short waves whose horizontal wavelengths (about 3 km and 1 km for Waves 1a and 1b, respectively) are well resolved by the numerical grid. Also considering that they propagate leftward with specific phase speeds, they are unlikely to be generated by the instability of numerical computation. Figure 7.12 illustrates clearly how such short waves arise and how the shape of Waves 2 is formed. The upper left panel (Figure 7.12a) depicts the instant when the trailing convex wave train is chasing after the frontal concave wave. Then, the rear wave train reaches the critical point where it starts to 'merge' with the frontal wave that is very gently sloping at the time (Figure 7.12b). During the merging process, Waves 1a gradually form and ride on the very smooth slope of the frontal wave (Figure 7.12c). After that, they propagate out of the system, and are stretched to a much wider range (Figures 7.10 and 7.12d). Waves 1b are formed at the same time as Waves 1a during the merging process, but they obviously have smaller scales and travel much more slowly, and as a consequence they gradually fall behind. By this point, the shape of Waves 2 is formed after the merging process, and it continually evolves towards a wave packet with rank-ordered convex ISWs.

The emergence of these short waves has been examined very carefully in order to exclude any external factors that may be responsible for their generation. No waves are reflected from the lateral open boundary, and the above coupling waves all propagate freely without external forces or other wave motions in the front and rear, demonstrating that such short waves are entirely the creation of the interactions of the leading concave wave and the trailing convex ISW packet.

The generation mechanism of such waves closely resembles that discussed earlier in Chapter 5, in which a packet of first mode short-scale waves riding on a second mode concave wave is produced during the disintegration process of a multi-modal baroclinic bore, and also when a first mode depression ISW surpasses a concave ISW that travels more slowly. By solving the Taylor-Goldstein equation that includes the background current, the short waves exist due to

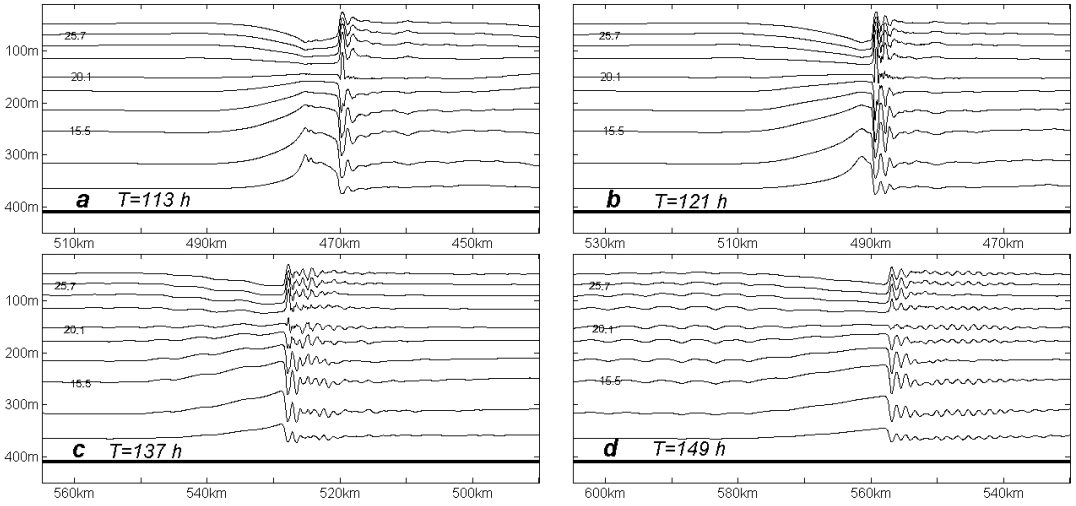

Figure 7.12: Interaction of the rear convex wave train and the frontal concave wave. Waves 1a and 1b are produced during the interaction process (see section 7.4.3.2). Panels a) to d) correspond to isotherms (°C) at T=113, 121, 137, and 149 h, respectively.

the specific vertical structure of horizontal velocity (multi-layered) induced by the second mode solitary wave. Considering the much more complicated vertical structure of the interacting system in our case, i.e., the frontal single wave and the rear wave packet with reverse second mode polarity, the sheared background velocity field is more prone to produce secondary waves.

The reason that the frontal concave wave that formed after passing the shelf break gets increasingly flat, rather than evolving towards a concave type soliton, is presumably attributed to the fact that, as discussed in the beginning of section 7.4, the quadratic nonlinear coefficient, which determines the polarity of an ISW, is positive on the shelf break, although it is close to zero (see Figure 7.6). This implies that the shelf area suppresses the generation of concave ISWs or at least is not favorable for their existence. On the other hand, ISWs of convex type can survive in such circumstances and persist for a very long time.

7.4.3.3 Structure of Waves 3

Very rich and prominent wave structures exist behind Waves 1 and 2 (Figure 7.11b). As can be seen in Figure 7.11b, very high modes, from mode 3 all the way up to mode 6, although not fully developed, can be identified from the multi-layered velocity field. On the right hand side of Figure 7.11b, multiple beams with different inclination angles are registered, showing a superposition of different high modes. One should note that the high modes exhibited above are subject to the impact of the background flows engendered by the anterior waves, especially Waves 2 and 1b. Taking into account their multi-layered vertical velocity structure, which tends to be unstable even when small external influences are imposed on them, the shapes of the modeled high modes deviate somewhat from the traditional KdV types of ISWs (comparisons not shown here). Such behavior of higher mode generation, obtained here directly from numerical runs, was previously described in some theoretical and experimental papers based on weakly nonlinear theory (Helfrich & Melville 1986, Helfrich 1992, Michallet & Ivey 1999), and it was found that the shoaling of a first mode depression wave leads to the generation of second modes during the propagation process up the slope, demonstrating an energy transfer to the

other modes. The interaction of ISWs with a slope-shelf topography also has much in common with the mechanism of wave scattering by underwater sills. Vlasenko & Hutter (2001) showed experimentally and numerically that both transmitted and reflected second mode soliton-like waves are produced after the interaction of the incoming depression wave with the sill.

The linear semi-analytical numerical model described by Vlasenko et al. (2005), as introduced in section 7.1, concerns the splitting of an incident wave into the neighboring baroclinic modes as a function of stratification, and the height and width of the slope. A qualitative estimation of the scattering of incident wave energy was attempted, using this model with the bottom profile identical to the one applied above, and it was found that using a linear scheme, continental slope in the northern SCS is not able to transmit energy of second mode internal waves to the neighboring modes at all because it is not steep enough. However, for nonlinear solitary waves, the generation of first and higher modes is so conspicuous, indicating the great discrepancies between these two cases. Since theoretical understanding of the fully nonlinear ISWs is still unsatisfactory, more analytical work of the shoaling process over variable topography is needed in the future to quantitatively estimate the energy transfer rate to the other modes.

7.4.4 Discussion of the measurements associated with the simulations

The measured concave wave (section 7.2, Figure 7.3) could be at any stage that we discussed above, considering the complex bathymetry and non-straight slopes in the northern SCS, although its location was in relatively shallow water. Whether a convex wave packet behind this wave (see Figure 7.9d) existed or not at that time could hardly be confirmed due to the limitation of the sampling frequency (1 min). More specifically, due to the high complexity of the topography in the northern SCS (see the blue lines in Figure 7.1), the shape of the continental shelf is far from a linear type, which implies that quite different scenarios may occur even when the depth of the shelf is the same. (This can be corroborated by a three-dimensional shoaling experiment that was done, in which real topography was included, but with much coarser spatial resolution). Apart from the water depth, the ISWs, especially the multi-layered second and higher modes, are also susceptible to various factors, like the background currents and the related shear, frequent mesoscale eddies from the LS, local barotropic tides, typhoons, etc. It is not surprising if the measured wave is deviated from the modeled or theoretical one. However, such a result at least corroborates the existence of second mode concave waves in the northern SCS, and together with the mooring data obtained by Yang et al. (2010) (whose mooring was located in the northeastern direction) and the numerical simulation discussed in Chapter 4, conclusions can be reached that second mode concave waves are also very common features rather than sporadic processes in the northern SCS.

As for the measured high mode with multiple layers, it is likely to be generated by the shoaling process of a second mode ISW, due to the scattering of wave energy to the neighboring modes by the impinging wave, as can be clearly seen in Figure 7.11b. Moreover, according to the measurement, the local water depth change in the north-south direction is very abrupt, i.e., the value decreases from 400 to 1200 m in several hundred meters (Figure 7.4a), corresponding to a very steep topography, which, according to the previous work on shoaling waves (Helfrich & Melville 1986, Vlasenko et al. 2005) and the sensitivity experiments that will be presented in section 7.5, is more favorable for the generation of high modes.

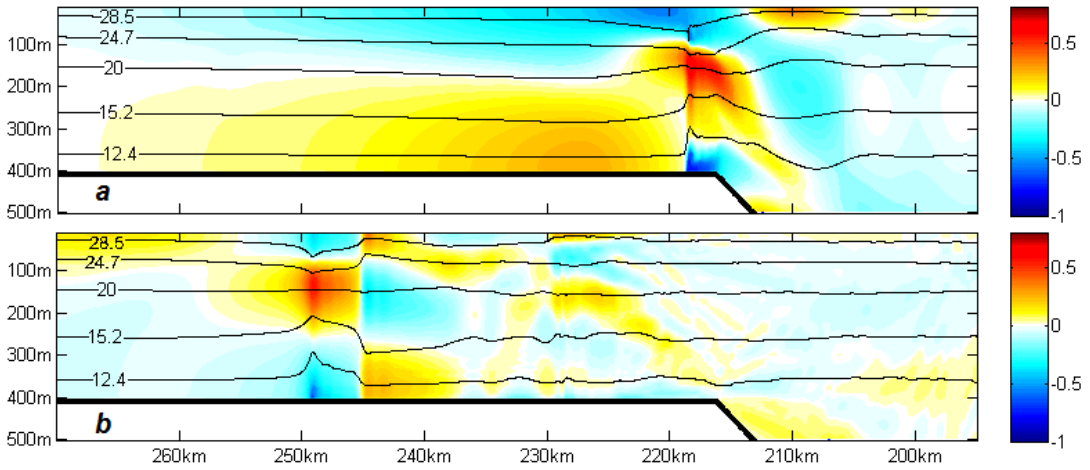

Figure 7.13: Same as Figure 7.9 but at T=35 and 48h for the steeper topography (sensitivity experiment Exp1).

7.5 Sensitivity of wave shoaling to the bottom inclination and wave amplitude

The reference experiment discussed above was performed with topography typical of the continental slope and shelf in the northern SCS, and the amplitude of the incident concave wave is as large as 100 m. In this section, several additional numerical experiments were conducted to study the sensitivity of the model to various bottom inclinations and wave amplitudes: Exp 1 and 2 were performed with bottom inclination equal to 1.737° and 0.1°, which respectively correspond to the steep and gentle case of the topography in the northern SCS (see Figure 7.1); amplitudes of the incident wave in Exp 3 and 4 were reduced to 70 m and 30 m to contrast with the strong nonlinearity in the reference experiment. The other parameters were completely the same.

The results with steeper topography (Exp 1) are illustrated by Figure 7.13, in which two snapshots are chosen to show the wave evolution process. The entire wave is just above the shelf break in the upper panel, and in the lower panel, the trailing edge of the concave wave is beginning to disintegrate into an undular bore that contains several convex ISWs. It can be concluded from Figure 7.13a that the wave profile changes more drastically when the steepness of the topography intensifies (compared to Figure 7.9b), and the upper part of the whole wave looks much more compact, unlike that in the reference experiment where the rear convex wave remains almost in the same horizontal position. As a consequence, the wave system, including the leading concave wave and the rear convex ones, is much less horizontally 'stretched' during the evolution process on the shelf (see Figure 7.13b). To be more specific, the rear convex ISW train catches up and merges with the frontal concave wave 45 km away from the shelf break, which is only one third of the distance traveled by the convex waves before merging occurs in the reference experiment. Qualitative comparison of Exp 1 with the reference experiment exhibits similar features of the transformation process, the final shape of the undular bore, and the high modes, except that the short waves shown in Figure 7.12 do not show up, which is very likely due to the much shorter interaction time of the frontal wave and the rear convex wave train.

On the contrary, as shown in Figure 7.14, when the incident wave penetrates onto a slope with

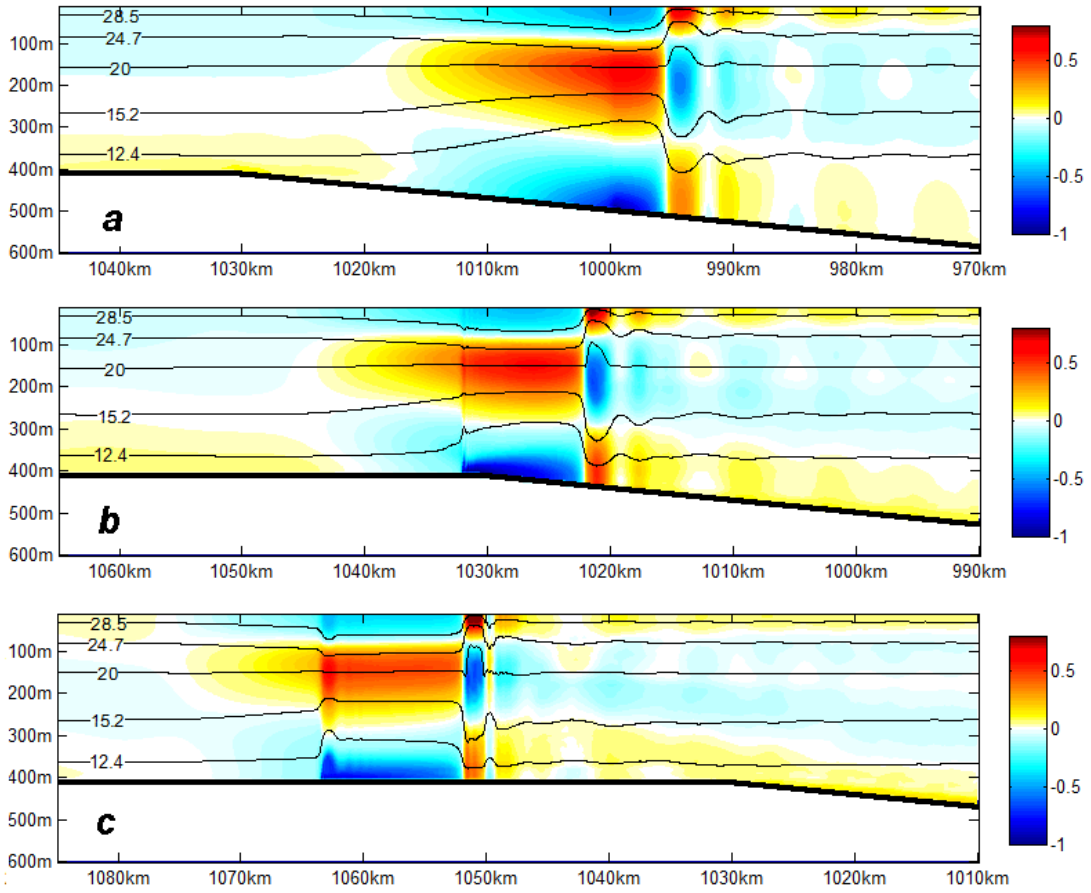

Figure 7.14: Same as Figure 7.9 but at T=207, 217 and 229 h for the more gently sloping topography (sensitivity experiment Exp2).

an inclination angle of 0.1°, which corresponds to a very gently variable topography, the situation is quite different from the previous two cases. Three scenarios, correlating respectively with the moment before, just, and after passing by the shelf break, are exhibited in the figure. A very salient feature is that a train of soliton-like convex waves has already formed behind the initial concave wave before it reaches the shelf break. This is understandable considering that the width of the continental slope in this sensitivity run is several times larger than that in the reference experiment, which means that the wave has more time to adjust to the changing environment, during which the balance between nonlinearity and dispersion is violated. Hence, the incident concave wave has essentially converted to its counterpart form over the slope (recall that the turning point is located somewhere around 800 m). Nonetheless, the very steep structure, just like that in Figure 7.9b, still appears immediately after the very gentle wave front reaches the shelf break (Figure 7.14b), and such a structure soon develops into a soliton-like wave of concave type (Figure 7.14c). But once again, as discussed in the reference experiment, such a wave actually fails to evolve towards a soliton. Instead, it gets increasingly flat and finally is caught up by the rear wave packet.

Note that the amplitude of the leading wave in the rear packet can reach a size of 80 m in Exp 2, and the first and high modes generated in this experiment are much weaker than those in the

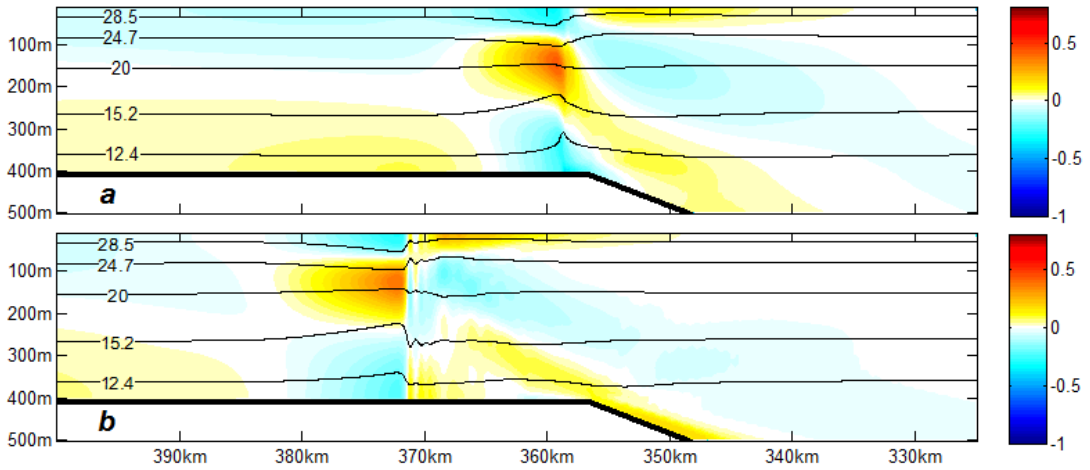

Figure 7.15: Same as Figure 7.9 but at T=67 and 73 h with the amplitude of the incident wave equal to 30 m (sensitivity experiment Exp4).

reference experiment, illustrating that energy transfer to the neighboring modes is much less efficient when the bottom topography is very gently sloping. The same conclusion was reached by the semi-analytical linear model developed by Vlasenko et al. (2005).

Exp 3 and 4 concern the influence of the amplitude of the initial wave on the resulting wave fields. When the amplitude is reduced to 70 m (Exp 3), no noticeable discrepancies occur (figures not shown). The main difference between Exp 3 and the reference experiment is that the transformed wave, after penetrating onto the shelf, is much less stretched, similar to the behavior of waves in Exp 1 (but wave behaviors around the shelf break are different from those in Exp 1). As for Exp 4 with the initial wave amplitude of 30 m, which more or less lies in the weakly nonlinear regime, the wave shoaling process reveals quite distinct features (Figure 7.15). The leading edge of the incident wave has only become a bit more gently sloping when it comes to the shelf break, followed immediately by the steep rear face. The abrupt trailing edge soon disintegrates into a group of small convex waves that move forward steadily. Such a scenario is quite different from that in the reference experiment, in which a solitary wave-like structure is formed in the smooth frontal face, 'chased' by the rear convex wave packet, and finally the two systems rejoin and propagate forward together with a permanent form. Note that high modes are also clearly visible in this experiment, although weaker than in the reference experiment.

7.6 Summary of shoaling process of a second mode internal solitary wave over a slope and a shelf

Unlike the investigation of the generation and propagation processes of ISWs in the LS and the northern SCS, studies on their shoaling process have been lacking except for several papers based on data analysis of some moorings deployed on the continental slope of the northern SCS (Duda et al. 2004, Lynch et al. 2004, Ramp et al. 2004, Alford et al. 2010, Ramp et al. 2010). Considering the wide range of the continental slope-shelf area in the northern SCS, wave signals captured by the deployed moorings cannot represent wave properties in the whole area, and as a consequence, the three-dimensional MITgcm, with high resolution and real topography, can be employed to study this issue. To fulfill this aim, a pilot theoretical study on shoaling second

mode ISWs over a straight slope is carried out in the present paper.

Specific interest in the shoaling process of a second mode concave ISW with large amplitude has been given, with the model setup close to the realistic situation in the northern SCS (stratification, depth, and inclination of the slope) where, according to in situ measurements (Yang et al. 2004, 2009, 2010) and numerical simulations (Du et al. 2008, Vlasenko et al. 2010), very active second mode ISWs exist, despite the rarity of such waves in the nature. A cruise in the summer of 2007 also measured several ISWs in the northern SCS, including a concave ISW and a multi-layered high mode. The evolution of large amplitude second mode ISWs on the shelf may play a significant role both in the material transport processes and in oceanic engineering, either directly by convection effects or indirectly by the generation of turbulence and mixing. Unfortunately, such type of motion, which is far beyond the scope of frequently exploited weakly nonlinear theory, has not yet been examined. The 2D fully nonlinear, non-hydrostatic MITgcm with very fine temporal and spatial resolution is employed here to comprehensively study this issue, with the aim to fill this gap.

Modeling results show that the wave form does not show any evident changes in the deep water during the penetration process over the slope, but strong transformation starts to take place when the wave is approaching the shelf break, although the velocity field still remains basically three-layered. A convex type wave comes into birth at the trailing edge of the incident wave near the turning point, and it gradually disintegrates into a group of internal solitons due to the steepening of the rear wave profile. On the other hand, the frontal face of the wave, which gets flatter and flatter on the slope, forms a steep structure right above the shelf break. However, this steep structure shows no tendency to evolve into a soliton, instead getting increasingly flat again while evolving on the shelf. The trailing convex wave packet travels faster and merges with the frontal concave wave. During the merging process, some small-scale waves are generated due to the complicated zonal velocity structures of the second mode ISWs. Finally wave packet with rank-ordered convex ISWs moves forward steadily on the shelf, followed by a group of high modes.

The generation of first and higher mode internal waves shows an energy transfer from the initial second mode wave to the neighboring modes. The linear semi-analytical model delineated by Vlasenko et al. (2005) fails to reproduce such an energy redistribution with the bottom topography resembling the situation in the northern SCS, which is most likely due to the strong nonlinearity of our configuration.

Two sensitivity runs with different topography inclination angles (larger and smaller) are performed to study the effects of the bottom topography. It was found that the wave profile is subject to a more abrupt change near the shelf break when the slope becomes steeper, and the resulting waves on the shelf are less stretched, i.e., the trailing convex wave packet rejoins the frontal concave wave at a distance much smaller than that in the reference experiment. On the other hand, when the topography is much more gently sloping, the convex wave packet, which is formed after certain evolution processes on the shelf in the previous experiments, appears before the shelf break, presumably due to the much longer adjustment time over a wider slope. Another two experiments that are sensitive to the amplitude of the incoming wave show that no noticeable discrepancies exist when the amplitude is reduced from 100 m to 70 m, but for reduction to 30 m, the wave profile starts to be deformed only after it passes through the shelf break, where the leading edge is more gently sloping, followed immediately by a packet of convex ISWs, exactly like the final stage of wave evolution in the reference experiment. High

mode signals are still evident, but they are not very pronounced.

The shoaling process of the incident waves in the northern SCS includes the first mode depression waves and the second mode concave waves, and the impinging process of a large amplitude first mode ISW with specific topography in the northern SCS will be simulated in the next chapter.

Chapter 8

The effect of rotation on shoaling of ISWs in the northern SCS

[1]

While the last chapter heuristically studied the shoaling process of a large amplitude second mode ISW over a slope that resembles the northern SCS, this chapter focuses on the shoaling of more general first mode ISWs over the wide 3D northern SCS slope and shelf. The effects of rotation are illustrated by 3D runs and are scrutinized by a series of 2D runs.

8.1 An introduction of wave shoaling and rotational effects in the northern South China Sea

For the internal waves in the northern SCS, their generation and propagation are the most intensively investigated. In contrast, wave shoaling is comparatively less understood. The northern SCS continental slope features a transition of topography from over 3000 m to several hundreds meters in a few hundreds kilometers (Figure 8.1). Three-dimensionality of the bathymetry is obvious. Numerous banks are distributed both in the deep and shallow water, among which the most striking one is the Dongsha Atoll, which is much steeper on the eastern side and connects to the continental slope, whereas on the western flank it transits smoothly to the continental shelf.

The radiated internal waves from the LS are a superposition of high-frequency ISWs and long internal tides. They impinge on the shoaling bathymetry, which further leads to wave transmission, refraction, reflection, and dissipation. It was found that a great portion of the wave energy is locally dissipated near the Dongsha Atoll (St. Laurent 2008, Klymak et al. 2011), whereas the rest of the wave energy mostly dissipates in the very shallow water after further evolution on the shelf. The pilot Asian Seas International Acoustic Experiment (ASIAEX) carried out in a small region of the SCS margin led to a few publications (Orr & Mignerey 2003, Duda et al. 2004, Ramp et al. 2004) that examined the ISW properties and the change of wave forms when propagating up towards the shelf. With an array of moorings to the east of the Dongsha Atoll (depths between 100 m and 285 m), Fu et al. (2012) observed the detailed shoaling process of large amplitude ISWs that transformed from waves of depression to waves of elevation. Lien et al. (2012) captured ISWs with trapped cores that are caused by shoaling topography on the continental slope of the northern SCS, and claimed that apart from the shoaling topographic effects, wave breaking and the trapped cores can further trigger the ISW disintegration process.

The propagation of internal tides and the subsequent fission into ISWs are fundamentally influenced by the Earth's rotation. Its effects have been examined by many authors (Gerkema 1996, Helfrich & Melville 2006, Helfrich & Grimshaw 2008, Grimshaw & Helfrich 2012). In

[1] This chapter is mostly based on the paper Guo & Vlasenko (2012)

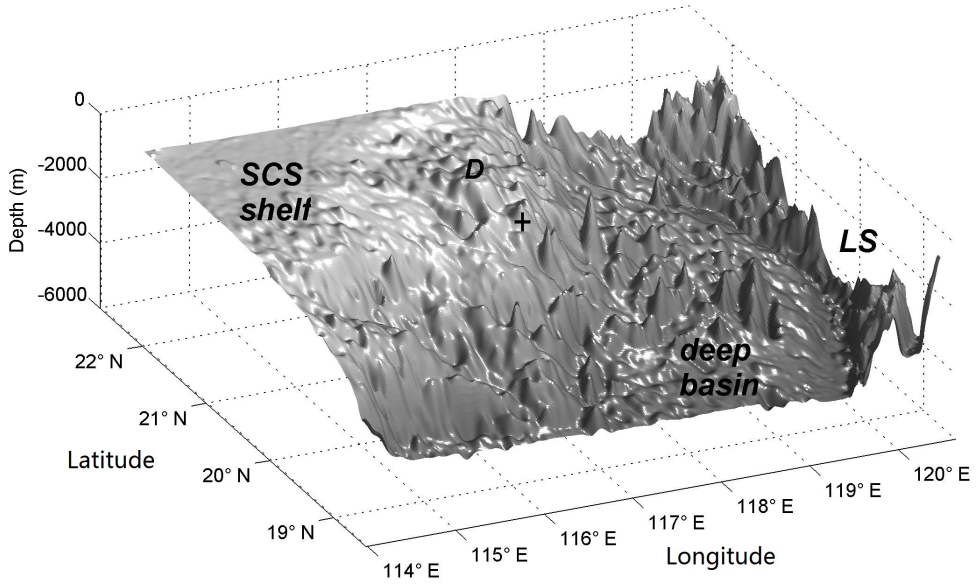

Figure 8.1: 3D topography of the modelling domain. 'D' denotes the Dongsha Atoll, whereas '+' indicates one of the underwater banks which has large impact on the propagation of ISWs (Figure 8.3)

general, when the length scales of the waves are comparable with the internal Rossby deformation radius L_R ($L_R = c/f$, where c is the phase speed of linear long wave, and f is the Coriolis frequency), as is often the case with long internal tides, nonlinearity (scaled by a/H, where a and H are respectively a wave amplitude and a depth scale) can be balanced by rotation (scaled by l/L_R, where l is a wavelength scale), and nondydrostatic effects (scaled by $(H/l)^2$) can be ruled out (Helfrich & Grimshaw 2008). However, when the nonlinear effects are strong enough to lead to the disintegration of the internal tide into ISWs, nonhydrostatic effects come into play and the rotational effects are less significant. As for the case in the northern SCS, using weakly nonlinear theory, Farmer et al. (2009) explored the effects of nonlinearity and rotation on the formation and propagation of ISWs and found the existence of rotation could significantly hamper the disintegration of internal tides. The effects were further examined by Li & Farmer (2011), who employed the fully nonlinear, weakly nonhydrostatic two-layered model of Helfrich & Grimshaw (2008) coupled with a linear generation model. On the other hand, despite the very short scale compared to L_R, for ISWs traveling a long distance that exceeds L_R, rotational effects can be important and lead to severe radiation of secondary waves (Grimshaw et al. 1998, Helfrich & Grimshaw 2008).

This investigation was motivated by the lack of comprehensive investigations of ISW shoaling process in the northern SCS. Given the potential impacts of ISW shoaling on the near-shore engineering, ecology, and oceanic dynamics, it is worthwhile to carry out such a numerical research, aiming at giving a general landscape view of wave shoaling process in a 3D context. Shen et al. (2009) conducted numerical runs with a fully nonlinear, nonhydrostatic model but the model domain was only confined within the ASIAEX area and thus cannot reflect the overall features in the whole northern SCS, considering the wide spanning of the continental slope and

shelf in the region (Figure 8.1). Note that the intruding internal waves include not only ISWs, but also long internal tides with multiple modes and frequencies (Klymak et al. 2011), which can make the analysis quite complex and ambiguous. To examine the effect of rotation on wave shoaling, only first mode large amplitude ISWs are considered in this paper. Special attention is paid to the combined effect of shoaling topography and rotation.

8.2 Model configuration of three-dimensional wave shoaling

The 3D MITgcm was used in this study. Realistic topography of ETOPO1 dataset was used (Figure 8.1). For the 3D case, the modeling domain extends from $19°45'$ to $22°N$ and from $114°30'$ to $120°30'E$, which nearly covers the whole area where ISWs are visible on SAR images (Figure 1.3). Water depth greater than 3000 m in the deep region was all set to 3000 m. Considering that topography dataset is not accurate near the Dongsha Atoll, and also for the purpose of stabilizing the model, water depth shallower than 20 m around the atoll was all set to 20 m. Horizontal resolutions in the Ox and Oy directions were 250 m and 1000 m, respectively. A discussion of the sufficiency of the horizontal resolutions in delineating wave evolution will be presented later. 180 layers were used in the vertical direction, with a resolution of 10 m in the upper 1500 m and of 50 m in the lower 1500 m. Telescoping grids and Orlanski-type boundary conditions were implemented on the four open boundaries to radiate the waves out and prevent wave reflections. The time step was equal to 12.5 s. Background stratification was derived from the summer climatological World Ocean Atlas (2009) (Figure 1.6), and horizontal homogeneity was assumed in the model initialization.

Since the main purpose of this chapter is to study the ISW evolution but not the generation process itself, the model was deliberately initialized by setting only one first mode ISW propagating westward from the deep part of the ocean assuming its generation not far from the LS. This is in accordance with satellite images in the sense that mostly only one single ISW (not a packet) exists in the deep water and that the location of the initial wave in the model corresponds to the earliest appearance of ISWs on SAR images (Zhao et al. 2004). A tricky step of the model initialization was to set up the initial incoming wave, and a similar approach as that in section 7.3 was used. Firstly, in a 2D configuration of constant depth (3000 m), a KdV solution of a first mode depression wave was substituted into the MITgcm, which evolved towards a new steady state. After getting fully detached from the structures behind it, this newborn ISW was truncated and used as an initial condition in the 3D case later. Secondly, the truncated 2D ISW was extended meridionally within the 3D model domain but still with constant water depth (3000 m), and this 3D ISW with straight wavefront was placed in the middle east of the domain. Sharp edges were formed on the two ends, leading to some swirl-like motions nearby, and energy gradually leaked sideways. The experiment on 3D evolution of initially 2D ISW in a basin of constant depth continued until all the transient processes decayed and the 3D ISW took the curved shape like that shown in Figure 8.2. This curved ISW is similar to the wave signatures shown on SAR images (Figure 1.3). It is the strongest in the center with the amplitude of 140 m yet decreases monotonically sideways to the north and the south. This ISW was used in the numerical experiments on 3D shoaling over realistic bottom topography (Figure 8.1).

8.3 Three-dimensional simulation of internal solitary wave shoaling in the northern South China Sea

In this section, the shoaling process of an ISW is examined within a realistic 3D configuration. In the meantime, the rotational effects on ISW evolution are put forward. In the following

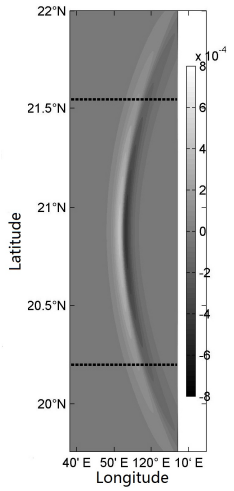

Figure 8.2: Initial condition for the model setup: sea surface zonal velocity gradient (s^{-1}) of the initial incoming ISW. The two dashed lines confine the initially straight ISW with sharp edges, which subsequently develops the backward curvature due to energy leakage sideways (see the text).

discussions, the sea surface zonal velocity gradient, which is an important parameter in SAR imagery (Alpers 1985), is taken as an indicator to trace the position of ISWs and investigate their spatial characteristics.

8.3.1 Initial stage of shoaling

Figure 8.3 is a compilation of sea surface signatures (sea surface zonal velocity gradient) of the leading ISWs at different stages. The corresponding time (in hours) is labeled along with each ISW. Three snapshots at t= 24, 34, and 48 h are the fragments from the model output, whereas the thick black lines show only the positions of the leading ISWs. The profile of the incoming ISW is not subjected to any substantial changes until it approaches the 1000 m isobath, where the topography starts to shoal drastically. As a consequence of the south-north asymmetry of the bathymetry, the southern periphery of the ISW travels faster due to larger water depth, hence the wavefront is deflected (compare profiles at t=20 and 24 h). At the same time, the northern part of the wave looks stronger than the southern counterpart due to the decreasing waveguide. Three-dimensionality is getting much more remarkable as the wave propagates up onto the slope. Wave refraction is visible near the Dongsha Atoll, where ISW splits into two parts which, however, merge again later behind the atoll. Wave reflection in all directions occur around the atoll (not shown). The impact of the underwater banks (shown by the triangles in Figure 8.3) is pronounced, particularly at t=34 h, when the wavefront splits into several fragments. Wave fission starts to develop in the shallow water, as is clearly seen at t=34 h. As time progresses, the disintegrated ISWs are stretched due to nonlinear dispersion (compare wave fragments at t=34 and 48 h). Subsequent evolution of sea surface signals in the shallow water will be discussed later.

To inspect the corresponding underwater wave structures, two cross-sections in Figure 8.3 ($21.5°N$ and $20.4°N$; see the two solid lines) were chosen. Four snapshots (t=16, 24, 34, and 48 h) for every cross-section shown in Figure 8.4 illustrate the evolution of the vertical density and

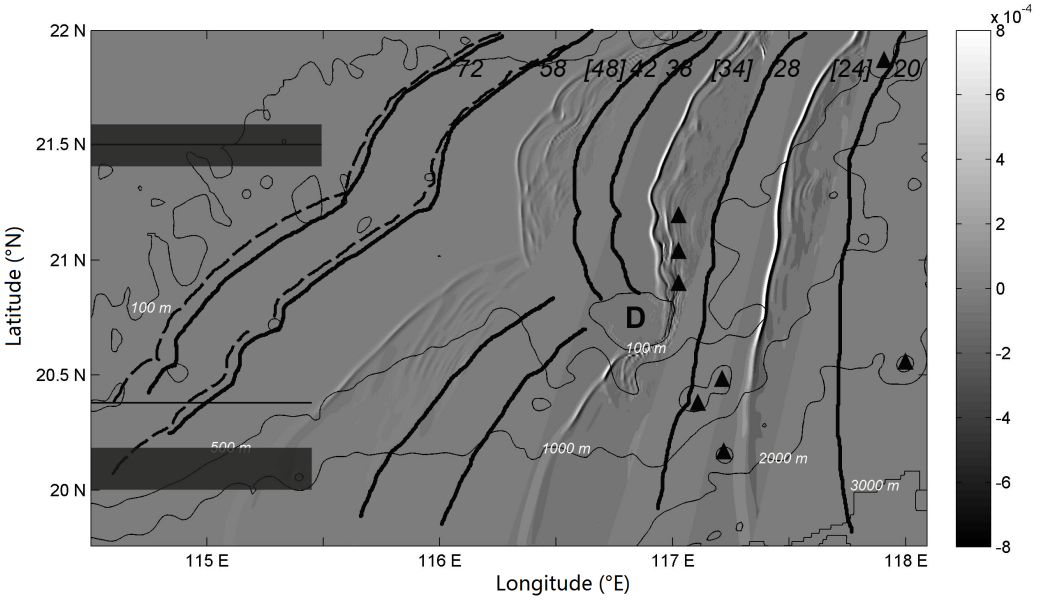

Figure 8.3: Compilation of the modeled sea surface velocity gradient overlapped on bathymetry (water depth of 100, 500, 1000, 2000, and 3000 m is shown) at different stages, with the time labeled accordingly. Three snapshots taken at t=24, 34, and 48 h are plotted straight from model results and the time labels are in the square brackets, whereas the bold solid lines are sketches of the leading waves at the other moments. Two bold dashed lines are sketches of the leading waves at t=58 h and t=72 h when rotation is switched off. The two thin lines along $21.5^{\circ}N$ and $20.4^{\circ}N$ (only the left parts are drawn to make the figure more readable) are chosen to illustrate the evolution of density and velocity fields in the vertical direction, as will be shown in Figure 8.4. The two grey rectangles mark two averaged topography that will be used in section 8.5. The triangles in the figure mark the approximate location of the underwater banks, whilst 'D' denotes the Dongsha Atoll.

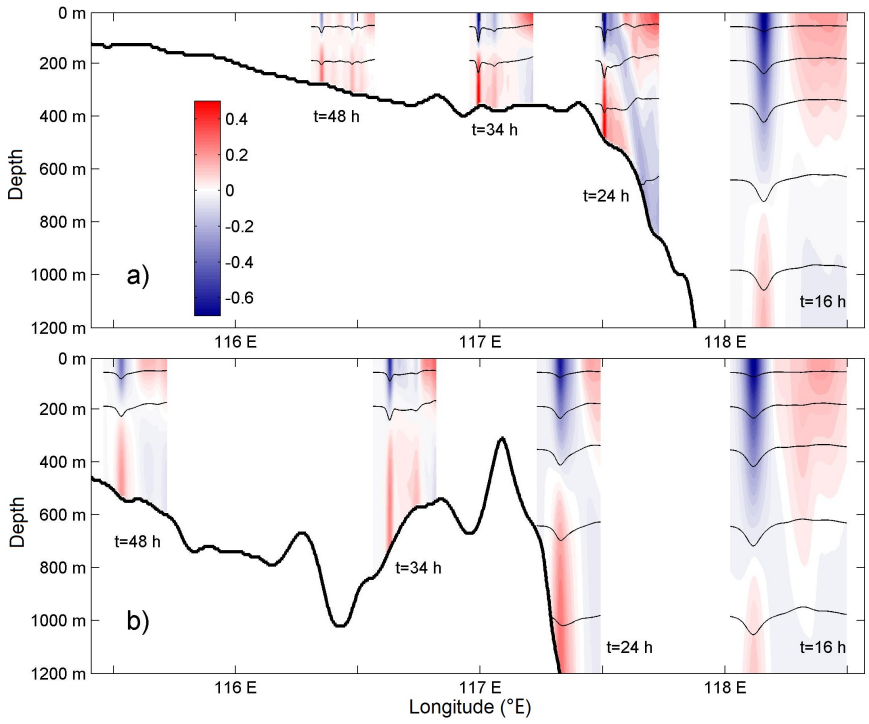

Figure 8.4: Vertical structures of density and velocity along the two cross-sections shown in Figure 8.3. Panels a and b correspond to cross-sections 21.5°N and 20.4°N, respectively. Four instants at t=16, 24, 34, and 48 h are shown for both cross-sections, with the last three instants corresponding to the three realistic model outputs in Figure 8.3. The plotted isopycnals are, from top to bottom, 1023, 1025, 1026, 1027, and 1027.5 kg/m^3, respectively.

velocity fields. The northern cross-section (panel a), which features steep yet smooth change of topography, is more effective in scattering wave energy. Wave amplitude at t=16 h (80 m) has decreased moderately from the initial 100 m along this cross-section, whereas it drops more quickly to 60 m after traveling onto the shelf (t=34 h) and to only 20 m further up (t=48 h). Transformation on the slope is drastic, with the detailed process shown in Figure 8.5. In panel a (t=20 h), wave profile reveals asymmetry, with the frontal side steeper whilst the rear gentler. A secondary wave, though still weak, is shed backwards and trails the main wave. This wave continuously grows, and at t=28 h, a clear wave of elevation is seen behind the leading ISW. On the other hand, the amplitude of the leading ISW keeps decreasing during this process and the wave itself gradually transforms into two waves after going onto the shelf, as is shown in Figures 8.3 and 8.4a (t=48 h).

The southern cross-section in Figure 8.3, which features an underwater bank with the depth of about 300 m, exhibits different scenario in wave evolution, as is shown in Figure 8.4b. Wave profile transformation is not significant until it gets close to the bank, over which the incoming wave amplitude decreases from 60 m at t=24 h to 50 m at t=34 h. Despite the slight decrease of the wave amplitude after the collision with the bank, the transmitted wave, which is as yet non-stationary, is much narrower, implying the loss of wave energy and the occurrence of localized wave scattering and energy transfer at the bank. The detailed interaction process between these

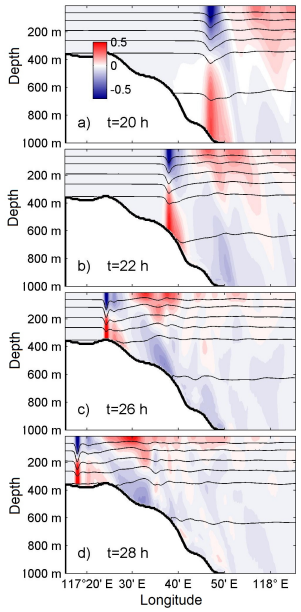

Figure 8.5: Evolution of vertical density and velocity fields near the shelf break along cross-section 21.5°*N* (Figure 8.4a). Time instants of 20, 22, 26, and 28 h are shown. The plotted isopycnals are, from top to bottom, 1023, 1024.2, 1025, 1025.5, 1026, and 1027 kg/m^3, respectively.

two moments is shown in Figure 8.6 with a time interval of two hours. Just as the scenario in the northern cross-section, the incoming wave also goes through an asymmetrical deformation but with a faster pace (panel a of Figure 8.6). A pronounced ray structure is formed as well near the bank top during the wave passage and it continuously evolves. After the detachment of the ISW from the bank, the beam structure starts to attenuate, gradually transforming into a series of high mode waves (panels c and d). After passing over the bank, the incident ISW exhibits a tendency to fission (Figure 8.6c). Overall, the southern portion of the wave is weaker and even indistinguishable in the sea surface signal field (see Figure 8.3), which is consistent with the SAR observations (Figure 1.3).

8.3.2 Crossing the turning point

When further propagating into shallow water, it is known that a shoaling wave of depression often goes through polarity reversal. The point at which it reverses can be sought by considering the KdV equation (2.24). The sign of the nonlinear coefficient α determines the polarity of an ISW of first mode, with positive and negative values corresponding to waves of depression and elevation, respectively. With the summer stratification used in the model (Figure 1.6), the calculation of α above the northern SCS shelf indicates that its sign reverses from negative to positive at the depth of about 130 m (turning point), which implies that within weakly nonlinear scheme, theoretically the incoming waves of depression are supposed to transform into waves of elevation.

Figure 8.7 shows two scenarios of wave evolution over the shelf break. Here the sea surface velocity gradient in the shallow water at time t=60 and 76 h is presented. It corresponds to the moments when the leading wave is located before and after reaching the turning point at

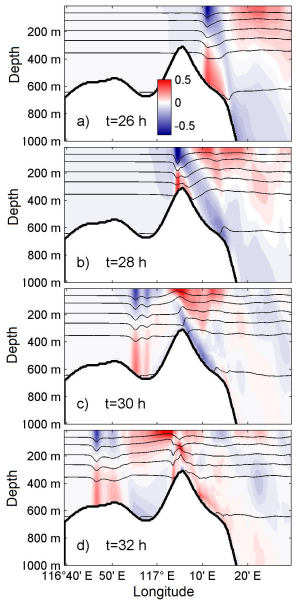

Figure 8.6: The same as Figure 8.5 but for the fields near the bank along cross-section 20.4°*N* (Figure 8.4b). Time instants of 26, 28, 30, and 32 h are shown.

the 130 m isobath, respectively. The two snapshots are separated in Figure 8.7 by the white stripe. The blocking effects of the underwater banks are pronounced, as can be seen at t=60 h, when the leading wave is segmented into several fragments and is thus spatially intermittent. In general, at this moment the wavefront features a blue stripe followed by a red stripe, except in the northern part where it intersects the 130 m isobath (turning point) and the wave features a red stripe followed by a blue stripe, clearly a manifestation of elevation waves. Meanwhile, a secondary wave train with multiple waves is clearly shown. Its surface manifestation is even stronger than the frontal ISW packet, and it turns up only in the northern half of the slope-shelf area where the shoaling topography is more steep, whereas in the southern half it is much weaker. This secondary wave train first emerges above the shelf break at t=34 h. Its structure and generation process will be scrutinized in the next section. In the next snapshot at t=76 h, when the leading wave has mostly crossed the 130 m isobath (the secondary wave train is not shown at this moment), the surface signature is basically visible as red/blue stripes on the sea surface, denoting the complete emergence of elevation waves. Also, ISW disintegration at this moment is more pronounced than at the previous moment, and several waves can be seen in the packet. Note that the sea surface signatures at this stage are much weaker than those before approaching the shelf break (see the color bar scale in Figure 8.7), and thus cannot be readily distinguished on SAR images.

Bathymetry is one of the key factors controlling the wave shoaling process. In the shelf-slope area of the northern SCS it is fairly corrugated (Figure 8.1), which influences the local wave characteristics. When scrutinizing the evolution of the vertical structures of the leading ISW packet in the across-shelf direction in Figure 8.7, wave broadening and polarity reversal occur (figures not shown). One should note that, as was previously described in section 8.1, only a small portion of the incoming wave energy from the LS is dissipated locally in the shallow water, whereas the majority is lost above the slope and the shelf break, especially in the area

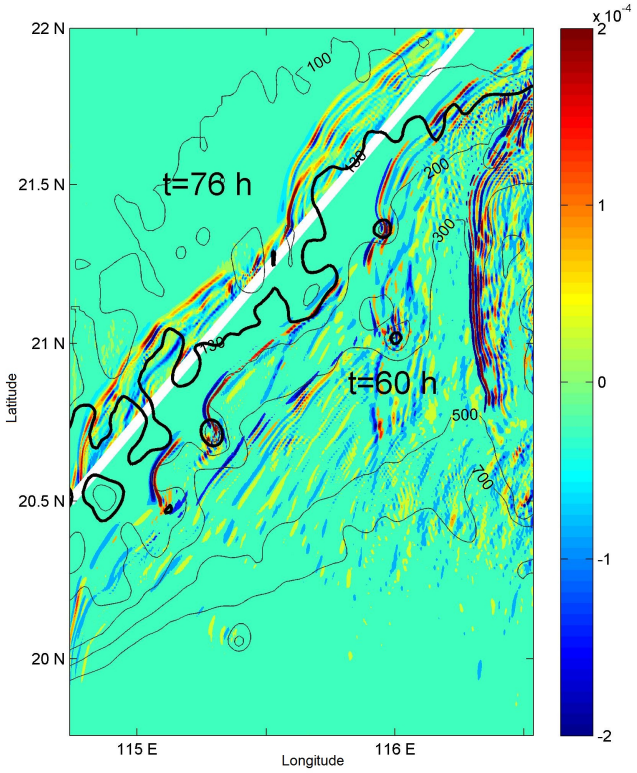

Figure 8.7: Sea surface velocity gradient plotted as blue and red stripes at t=60 h (lower right) and t=76 h (upper left) in the shallow water, with the white band separating the two snapshots. Bathymetry is overlapped, with the 130 m isobath plotted in bold.

around the Dongsha Atoll.

8.3.3 A discussion of horizontal resolution

The above 3D experiment was conducted with a horizontal resolution (Δx) equal to 100 m. It is known that discretization of the hydrodynamic equations can introduce numerical dispersion that competes with physical dispersion. According to Vitousek & Fringer (2011), for a continuous stratification, the measure of the ratio of numerical to physical dispersion (Γ) can be written as:

$$\Gamma = K\lambda^2 = K(\frac{\Delta x}{h_e})^2 \tag{8.1}$$

where K is an $O(1)$ constant; $\lambda = \frac{\Delta x}{h_e}$ is the grid leptic ratio; h_e is a depth scale and is expressed as:

$$h_e = \sqrt{\frac{3\int_{-H}^{0}\Phi^2 dz}{\int_{-H}^{0}(\frac{\partial\Phi}{\partial z})^2 dz}} \tag{8.2}$$

where H is the water depth, and $\Phi = \Phi(z)$ is the vertical eigen-function. In numerical simulations of internal waves, $\Gamma << O(1)$ is desired, since this implies that spurious numerical dispersion is minute compared to the realistic physical dispersion, whereas for the opposite case, $\Gamma >> O(1)$, wave dispersion will be seriously contaminated by numerical dispersion, which certainly jeopardizes the accuracy of the modelling results.

For the case of the northern SCS, a Γ versus H graph is plotted in Figure 8.8 for $\Delta x = 100,\ 250\ m$. It is seen from the graph that for $\Delta x = 250\ m$, $\Gamma << O(1)$ occurs only at $H > 1000\ m$, and at $H = 500\ m$, numerical dispersion is almost comparable with physical dispersion. Shallower than 500 m the model results are overwhelmed with spurious numerical dispersion. However, when $\Delta x = 100\ m$, $\Gamma << O(1)$ before the wave reaches the depth of 500 m, and numerical dispersion is considered minor. However, upon approaching $H = 300\ m$, Γ increases to 0.44, which implies that numerical dispersion has come into play, but the latter still dominates. Further shallower, Γ increases sharply, indicating the dominance of numerical dispersion over physical dispersion.

Figure 8.8 illustrates the insufficiency of a 250 m resolution in delineating wave evolution in the shallow water. However, due to the massive demand of computational power and the subsequent data analysis for the output, it is very difficult to further enhance the horizontal resolution. Nevertheless, it will be proved later that the 250 m case still grasps the main features of wave evolution, only that it produces a bit smaller wave amplitude and less waves. Hence, the above 3D results in the shallow water should be treated more in a qualitative way. This issue will be re-visited later in the next section.

On the other hand, the formation of an intriguing secondary wave train in Figure 8.7 was only briefly mentioned and it merits more insight. This wave train shows up only in the northern portion of the slope-shelf area, and nearly vanishes when rotation is switched off in the run. It comprises of multiple short waves that are unlikely to be well resolved in the 3D runs. To inspect its generation process and mechanism, a series of high-resolution 2D experiments was conducted to elucidate the effects that rotation has on the evolution of shoaling ISWs.

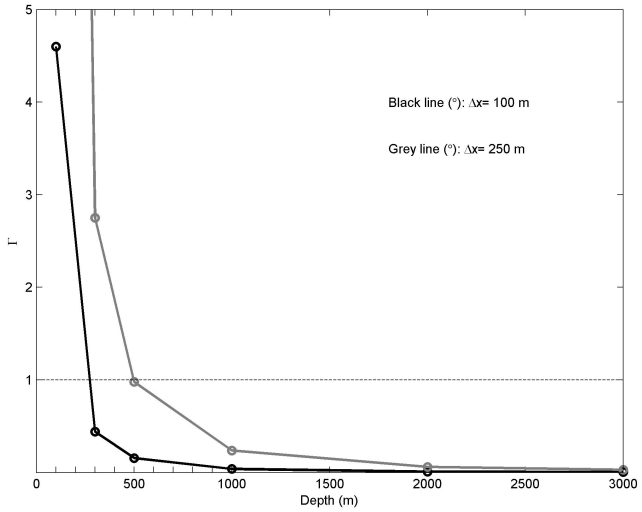

Figure 8.8: Γ (see the text) versus depth in the northern SCS. Values of Γ were calculated at depths of 100, 300, 500, 1000, 2000, and 3000 m (see the circles) for the horizontal resolutions (Δx) of 100 m (black line) and 250 m (grey line).

8.4 The rotational effects on ISWs in the northern SCS: constant depth

Before discussing the influence of rotation on a shoaling ISW, it would be reasonable to first examine the rotational effects only, i.e., in a basin of constant depth.

According to Leonov (1981), stationary localized ISW solutions of the rotation-modified KdV equation cannot exist. However, Gilman et al. (1996) found that non-stationary ISWs can co-exist with long, smooth background waves of small amplitude, whereas in the other regime, Gilman et al. (1996) showed that an inital KdV-type ISW can completely annihilate within a finite time by constantly shedding long tails, which can steepen and give birth to a new ISW with nearly identical parameters to the original ISW, and this process repeats quasi-periodically. Grimshaw et al. (1998) also investigated the decaying process of an initial ISW with an asymptotic procedure. It was found that the amplitude (η) of the evolving ISW decays with time (t) as (Grimshaw et al. 1998, Helfrich 2007):

$$\frac{\eta}{\eta_0} = (1 - \frac{t}{t_d})^2 \tag{8.3}$$

where η_0 is the amplitude of the initial ISW, and t_d is the scale of the terminal damping time, which was estimated by Helfrich (2007) as 1-4 days for oceanic conditions.

Using a fully nonlinear, weakly nonhydrostatic two-layered model with rotation, Helfrich (2007) discovered a novel scenario of ISW evolution: in rotational systems, a propagating ISW keeps shedding inertia-gravity waves, which always steepen and form a secondary ISW due to nonlinear effects; such a decay and re-emergence process repeatedly occurs and ultimately a nearly localized wave packet, which consists of a long-wave envelope (lengthscale of L_R) through which solitary-like waves propagate, emerges. Such a process was further scrutinized and corroborated by Stastna et al. (2009), who solved the rotating stratified Euler equations, and by Grimshaw & Helfrich (2012), who illustrated with a combination of asymptotic theory, numer-

ical simulations, and laboratory experiments. On the other hand, Grimshaw & Helfrich (2008) numerically solved the Ostrovsky equation (Ostrovsky 1978) which includes rotation into the KdV equation, and presented different scenarios based on the non-dimensionalized amplitude of the initial ISW and found that, in all the cases considered, a leading wave packet emerges, but for relatively small initial waves, the packet could not completely separate from the trailing radiated waves, whereas for large initial waves the separation is clear.

Note that the earliest appearance of ISWs in the northern SCS is located somewhere near $120°30'E$ (Figure 1.3). L_R is estimated as about 54 km at the latitude of this region, and given the long distance between $120°30'E$ and the continental shelf on the propagation routes of the ISWs, which is about several hundreds kilometers, the impacts of rotation on ISW propagation are expected to be significant. Nevertheless, despite the intriguing finding by Helfrich (2007), the assumption of a weak nonhydrostaticity and two-layer stratification of the ocean can restrict the generality of these conclusions. Here, in application to the deep part of the northern SCS, it would be instructive to first investigate the rotational effects. To this end, a series of 2D experiments with constant water depth was first conducted.

Figure 8.9 shows the evolution of an ISW with an initial amplitude of 90 m and a depth of 3000 m at the latitude of about $21° N$ (condition of the northern SCS). The plotted lines $\eta(x,t)$ are shown in a coordinate system moving with the linear long wave phase speed (estimated as 2.74 m/s in this case). The time interval between two successive profiles is equal to eight hours. The impact of rotation on the ISW evolution can be clearly seen from the figure. The rear of the ISW is humped at t=22 h (Figure 8.9b), commencing the radiation of inertia-gravity waves backwards. The radiated waves keep draining energy from the frontal ISW and grow in amplitude (t=56 h). Meanwhile, the ever-growing inertia-gravity wave itself steepens and gradually forms a solitary-like wave whose amplitude, at t=86 h, has exceeded the leading ISW, which has been greatly decayed by that time. This initial stage of ISW decaying is compared against the weakly nonlinear theory (8.3), and is shown in Figure 8.10. It can be seen that before the return process, i.e., the emergence of the second solitary-like wave around 80 h, the two lines nearly coincide completely, which implies that weakly nonlinear theory can be reasonably applied for the prediction of the decay process of the initial leading ISW. However, apparently it is incapable of delineating the return process of the wave evolution.

As time goes, the steepened secondary wave at t=86 h is progressively shaped and also sheds energy backwards, just like its predecessor, which, as is shown in Figure 8.9b, has almost diminished at t=146 h. Such a decay-return process is, to a large extent, what Helfrich (2007) has predicted. The only difference is that the inertial gravity waves are continuously shed from the frontal ISW envelope, and their number is growing as time progresses, although nonlinearity is not strong enough for them to evolve towards ISWs. The inertia-gravity waves drain energy from the frontal ISW packet and as a consequence, the maximum isopycnal displacement in the packet constantly decreases until it can hardly be resolved by the model resolution (Figure 8.10). This feature is quite in contrast with the scenario of Helfrich (2007), which exhibits very weak energy leakage and eventually a status of almost localized wave envelope with temporal periodicity is reached. Such a discrepancy is likely to be attributed to be the assumption of weak/full nonhydrostaticity in these two models. The nonhydrostatic dispersion $(H/l)^2$, turns out to be not small for ISWs in the northern SCS when taking H=3 km and l equal to several kilometers (see Figure 4.3a). Nonhydrostatic effects tend to disperse the ISW, thus much stronger draining of energy from the frontal ISW packet is encountered in the circumstances of

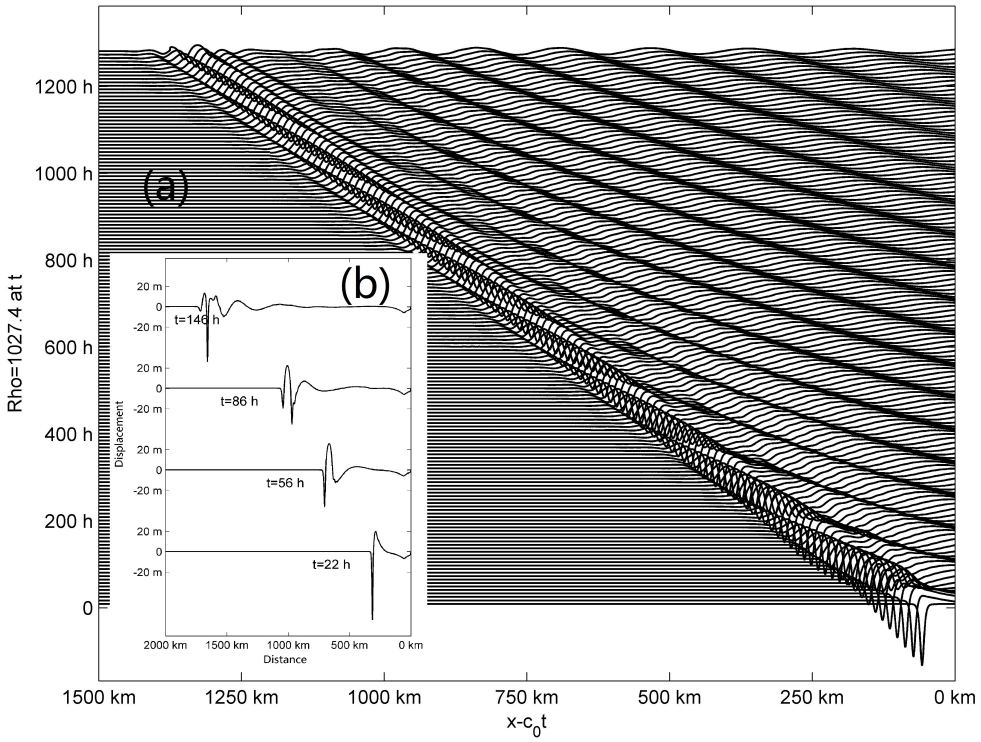

Figure 8.9: a) 2D evolution of an ISW with amplitude of 90 m under the effects of rotation. The isopycnal of $\rho = 1027.4\ kg/m^3$, which is located at 900 m when at rest, is shown at an equal time interval of 8 hours in a frame moving with the linear phase speed $c_0 = -2.74\ m/s$, where minus denotes ISW that propagates westward; b) ISW profile shown at four time slices: t=22, 56, 86, and 146 h.

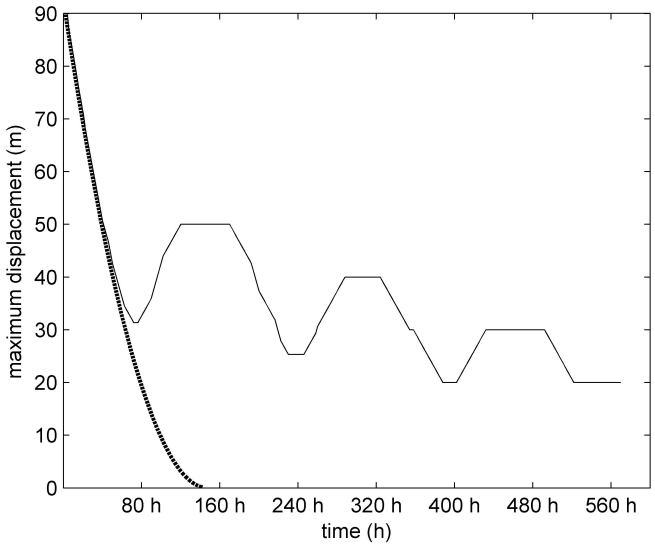

Figure 8.10: Time evolution of the maximum displacement of the ISW shown in Figure 8.9a (thin line); the superimposed dashed line is the corresponding amplitude decay solved from weakly nonlinear theory.

the northern SCS where nonhydrostaticity is not weak.

On the other hand, to compare with the scenarios obtained by Grimshaw & Helfrich (2008), an estimation of an M parameter was conducted. It is expressed as

$$M = \frac{\lambda}{\nu L^2} \tag{8.4}$$

where $L^4 = \sqrt{\lambda/\gamma}$; ν, λ, and γ are respectively coefficients of nonlinearity, dispersion, and rotation in the Ostrovsky equation (under Boussinesq approximation):

$$\nu = \frac{3}{2} c \frac{\int (d\Phi/dz)^3 dz}{\int (d\Phi/dz)^2 dz} \tag{8.5}$$

$$\lambda = \frac{1}{2} c \frac{\int \Phi^2 dz}{\int (d\Phi/dz)^2 dz} \tag{8.6}$$

$$\gamma = \frac{f^2}{2c} \tag{8.7}$$

where the wave phase speed c and Φ can be sought by solving the eigenvalue problem; f is the Coriolis frequency. For the continuous summer stratification in the northern SCS (as shown in Figure 1.6) with a water depth of 3000 m, the above coefficients have the values of:

$c = 3.12\ ms^{-1}$;

$\nu = -0.005\ s^{-1}$;

$\lambda = 1.1 \times 10^6\ m^3 s^{-1}$;

$\gamma = 4 \times 10^{-4}\ m^{-1} s^{-1}$ ($f = 5 \times 10^{-5}\ s^{-1}$ is used).

This M parameter non-dimensionalizes the wave amplitude in the calculations of Grimshaw & Helfrich (2008). With the estimated coefficients listed above, M is calculated to be equal to 4.2 m, thus the obtained non-dimensional amplitude for an ISW of 90 m is $90/4.2 \approx 21$, which, according to Grimshaw & Helfrich (2008), should give rise to a regime where a leading wave packet quickly separates from the trailing waves behind. However, it is clear from Figure 8.9 that this is not the case, i.e., the continuously decaying leading packet cannot detach from behind at all, which proves the incompetence of weakly nonlinear, weakly nonhydrostatic theories in delineating large ISWs with not weak nonhydrostaticity in this case.

Note that the longevity of the waves shown in Figure 8.9a (about 1300 h) is purely for the interest of investigating rotational effects on ISWs and is unrealistic in the northern SCS. The distance of the leading wave at t=22 h in Figure 8.9b from the initial wave denotes the traveling range of the wave from $120°30'E$, where ISWs first appear, to about $118°E$, where the deep water transits to the continental slope. It is readily seen from the figure that minor profile change is predicted and the initial ISW decay is deemed to be weak, which implies that for ISWs traveling across the SCS deep basin, the rotational dispersion does not play a very significant role. On the other hand, when further progressing westward onto the shelf break and shallow water, ISWs are subject to very strong topographic effects. This renders the role of rotation indistinct, although Figure 8.9b (t=56 h) does show that without topography change the initial ISW has decayed a lot when reaching the western boundary of the northern SCS.

To assess the effects of rotation on ISWs in the shallow water, an experiment with constant water depth of 500 m and with initial ISW amplitude of 50 m was configured and the results are shown in Figure 8.11. It is apparent that the change of the wave profile and the associated long wave radiation are less abrupt due to weaker nonlinearity in this case. However, the rotational effects are no less significant. If the northern SCS slope and shelf are roughly treated as from $118°E$ to $116°E$ and with constant depth of 500 m, when traveling through this distance, the initial ISW amplitude decreases mildly to 40 m after about 40 hours, compared to from 90 m to 70 m in Figure 8.9 across the same distance.

The above discussion revealed the influence of rotation for the evolution of ISWs both in the deep and shallow water with constant depth. By switching on topography, the combined effect of shoaling topography and rotation is illustrated below.

8.5 The rotational effects on ISWs in the northern SCS: variable depth

Given that 3D calculations on a fine-resolution grid are not always computationally feasible, a series of 2D experiments was conducted to study the interesting scenarios (mainly the formation of a secondary wave train) revealed in the 3D experiments discussed above. To this end, two cross-sections with averaged topography, the northern cross-section (averaged between 21.4° and 21.6° N) and the southern cross-section (averaged between 20° and 20.2° N), were chosen. The averaged profiles are shown in Figure 8.12. The two cross-sections are representative of the topography in this area: the northern one features a drastic change of slope, whereas the southern one is similarly steep in the deep part, but the shelf break is much deeper (1000 m). It then features a smooth change of topography, followed by a second slope and shelf break. The southern cross-section is overall deeper than the northern one.

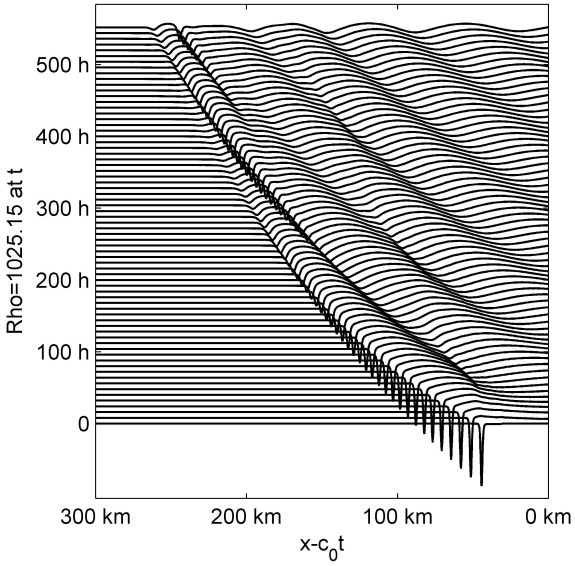

Figure 8.11: The same as Figure 8.9a but with water depth of 500 m, initial ISW amplitude of 50 m, and c_0 of $-1.4\ m/s$. The shown isopycnal is $\rho = 1025.15\ kg/m^3$, which is located at 210 m when at rest.

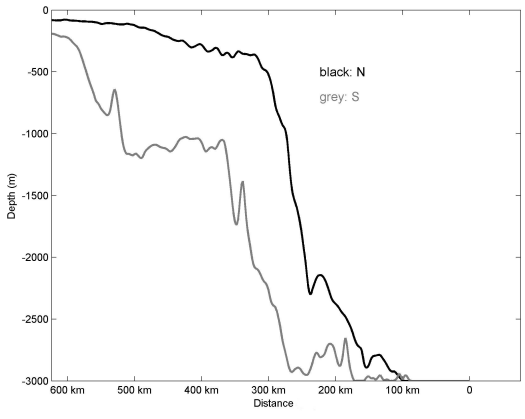

Figure 8.12: Two sets of averaged topography used in the 2D experiments: the northern cross-section (black line; averaged between 21.4° and 21.6° *N*) and the southern cross-section (grey line; averaged between 20° and 20.2° *N*). The positions of the two cross-sections are also indicated in Figure 8.3.

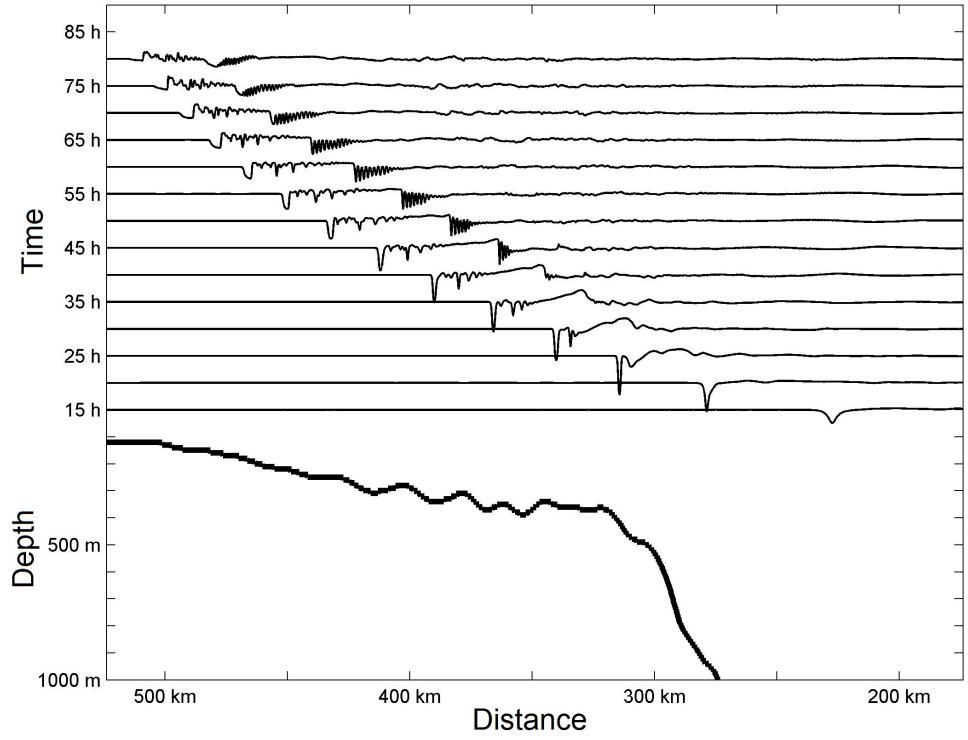

Figure 8.13: 2D evolution of an ISW with amplitude of 90 m under the effects of rotation along the northern cross-section. The isopycnal of $\rho = 1024\ kg/m^3$, which is located at 100 m when at rest, is shown at an equal time interval of 5 hours. The shown isopycnals start from t=15 h when the ISW approaches the shelf break. The lowest thick line is the topography in the upper 1000 m, with the 0 m depth at the position of '15 h'. The y-axis for the topography also measures the scale of the displacement of the plotted isopycnals.

Model setup is the same as that in section 8.2, except that the topography is variable. Figure 8.13 shows the evolution process of the shoaling wave. Scrutinizing the figure one can see a striking new feature of the wave evolution that has not been reported before, that is, the joint effect of rotation and variable topography leads to the formation of a secondary wave train with a number of short, rank-ordered waves (solibore). The incoming ISW from deep water experiences severe deformation when passing through the shelf break, with the radiation of secondary waves. The leading ISW is progressively shaped by the changing environment, with a decreasing of amplitude and commencement of wave fission. The distances between the fissioned ISWs are enlarged due to nonlinear dispersion. The broadening and subsequent polarity reversal of the leading ISW occur after t=60 h when the leading wave is located above the depth of about 130 m.

It was shown above that an interesting finding of the present runs is the generation of a secondary solibore, which is possible due to the joint effect of rotation and joint topography. According to Figure 8.13, accompanying with the reshaping of the leading ISW near the shelf break (t=25 h), somewhere behind it the isopycnal is somehow elevated and quickly steepens and disintegrates

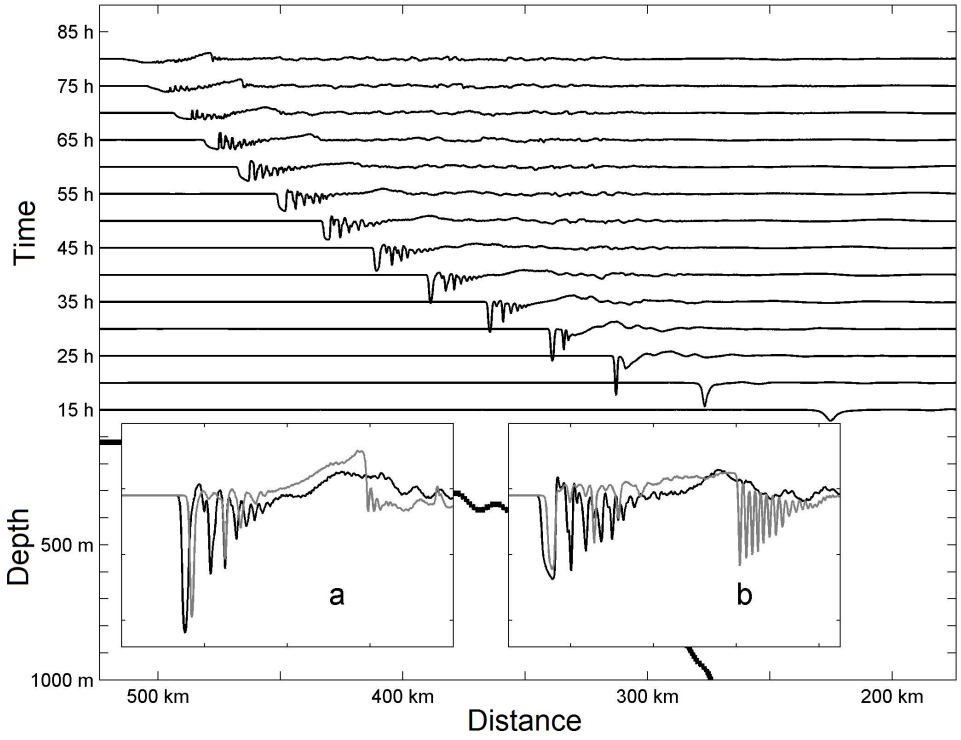

Figure 8.14: The same with Figure 8.13 except that rotation is switched off. The two insets display the comparison of the isopycnals with (grey) and without (black) rotation at t=40 h (inset a) and 55 h (inset b).

into a wave train with increasing number of waves, i.e., a solibore. The first wave of the solibore also broadens and exhibits a scenario of polarity reversal when further traveling up onto the shallow water. Behind the solibore are some high modes which are generated due to nonlinear scattering of wave energy into the ambient modes.

To test and verify whether it is rotation that causes the formation of such a solibore, the very same experiment but without rotation was performed, and the results are shown in Figure 8.14. It is seen from the figure that, at t=25 h, the elevation also emerges behind the incoming ISW, but it is less strong than that in Figure 8.13 at the same moment of time. However, unlike the rotational case, this elevation does not steepen into a solibore. Instead, it gets increasingly smooth until it reaches the very shallow water where it reveals a slight tendency of steepening (t=75 h). Meanwhile, for the initial incoming ISW, it goes through similar transformation process, but with larger wave amplitude and more fissioned waves. A comparison of two scenarios (t=40 h and 55 h) with and without rotation is shown in the two insets of Figure 8.14, and the contrast is immediately apparent.

The conclusion that can be drawn from the above comparison is that it is rotation that engenders the formation of the secondary wave train. Recall from Figure 8.9b that, without topography (i.e., with a constant depth of 3000 m), the ISW profile has only changed slightly after traveling through the deep basin (t=22 h in Figure 8.9b), but further west near the western boundary of

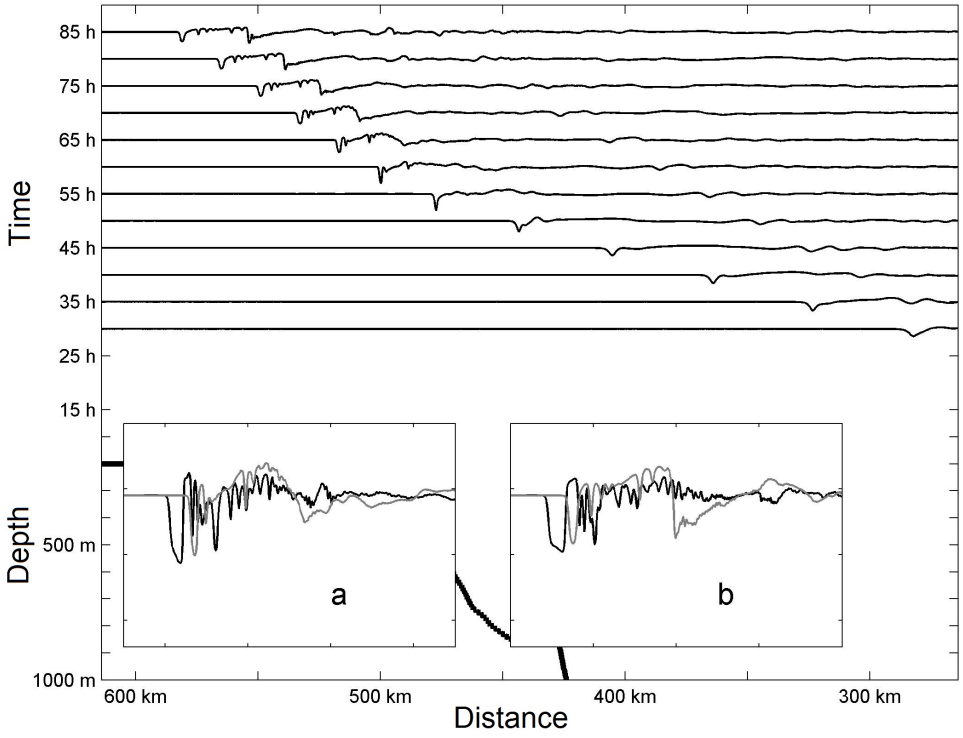

Figure 8.15: The same with Figure 8.13 except that it is for the southern cross-section. The two insets display the comparison of the isopycnals with (grey) and without (black) rotation at t=65 h (inset a) and 75 h (inset b).

the studying area (t=56 h in Figure 8.9b), the initial ISW has radiated a long (about 200 km) inertia-gravity wave. When topography is implemented into the model, the long inertia-gravity wave steepens quickly upon reaching the abruptly shoaling topography and produces a solibore which is of different nature to the wave packet that is formed due to the shoaling of the initial incoming ISW. In brief, the combined effect of shoaling topography and rotation leads to the emergence of two separate wave packets of different kind from only one incoming ISW, which contrasts with previous studies on ISW evolution that usually simulated only one packet upon shoaling process.

As for the southern cross-section, a more or less similar scenario is seen in Figure 8.15. However, in this case the main shelf break is deeper and is situated nearly 200 km west of the shelf break of the northern cross-section. As a result of that, the secondary solibore emerges much later and further west in this area. Meanwhile, the solibore is much less significant than that in the northern cross-section. Comparing with the non-rotational case, one can see that without rotation (insets in Figure 8.15) the secondary solibore does not show up and the initial ISW is larger at all stages. One should notice from Figures 8.13 and 8.15 that a moderately sloped topography will not necessarily generate a secondary wave train; an abruptly changing shallow shelf break is required for that.

The appearance of a secondary wave train implies that one initial incoming ISW can lead to the

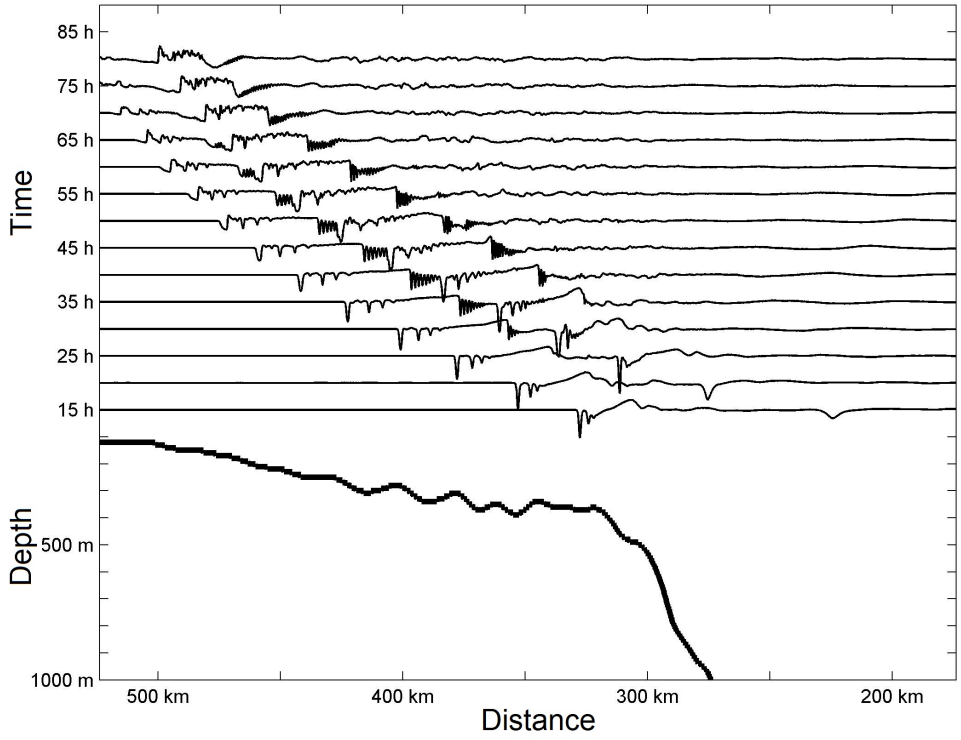

Figure 8.16: The same with Figure 8.13 except that there are two incoming ISWs that are set one M_2 wavelength (150 km) apart.

generation of two wave packets above the shelf break. An interesting question arises, given that two ISWs in the deep SCS basin are separated apart by the M_2 wavelength, what will happen if such two ISWs are set up in the model? Will there be four packets emerging eventually further up the shelf break? To check it out, a run was configured with two ISWs: with rotation, when an ISW has propagated an M_2 wavelength (150 km), the other ISW was implemented into the model at where the first ISW was initially located; the other setups were the same with that in Figure 8.13. The results are shown in Figure 8.16. It can be seen that due to the relatively slower propagation speed of the secondary solibore that was generated by the first incoming ISW, it is overtaken very quickly by the first ISW packet of the second incoming ISW upon passing the shelf break. These two wave structures interact with each other and are nonlinearly coupled until propagating into shallow water where the coupled wave structure gradually vanishes. Essentially, the combined wave structure is actually the superposition of a secondary solibore formed by an incoming ISW and an ISW packet that intrudes one tidal cycle later. It behaves as a cluster of dense spikes when plotting the surface velocity gradient, and thus could explain the abundance of wave trains up the shelf break on SAR images.

Getting back to Figure 8.8, one is reminded that spatial discretization can introduce spurious numerical dispersion that contaminates the modelling results. However, how significantly it contributes to the simulation remains unclear. Figure 8.17 shows four wave profile scenarios calculated with $\Delta x = 100,\ 250$, and 1000 m. It can be seen that the insufficiency of 1000 m

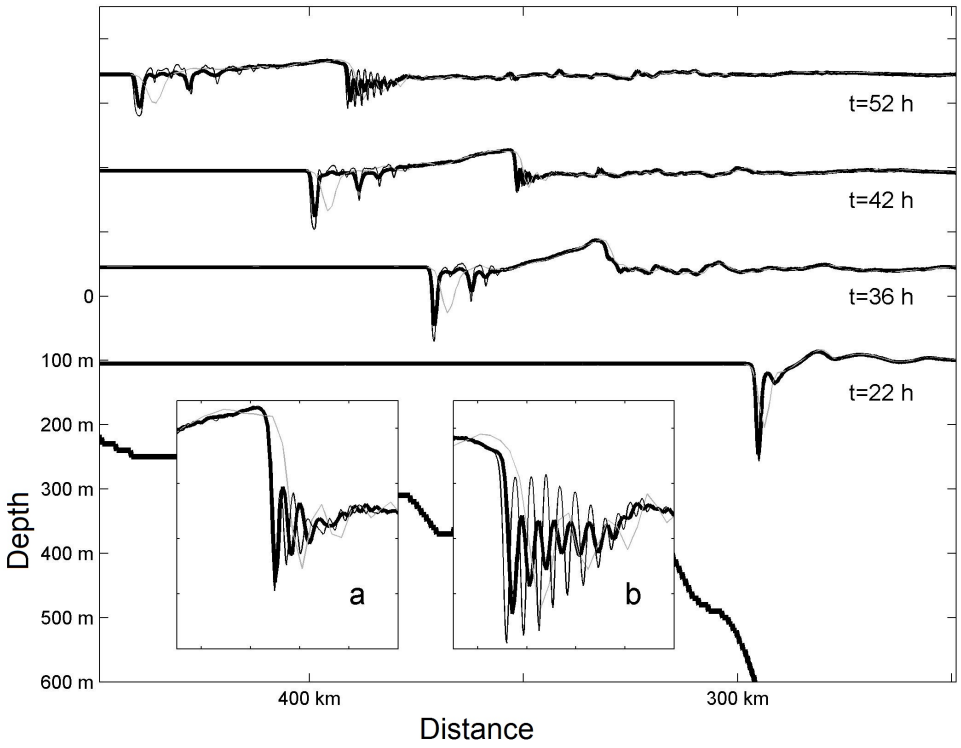

Figure 8.17: Sensitivity of the wave evolution on the horizontal resolutions (Δx): 100 m (thick black line), 250 m (thin black line), and 1000 m (thin grey line). Isopycnal of $\rho = 1024\ kg/m^3$ at four snapshots (from bottom to top: t=22, 36, 42, and 52 h) along the northern cross-section is shown. The two insets display the close-up views of the secondary wave train at t=42 h (inset a) and 52 h (inset b).

(Δy in the 3D experiments) resolution is apparent. It results in wider and smaller waves and can reproduce neither the evolution of the initial ISW nor the secondary wave train. But for $\Delta x = 100,\ 250\ m$, the discrepancy is much less significant. Wave profile for $\Delta x = 250\ m$ almost completely coincides with the profile for $\Delta x = 100\ m$ before approaching the shelf break, whereas upon arriving at the shallow water, the leading ISW is smaller and wave fission is weaker for $\Delta x = 250\ m$. As for the secondary solibore, there is little difference in the initial stage of wave elevation and disintegration (t=36, 42 h), but as time progresses and topography shoals, the discrepancy is obvious: wave disintegration is more pronounced when $\Delta x = 100\ m$, and the disintegrated waves are larger, narrower and have more number. According to the previous analysis of the value Γ (Figure 8.8), the waves have suffered overwhelming numerical dispersion at this stage when $\Delta x = 250\ m$, but the general features of wave evolution remain essentially unchanged (Figure 8.17).

Hence, for the 3D experiments in section 8.3, it should be noted that model predictions is quantitatively correct only at depths deeper than 1000 m. Shallower than that spurious numerical dispersion increases rapidly and it completely overwhelms physical dispersion at $H < 300\ m$. Nevertheless, for the incoming ISW (not the secondary solibore), the 250 m case still catches the main features of wave evolution when compared with that with 100 m resolution (even when

H equal to 220 m; see Figure 8.17), only that it reproduces a bit smaller wave amplitude. But for the secondary solibore, the discrepancy is larger, and it is especially pronounced at depths shallower than 350 m. So, the above 3D results should be treated more in a qualitative way but can still be deemed to be within a range of tolerable error in the shallow water. But for the secondary solibore, the error is much more significant, say, at $H < 350m$. On the other hand, making things worse is that Δy is as coarse as 1000 m. In the shallow water the wavefront has considerably rotated, which makes the resolution in y direction more important and thus jeopardizes the results.

The 2D experiments discussed above elucidate the principal idea of the paper, i.e., how rotation influences the shoaling of ISWs and the concomitant emergence of a secondary solibore. However, within the 3D configuration, one can consider the rotational influence in a more realistic context. Figure 8.3 schematically shows the plan view of the wave surface signature at two moments when rotation is absent (two dashed lines). The impact of rotation is straightforwardly seen from the comparison, and the discrepancy is larger further south. A comparison of the vertical profiles with and without rotation has been made and is shown in Figure 8.18. The eight panels in Figure 8.18 correspond to the eight profiles shown in Figure 8.4, viz., along two cross-sections and with four time slices taken for each cross-section. As expected and in agreement with the 2D experiment, rotational effects are weak in the deep basin. Specifically, panels d and h illustrate that the wave with rotation is slightly smaller in amplitude and propagates a bit more slowly due to the nonlinear dispersion. As a consequence of the backward radiation of long inertia-gravity waves, the isopycnals behind the leading wave are slightly elevated compared to the case without rotation. In the next instant above the steep topographic feature at t=24 h (panels c and g), the discrepancy between these two cases is much larger, even though the ISW has only traveled 68 and 83 km from the previous positions in the northern and southern cross-sections, respectively, which highlights the combined effect of topography and rotation. At this moment, the amplitude of the leading ISW with rotation is 25% and 33% smaller than its counterpart in the northern and southern cross-sections, respectively, compared to 13% and 20% in the previous instant (t=16h; panels d and h).

In the next moments above the shelf, the discrepancy is further augmented, with the attendant occurrence of wave disintegration. This is clearly seen at 48 h in panels a and e, especially in the latter, wave amplitude with rotation is more than twice smaller than that without rotation. Also notice that the distance between the two leading waves with and without rotation is longer in the southern cross-section (panel e) than that in the northern counterpart (panel a) due to larger amplitude and the resultant stronger nonlinear dispersion, which implies that without rotation the alignment of the wavefronts on the shelf would be spatially more oblique with respect to their original orientation when observing from the space.

Moreover, one thing worth mentioning is the contribution of rotation to the relative rarity of ISWs east of the LS in the broad western Pacific. As a consequence, the longevity of rotation can effectively damp the initial ISW formed somewhere close to the strait. However, this merits further investigation, since quite a few factors can bring about the lack of ISWs east of the LS (Buijsman, McWilliams & Jackson 2010).

8.6 Summary of the rotational effects on internal solitary wave shoaling

In contrast with the majority of investigations of internal wave generation in the northern SCS, the problem of wave shoaling phenomenon above the SCS slope and shelf has not been prop-

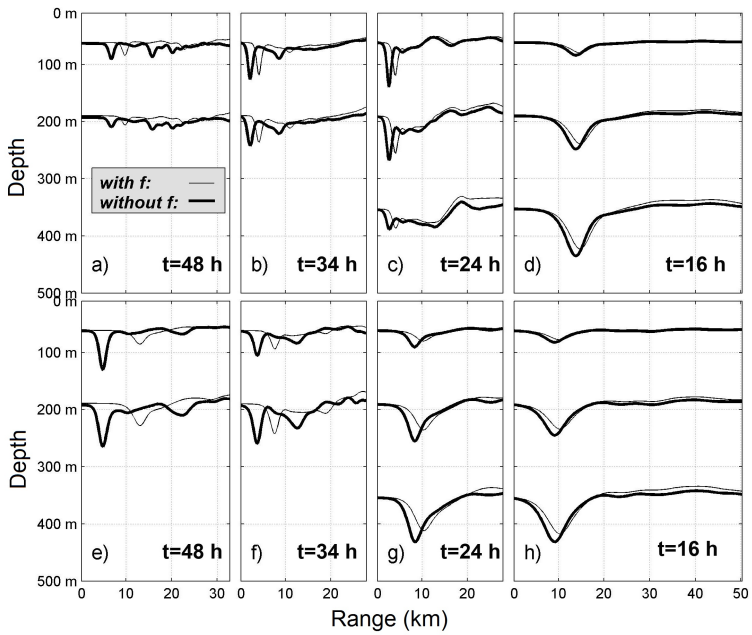

Figure 8.18: Comparison of the wave evolution profiles with (thin line) and without (thick line) rotation. The eight panels in the figure correspond exactly to the eight profiles in Figure 8.4; panels a-d and panels e-h correspond to Figures 8.4a and 8.4b, respectively; the time slices are, from right to left, 16, 24, 34 and 48 h. The plotted isopycnals in each panel are, from top to bottom, 1023, 1025, and 1026 kg/m^3, respectively.

erly addressed. Large amplitude baroclinic waves formed at LS travel across the deep basin, transform on the continental slope and shelf, and eventually dissipate in the shallow water. The intruding internal waves are the superposition of internal tides (diurnal and semidiurnal components) and ISWs. As a pilot numerical study, this chapter looks into the shoaling process of large amplitude first mode ISWs, which are the most striking features of the internal wave field in the northern SCS.

3D experiments were first performed with emphasis on the details of the evolution of wave profiles. It was found that the wave profile is subject to minor changes, mostly caused by the rotation, until it comes into contact with the shelf break, where severe wave deformation and disintegration take place. The Dongsha Atoll and some underwater banks play a key role in this process, especially in the area around the Dongsha Atoll, where the incoming ISWs diffract, reflect, and dissipate. The wavefront of the leading ISW is getting more spatially oblique with respect to their original orientation as it progresses westward due to the inclination of the slope in the topography. Wave disintegration is more prominent in the shallow water zone. Wave polarity reverses near the turning point (at the 130 m isobath), which is well consistent with the predictions of weakly nonlinear theory.

The selection of the horizontal resolution in the 3D experiments was discussed, and it was found that in the shallow water, a 250 m resolution is inadequate in delineating wave evolution in a quantitative way. However, given the massive demand of computational power, it is not quite realistic to further enhance the horizontal resolution. On the other hand, an intriguing secondary wave train with multiple short waves shows up in the 3D experiments. It was conjectured that it is rotation that mainly contributes to the formation of it. Given the unjustified 3D resolution and the flexibility of 2D models, to give more insight on the ISW evolution under the rotational effects, a series of 2D experiments was conducted.

It was found that under the rotational effects solely (with constant depth), an initial ISW constantly decays by shedding inertia-gravity waves backwards, in contrast with the results of Helfrich (2007), who presented a scenario of the formation of an eventual localized wave packet with little decay. Analysis of the magnitude of nonhydrostaticity shows that the treatment of weak/full nonhydrostatic effects is likely to cause such a discrepancy. The evolution of the leading ISW was compared with weakly nonlinear theory and a good agreement is reached. However, the eventual formation of a non-separated leading packet contrasts greatly with the Ostrovsky solutions (Grimshaw & Helfrich 2008), according to which a marked packet should quickly separate from the trailing waves.

Following the 2D experiments with constant depth, variable topography was implemented into the model and the combined effect of rotation and shoaling topography was scrutinized. It was shown that due to the joint effect of rotation and variable topography, the radiated inertial-gravity wave forms a pronounced elevation near the shelf break, which soon disintegrates into a wave train with increasing number of waves (solibore), an effect which has not been reported yet. This process is especially pronounced in the northern part of the slope-shelf area where the shelf break is shallower. The appearance of a secondary wave train implies that one initial incoming ISW can lead to the generation of two wave packets apart above the shelf break. It was further illustrated by a two-wave experiment that a wave packet above the shelf break is actually a superposition of a secondary solibore formed by an incoming ISW and an ISW packet that intrudes one tidal cycle later.

The issue of horizontal resolution was re-visited by comparing wave profiles obtained from different resolutions. It was found that a 250 m resolution is incapable of accurately simulating ISW evolution process in the shallow water. However, it successfully grasps the general features that are concerned. On the other hand, having elucidated the generation process and mechanism of the secondary solibore, the impacts of rotation on ISW profile were re-analyzed more quantitatively within the 3D circumstance.

Chapter 9

Thesis conclusions and summary

Dynamics of baroclinic tides and ISWs in the northern SCS are numerically explored in this research. MITgcm is used as the main tool to perform the numerical runs. Internal wave generation, structure, propagation, and shoaling in the northern SCS are focused on and simulated.

Internal wave generation processes at LS are modelled with the high-resolution three-dimensional MITgcm in the first place. A mixed lee wave regime is obtained over the majority of the LS in terms of the generation mechanism. Large amplitude ISWs of both first mode ($\sim 120\ m$) and second mode ($\sim 80\ m$) are generated after going through the double-ridge system in the LS. It is found that the eastern ridge causes the formation of the first mode, whereas the western ridge is indispensable for the emergence of the second mode.

Some intriguing short internal waves are found always riding on a second mode ISW. They feature a wavelength of $\sim 1.5\ km$ and an amplitude of $\sim 20\ m$. By solving the Taylor-Goldstein equation it turns out that it is the vertical shear induced by the second mode that leads to the appearance of such short waves. It is further confirmed that the short waves turn up at two distinct spots in the northern SCS that correspond to differing mechanisms: one mechanism is due to the disintegration of a baroclinic bore which appears just west of the western ridge. During this process ISWs of first mode and second mode emerge and this type of short waves show up riding on the second mode ISW; the other mechanism is owing to the overtaking of a faster first mode ISW over a slower second mode ISW that was generated one tidal cycle earlier. After the collision, the short waves emerge on the second mode ISW. Comparison of the model results with SAR images yields a good agreement.

Two types of ISWs are often classified in the northern SCS: A waves, which have larger amplitudes and arrive at a site regularly at the same time every day, and B waves, which are weaker and arrive one hour later every day. By scrutinizing historical observations, it was found that the occurrence of ISWs in the northern SCS always follows the maximum magnitude of semidiurnal barotropic tides in the LS. However, only semidiurnal tides can not generate A and B waves. The appearance of A and B ISWs is simulated by a series of two-dimensional experiments with realistic tidal forcing. It was found that the modulation of diurnal tides in the LS plays an substantial role in the characteristics of ISWs in the northern SCS, such as their amplitude, arrival time, number of waves in a packet. The A and B ISWs turn out to have complicated patterns and there is a transition between the two with a period of approximately fortnight. Model results are verified by some in situ measurements and reinforced by a linear tidal generation model.

The other focus of the present research concerns the shoaling process of ISWs above the slope and shelf of the northern SCS. First, shoaling of a large amplitude second mode ISW is simulated with the two-dimensional MITgcm, using a linear slope and stratification resembling that of the northern SCS. Wave profiles transform most severely near the turning point and the shelf break. Very rich wave structures arise on the shelf, and finally a stationary packet takes shape.

Second, the shoaling process of a first mode ISW is considered, with the emphasis on the role played by rotation. Large-scale three-dimensional experiments are first performed. Wave shoaling process is scrutinized in the three-dimensional context and the influence of rotation on wave shoaling is put forward. Given the huge demanding of three-dimensional simulations, a series of two-dimensional experiments are set up to examine the rotational effects. Two-dimensional experiments on purely rotational effects (constant depth) reveal that in the circumstance of the northern SCS, an initial ISW suffers from notable attenuation by constantly radiating inertia-gravity wave backwards, as is in contrast with previous studies in which a nearly localized wave packet was predicted. On the other hand, it is found that when variable topography is present, under rotational effect, a single ISW impinges on the slope and gives rise to two wave trains of different nature. The first train is an ISW packet and is linked directly to the initial ISW, whereas the second train is a solibore that consists of multiple short waves that resemble ISWs. The formation of the solibore is the outcome of combined effect of topography and rotation. Without rotation, the solibore nearly does not appear at all. It is also found that the secondary solibore is significantly more prominent in the northern portion of the slope-shelf area, but is largely weakened further south.

Throughout the numerical simulations presented in this dissertation, there are certain elements that have been missing. The significance of these omissions remains to be evaluated and the results are expected to be refined accordingly in the future. For example, Chapter 4 introduces three-dimensional simulations that only cover part of the LS and the northern SCS, which, together with the inclusion of M_2 tidal forcing only, is inadequate in accurately revealing ISW dynamics in the northern SCS. For the simulations of A and B ISWs in Chapter 6, multiple tidal harmonics are implemented, but the runs are all two-dimensional. The above points are concerned with the domain size and the length of simulation time, which are limited by the computing facilities due to the huge demand of computational power. By the same token, the simulation of a shoaling first mode ISW only takes place in the continental slope and shelf without considering wave generation and propagation. Furthermore, processes like internal tide shoaling, interaction of incoming internal tides with local barotropic tides, etc. are not taken into account. Also, for the shoaling process, the effects of bottom stress and the intensity and contribution of internal waves generated locally are not evaluated.

Future work calls for the refinement of the model and greater integration with observations. It is known that the demand on the model performance largely depends on the phenomena of interest and the desired accuracy. When simulating the dynamics of internal tides, which feature scales of $O(100)$ km, hydrostatic models with relatively coarse horizontal resolutions ($O(1) - O(10)$ km) are adequate for the purpose. However, when it comes to the simulation of large nonlinear ISWs in the northern SCS, a non-hydrostatic three-dimensional model with a fine resolution ($O(100)$ m) is required to accurately delineate wave characteristics like profile, amplitude, phase speed, etc. Coarse resolution will introduce considerable spurious numerical dispersion that can overwhelm the actual physical dispersion, seriously undermining the fidelity of the simulated results. Moreover, for the three-dimensional numerical simulation, complexity is added by the impacts of Kuroshio, which itself has been unclear in terms of its flowing patterns and structures in the LS. Taking into account the potential impacts of the pycnocline inclination and background currents related to the Kuroshio and the attendant eddy-shedding, a remedy could be that the internal wave generation model be coupled or nested with a general circulation model. However, its feasibility and outcome remain to be evaluated. Challenges remain, but with the rapid development of computer techniques, it is foreseeable in the near

future that the difficulties will be overcome and a comprehensive prediction system is expected to be built.

On the other hand, while the resolution and the size of the modelling domain are essential for the prediction of ISW characteristics, knowledge of correct stratification, bathymetry, and barotropic tidal forcing is desirable, and this requires the support from massive in situ observations which can be assimilated into the model. Also, the increase of in situ observations both in quantity and quality has been proven to be of great motivation and beneficial to the development and validation of numerical models. Especially in the recent years, modelling efforts have been increasingly synthesized with field observations and the capability of numerical simulations has consequently been substantially improved. Hence, working in combination with more observations should be taken forward in the future.

List of references.

Akylas, T. R. (1991), 'On the radiation damping of a solitary wave in a rotating channel.', *In Mathematical Approaches in Hydrodynamics* **ed. T Miloh**, 175–181. Philadelphia: SIAM.

Akylas, T. R. & Grimshaw, R. H. J. (1992), 'Solitary internal waves with oscillatory tails', *Journal of Fluid Mechanics* **242**, 279–298.

Alford, M. H. (2001), 'Internal Swell Generation: The Spatial Distribution of Energy Flux from the Wind to Mixed Layer Near-Inertial Motions', *Journal of Physical Oceanography* **31(8)**, 2359–2368.

Alford, M. H. (2003), 'Redistribution of energy available for ocean mixing by long-range propagation of internal waves', *Nature* **423**, 159–162.

Alford, M. H., Lien, R.-C., Simmons, H., Klymak, J., Ramp, S., Yang, Y. J., Tang, D. & Chang, M.-H. (2010), 'Speed and evolution of nonlinear internal waves transiting the South China Sea', *Journal of Physical Oceanography* **40**, 1338–1355.

Alford, M. H., MacKinnon, J. A., Nash, J. D., Simmons, H., Pickering, A., Klymak, J. M., Pinkel, R., Sun, O., Rainville, L., Musgrave, R., Beitzel, T., Fu, K.-H. & Lu, C.-W. (2011), 'Energy flux and dissipation in Luzon Strait: two tales of two ridges', *Journal of Physical Oceanography* **41(11)**, 2211–2222.

Alpers, W. (1985), 'Theory of radar imaging of internal waves', *Nature* **314**, 245–247.

Apel, J., Ostrovsky, L., Stepanyants, Y. & Lynch, J. F. (2006), Internal solitons in the ocean, Technical report, Woods Hole Oceanographic Institution.

Arbic, B., Richman, J., Shriver, J., Timko, P., Metzger, E. & Wallcraft, A. (2012), 'Global modeling of internal tides within an eddying ocean general circulation model', *Oceanography* **25(2)**, 20–29.

Baines, P. (1973), 'The generation of internal tides by flat-bump topography', *Deep Sea Research and Oceanographic Abstracts* **20**, 179–205.

Baines, P. (1995), *Topographic effects in stratified flows*, Cambridge University Press.

Balmforth, N. J., Ierley, G. & Young, W. (2002), 'Tidal conversion by subcritical topography', *Journal of Physical Oceanography* **32(10)**, 2900–2914.

Balmforth, N. J. & Peacock, T. (2009), 'Tidal conversion by supercritical topography', *Journal of Physical Oceanography* **39**, 1965–1974.

Bell, T. (1975*a*), 'Lee waves on stratified flows with simple harmonic time dependence', *J. Fluid Mech.* **67**, 705–722.

Bell, T. (1975*b*), 'Topographically generated internal waves in the open ocean', *Journal of Geophysical Research* **80(3)**, 320–327.

Benjamin, T. (1967), 'Internal waves of permanent form in fluids of great depth', *J. Fluid Mech.* **29**, 559–592.

Benny, D. (1966), 'Long nonlinear waves in fluid flows', *J. Math. & Phys.* **45**, 52–63.

Bole, J., Ebbesmeyer, C. & Romea, R. (1994), 'Soliton currents in the South China Sea: Measurements and theoretical modeling', *Proc. 26th Annual Offshore Technology Conf.* pp. 367–376. Houston, TX, OTC.

Boussinesq, J. (1871), 'Théorie de l'intumescence liquide, applelée onde solitaire ou de translation, se propageant dans un canal rectangulaire', *Comptes Rendus de l'Academie des Sciences* **72**, 755–759.

Buijsman, M., Kanarska, Y. & McWilliams, J. (2010), 'On the generation and evolution of nonlinear internal waves in the South China Sea', *Journal of Geophysical Research* **115**, C02012.

Buijsman, M., Legg, S. & Klymak, J. (2012), 'Double Ridge Internal Tide Interference and its Effect on Dissipation in Luzon Strait', *Journal of Physical Oceanography* **42**, 1337–1356.

Buijsman, M., McWilliams, J. & Jackson, C. (2010), 'East-west asymmetry in nonlinear internal waves from Luzon Strait', *Journal of Geophysical Research* **115**, C10057.

Cai, S., Long, X. & Gan, Z. (2002), 'A numerical study of the generation and propagation of internal solitary waves in the Luzon Strait', *Oceanologica Acta* **25**, 51–60.

Cai, S. & Xie, J. (2010), 'A propagation model for the internal solitary waves in the northern South China Sea', *Journal of Physical Oceanography* **115**, C12074.

Chang, M.-H., Lien, R.-C., Tang, T. Y., D'Asaro, E. a. & Yang, Y. J. (2006), 'Energy flux of nonlinear internal waves in northern South China Sea', *Geophysical Research Letters* **33**, L03607.

Chao, S.-Y., Ko, D.-S. & Shaw, P.-T. (2007), 'Assessing the west ridge of Luzon Strait as an internal wave mediator', *Journal of Oceanography* **63**, 897–911.

Chen, G.-Y., Liu, C.-T., Wang, Y.-H. & Hsu, M. K. (2011), 'Interaction and generation of long-crested internal solitary waves in the South China Sea', *Journal of Geophysical Research* **116**, C06013.

Choi, W. & Camassa, R. (1999), 'Fully nonlinear internal waves in a two-fluid system', *Journal of Fluid Mechanics* **396**, 1–36.

Da Silva, J. C. B., Ermakov, S. A., Robinson, I. S., Jeans, D. R. G. & Kijashko, S. V. (1998), 'Role of surface films in ERS SAR signatures of internal waves on the shelf 1. Short-period internal waves', *Journal of Geophysical Research* **103(C4)**, 8009–8031.

Davis, R. & Acrivos, A. (1967), 'Solitary internal waves in deep water', *J. Fluid Mech.* **29**, 593–607.

Du, T., Tseng, Y.-H. & Yan, X.-H. (2008), 'Impacts of tidal currents and Kuroshio intrusion on the generation of nonlinear internal waves in Luzon Strait', *Journal of Geophysical Research* **113**, C08015.

Duda, T. F., Lynch, J. F., Irish, J. D., Beardsley, R. C., Ramp, S. R., Chiu, C. S., Tang, T. Y. & Yang, Y. J. (2004), 'Internal tide and nonlinear internal wave behavior at the continental slope in the northern South China Sea', *IEEE Journal of Oceanic Engineering* **29**, 1105–1130.

Duda, T. F. & Rainville, L. (2008), 'Diurnal and semidiurnal internal tide energy flux at a continental slope in the South China Sea', *Journal of Geophysical Research* **113**, C03025.

Ebbesmeyer, C. C., Coomes, C. A., Hamilton, R. C., Kurrus, K. A., Sullivan, T. C., Salem, B. L., Romea, R. D. & Bauer, R. J. (1991), 'New observation on internal wave (soliton) in the South China Sea using acoustic Doppler current profiler', *Marine Technology Society 91 Proc., New Orleans* pp. 165–175.

Echeverri, P. & Peacock, T. (2010), 'Internal tide generation by arbitrary two-dimensional topography', *Journal of Fluid Mechanics* **659**, 247–266.

Egbert, G. & Erofeeva, S. (2002), 'Efficient inverse modeling of barotropic ocean tides', *Journal of Atmospheric and Oceanic Technology* **19(2)**, 183–204.

Egbert, G. & Ray, R. (2000), 'Significant dissipation of tidal energy in the deep ocean inferred from satellite altimeter data', *Nature* **405**, 775–778.

Evans, W. & Ford, M. (1996), 'An integral equation approach to internal (2-layer) soliary waves', *Physics of Fluids* **8(8)**, 2032–2047.

Farmer, D., Li, Q. & Park, J.-H. (2009), 'Internal wave observations in the South China Sea: The role of rotation and non-linearity', *Atmosphere-Ocean* **47(4)**, 267–280.

Fett, R. & Rabe, K. (1977), 'Satellite observation of internal wave refraction in the South China Sea', *Geophysical Research Letters* **4**(5), 189–191.

Fringer, O., Gerritsen, M. & Street, R. (2006), 'An unstructured-grid, finite-volume, nonhydrostatic, parallel coastal ocean simulator', *Ocean Modelling* **14(3-4)**, 139–173.

Fu, K.-H., Wang, Y.-H., St. Laurent, L., Simmons, H. & Wang, D.-P. (2012), 'Shoaling of large-amplitude nonlinear internal waves at Dongsha Atoll in the northern South China Sea', *Continental Shelf Research* **37**, 1–7.

Garrett, C. (2001), 'What is the "near-inertial" band and why is it different from the rest of the internal wave spectrum?', *Journal of Physical Oceanography* **31**, 962–971.

Garrett, C. & Kunze, E. (2007), 'Internal tide generation in the deep ocean', *Annual Review of Fluid Mechanics* **39(1)**, 57–87.

Gerkema, T. (1996), 'A unified model for the generation and fission of internal tides in a rotating ocean', *J. of Mar. Res.* **54**, 421–450.

Gerkema, T. (2001), 'Internal and interfacial tides: Beam scattering and local generation of solitary waves', *J. of Mar. Res.* **59**, 227–255.

Gerkema, T. & Zimmerman, J. (1995), 'Generation of nonlinear internal tides and solitary waves', *Journal of Physical Oceanography* **25**, 1081–1094.

Gilman, O., Grimshaw, R. & Stepanyants, Y. (1996), 'Dynamics of internal solitary waves in a rotating fluid', *Dynamics of Atmospheres and Oceans* **23**, 403–411.

Grimshaw, R. (1985), 'Evolution equations for weakly nonlinear, long internal waves in a rotating fluid', *Stud. Appl. Math.* **73**, 1–33.

Grimshaw, R., He, J.-M. & Ostrovsky, L. (1998), 'Terminal damping of a solitary wave due to radiation in rotational systems', *Studies in Applied Mathematics* **101**, 197–210.

Grimshaw, R. & Helfrich, K. (2008), 'Long-time Solutions of the Ostrovsky Equation', *Studies in Applied Mathematics* **121(1)**, 71–88.

Grimshaw, R. & Helfrich, K. (2012), 'The effect of rotation on internal solitary waves', *IMA Journal of Applied Mathematics* **77**, 326–339.

Grimshaw, R. & Tang, S. (1990), 'The rotation-modified kadomtsev-petviashvili equation : an analytical and numerical study', *Stud. Appl. Math.* **83**, 223–248.

Grue, J., Jensen, A., Rusas, P.-O. & Sveen, J. (1999), 'Properties of large-amplitude internal waves', *Journal of Fluid Mechanics* **380**, 257–278.

Guo, C. & Chen, X. (2012), 'Numerical investigation of large amplitude second mode internal solitary waves over a slope-shelf topography', *Ocean Modelling* **42**, 80–91.

Guo, C., Chen, X., Vlasenko, V. & Stashchuk, N. (2011), 'Numerical investigation of internal solitary waves from the Luzon Strait: generation process, mechanism and three-dimensional effects', *Ocean Modelling* **38**, 203–216.

Guo, C. & Vlasenko, V. (2012), 'The effect of rotation on shoaling of large amplitude internal solitary waves in the northern South China Sea', *Ocean Modelling* . (Submitted).

Guo, C., Vlasenko, V., Alpers, W., Stashchuk, N. & Chen, X. (2012), 'Evidence of short internal waves trailing strong internal solitary waves in the northern South China Sea from synthetic aperture radar observations', *Remote Sensing of Environment* **124**, 542–550.

Helfrich, K. (1992), 'Internal solitary waves breaking and run-up on a uniform slope', *J. Fluid Mech.* **243**, 133–154.

Helfrich, K. (2007), 'Decay and return of internal solitary waves with rotation', *Physics of Fluids* **19(2)**, 026601.

Helfrich, K. & Grimshaw, R. (2008), 'Nonlinear disintegration of the internal tide', *Journal of Physical Oceanography* **38**, 686–701.

Helfrich, K. & Melville, W. (1986), 'On long nonlinear internal waves over slope-shelf topography', *J. Fluid Mech.* **167**, 285–308.

Helfrich, K. & Melville, W. (2006), 'Long nonlinear internal waves', *Annual Review of Fluid Mechanics* **38**, 395–425.

Helfrich, K., Melville, W. & Miles, J. (1984), 'On interfacial solitary waves over slowly varying topography', *J. Fluid Mech.* **149**, 305–317.

Holloway, P., Pelinovsky, E. & Talipova, T. (1999), 'A generalized Korteweg-de Vries model of internal tide transformation in the coastal zone', *Journal of Geophysical Research* **104(C8)**, 18333–18350.

Holloway, P., Pelinovsky, E., Talipova, T. & Barnes, B. (1997), 'A nonlinear model of internal tide transformation on the australian north west shelf', *Journal of Physical Oceanography* **27**, 871–896.

Holt, B. (2005), 'SAR imaging of the ocean surface', *Synthetic Aperture Radar Marine User's Manual (Chapter 2). United States. Dept. of Commerce* .

Hsu, M. K., Liu, A. K. & Liu, C. (2000), 'A study of internal waves in the China Seas and Yellow Sea using SAR', *Continental Shelf Research* **20**, 389–410.

Huang, W., Johannessen, J., Alpers, W., Yang, J. & Gan, X. (2008), 'Spatial and temporal variations of internal waves sea surface signatures in the northern South China Sea studied by spaceborne SAR imagery', *in Proc. SeaSAR, Frascati, Italy, Jan.21-25* pp. 1–6.

Jackson, C., da Silva, J. & Jeans, G. (2012), 'The generation of nonlinear internal waves', *Oceanography* **25(2)**, 108–123.

Jackson, C. R. (2009), 'An Empirical Model for Estimating the Geographic Location of Nonlinear Internal Solitary Waves', *J. Atmos. Oceanic Technol.* **26**, 2243–2255.

Jan, S. & Chen, C.-T. A. (2009), 'Potential biogeochemical effects from vigorous internal tides generated in Luzon Strait: A case study at the southernmost coast of Taiwan', *Journal of Geophysical Research* **114**, C04021.

Jan, S., Chern, C.-S., Wang, J. & Chao, S.-Y. (2007), 'Generation of diurnal K_1 internal tide in the Luzon Strait and its influence on surface tide in the South China Sea', *Journal of Geophysical Research* **112**, C06019.

Jan, S., Chern, C.-S., Wang, J. & Chiou, M. (2012), 'Generation and propagation of baroclinic tides modified by the Kuroshio in the Luzon Strait', *Journal of Geophysical Research* **117**, C02019.

Jan, S., Lien, R.-C. & Ting, C.-H. (2008), 'Numerical study of baroclinic tides in Luzon Strait', *Journal of Oceanography* **64**, 789–802.

Joseph, R. (1977), 'Solitary waves in finite depth fluids', *J. Phys. A: Math. Gen.* **10(12)**, L225.

Kadomtsev, B. & Petviashvili, V. (1970), 'On the stability of solitary waves in weakly dispersing media', *Soviet Physics - Doklady* **15(6)**, 539–541.

Kang, D. & Fringer, O. (2012), 'Energetics of barotropic and baroclinic tides in the monterey bay area', *Journal of Physical Oceanography* **42(2)**, 272–290.

Kao, T., Pan, F. & Renouard, D. (1985), 'Internal solitons on the pycnocline: Generation, propagation and shoaling and breaking over a slope', *J. Fluid. Mech.* **159**, 19–53.

Katsis, C. & Akylas, T. R. (1987), 'Solitary internal waves in a rotating channel: A numerical study', *Physics of Fluids* **30(2)**, 297–301.

Kelly, S. M. & Nash, J. D. (2010), 'Internal-tide generation and destruction by shoaling internal tides', *Geophysical Research Letters* **37**, L23611.

Khatiwala (2003), 'Generation of internal tides in an ocean of finite depth: analytical and numerical calculations', *Deep Sea Research I* **50(1)**, 3–21.

Klymak, J., Legg, S. & Pinkel, R. (2010), 'A simple parameterization of turbulent tidal mixing near supercritical topography', *Journal of Physical Oceanography* **40(9)**, 2059–2074.

Klymak, J. M., Alford, M. H., Pinkel, R., Lien, R.-C., Yang, Y. J. & Tang, T.-Y. (2011), 'The Breaking and Scattering of the Internal Tide on a Continental Slope', *Journal of Physical Oceanography* **41**(5), 926–945.

Klymak, J. M., Pinkel, R., Liu, C.-T., Liu, A. K. & David, L. (2006), 'Prototypical solitons in the South China Sea', *Geophysical Research Letters* **33**, L11607.

Konyaev, K., Sabinin, K. & Serebryany, A. (1995), 'Large-amplitude internal waves at the Mascarene Ridge in the Indian Ocean', *Deep-Sea Research I* **42(11-12)**, 2075–2091.

Korteweg, D. & de Vries, G. (1895), 'On the change of form of long waves advancing in a rectangular canal and on a new type of long stationary waves', *Philosophical Magazine* **39**, 422–443.

Kubota, T., Ko, D. & Dobbs, L. (1978), 'Weakly-nonlinear, long internal gravity waves in a strarified fluid of finite depth', *Journal of Hydronautics* **12**, 157–165.

Lamb, K. (2002), 'A numerical investigation of solitary internal waves with trpped cores formed via shoaling', *Journal of Fluid Mechanics* **451**, 109–144.

Lamb, K. (2003), 'Shoaling solitary internal waves: on a criterion for the formation of waves with trapped cores', *Journal of Fluid Mechanics* **478**, 81–100.

Ledwell, J., Montgomery, E., Polzin, K., St. Laurent, L., Schmitt, R. & Toole, J. (2000), 'Evidence for enhanced mixing over rough topography in the abyssal ocean', *Nature* **403**, 179–182.

Ledwell, J., Watson, A. & Law, C. (1993), 'Evidence for slow mixing across the pycnocline from an open-ocean tracer-release experiment', *Nature* **364**, 701–703.

Lee, C.-Y. & Beardsley, R. (1974), 'The generation of long nonlinear internal waves in a weakly stratified shear flow', *Journal of Geophysical Research* **79**, 453–462.

Legg, S. & Huijts, K. (2006), 'Preliminary simulations of internal waves and mixing generated by finite amplitude tidal flow over isolated topography', *Deep Sea Research II* **53**, 140–156.

Legg, S. & Klymak, J. (2008), 'Internal hydraulic jumps and overturning generated by tidal flow over a tall steep ridge', *Journal of Physical Oceanography* **38(9)**, 1949–1964.

Leith, C. (1996), 'Stochastic models of chaotic systems', *Physica D* **98**, 481–491.

Leonov, A. (1981), 'The effect of the earth's rotation on the propagation of weak nonlinear surface and internal long oceanic waves', *Annals of the New York Academy of Sciences* **373**, 150–159.

Li, Q. (2010), 'Nonlinear internal waves in the South China Sea', *PhD thesis, University of Rhode Island* .

Li, Q. & Farmer, D. M. (2011), 'The Generation and Evolution of Nonlinear Internal Waves in the Deep Basin of the South China Sea', *Journal of Physical Oceanography* **41**(7), 1345–1363.

Li, Q., Farmer, D. M., Duda, T. F. & Ramp, S. (2009), 'Acoustical Measurement of Nonlinear Internal Waves Using the Inverted Echo Sounder', *Journal of Atmospheric and Oceanic Technology* **26**(10), 2228–2242.

Lien, R.-C., D'Asaro, E., Henyey, F., Chang, M.-H., Tang, T.-Y. & Yang, Y.-J. (2012), 'Trapped Core Formation within a Shoaling Nonlinear Internal Wave', *Journal of Physical Oceanography* **42**, 511–525.

Lien, R.-C., Tang, T., Chang, M. & D'Asaro, E. (2005), 'Energy of nonlinear internal waves in the South China Sea', *Geophysical Research Letters* **32**, L05615.

Liu, A., Chang, Y., Hsu, M.-K. & Liang, N. (1998), 'Evolution of nonlinear internal waves in the East and South China Seas', *Journal of Geophysical Research* **103**, 7995–8008.

Liu, A. & Hsu, M. (2004), 'Internal wave study in the South China Sea using Synthetic Aperture Radar (SAR)', *International Journal of Remote Sensing* **25**, 1261–1264.

Liu, C.-T., Pinkel, R., Klymak, J., Hsu, M.-K., Chen, H.-W. & Villanoy, C. (2006), 'Nonlinear internal waves from the Luzon Strait', *EOS, TRANSACTIONS AGU* **87(42)**, 449–451.

Liu, Q., Kaneko, A. & Su, J. (2008), 'Recent progress in studies of the South China Sea circulation', *Journal of Oceanography* **64(5)**, 753–762.

Llewellyn Smith, S. & Young, W. (2002), 'Conversion of the barotropic tide', *Journal of Physical Oceanography* **32**, 1554–1566.

Long, R. (1953), 'Some aspects of the flow of stratified fluids: I. a theoretical investigation', *Tellus* **5(1)**, 42–58.

Lynch, J., Ramp, S., Chiu, C.-S., Tang, T., Yang, Y.-J. & Simmen, J. (2004), 'Research Highlights from the Asian Seas International Acoustics Experiment in the South China Sea', *IEEE Journal of Oceanic Engineering* **29**, 1067–1074.

Marshall, J., Adcroft, A., Hill, C., Perelman, L. & Heisey, C. (1997), 'A finite-volume, incompressible Navier Stokes model for studies of the ocean on parallel computers', *Journal of Geophysical Research* **102**, 5753–5766.

Marshall, J., Hill, C., Perelman, L. & Adcroft, A. (1997), 'Hydrostatic, quasi-hydrostatic, and nonhydrostatic ocean modeling', *Journal of Geophysical Research* **102**, 5733–5752.

Maxworthy, T. (1979), 'A note on the internal solitary waves produced by tidal flow over a three-dimension ridge', *Journal of Geophysical Research* **84**, 338–346.

McCandless, S. & Jackson, C. (2005), 'Principles of Synthetic Aperture Radar', *Synthetic Aperture Radar Marine User's Manual (Chapter 1). United States. Dept. of Commerce* .

Merrifield, M. & Holloway, P. (2002), 'Model estimates of M_2 internal tide energetics at the Hawaiian Ridge', *Journal of Geophysical Research* **107(C8)**, 3179.

Michallet, H. & Ivey, G. (1999), 'Experiments on mixing due to internal soliary waves breaking on uniform slopes', *Journal of Geophysical Research* **104**, 467–477.

Miyata, M. (1985), 'An internal solitary wave of large amplitude', *La Mer* **23**, 43–48.

Miyata, M. (1988), 'Long internal waves of large amplitude', *In Nonlinear Water Waves, IUTAM Symposium Tokyo 1987* **ed. K. Horikawa and H. Maruo**, 399–406. Berlin: Springer-Verlag. 466 pp.

Moum, J., Nash, J. & Klymak, J. (2008), 'Small-scale processes in the coastal ocean', *Oceanography* **21(4)**, 22–33.

Munk, W. & Wunsch, C. (1998), 'Abyssal recipes II: energetics of tidal and wind mixing', *Deep Sea Research I* **45(12)**, 1977–2010.

Nakamura, T., Awaji, T., Hatayama, T., Akitomo, K., Takizawa, T., Kono, T., Kawasaki, Y. & Fukasawa, M. (2000), 'The generation of large-amplitude unsteady lee waves by subinertial K_1 tidal flow: A possible vertical mixing mechanism in the Kuril Straits', *Journal of Geophysical Research* **30**, 1601–1621.

Nash, J., Kunze, E., Lee, C. & Sanford, T. (2006), 'Structure of the Baroclinic Tide Generated at Kaena Ridge, Hawaii', *Journal of Physical Oceanography* **36(6)**, 1123–1135.

Niwa, Y. & Hibiya, T. (2004), 'Three-dimensional numerical simulation of M_2 internal tides in the East China Sea', *Journal of Geophysical Research* **109**, C04027.

Ono, H. (1975), 'Algebraic solitary waves in stratified fluids', *J. Phys. Soc. Japan* **39**, 1082–1091.

Orr, M. & Mignerey, P. (2003), 'Nonlinear internal waves in the South China Sea: Observation of the conversion of depression internal waves to elevation internal waves', *Journal of Geophysical Research* **108**, 3064.

Ostrovsky, L. (1978), 'Nonlinear internal waves in a rotating ocean', *Oceanology* **18**, 119–125.

Ostrovsky, L. & Grue, J. (2003), 'Evolution equations for strongly nonlinear internal waves', *Physics of Fluids* **15(10)**, 2934–2948.

Pacanowski, R. & Philander, S. (1981), 'Parameterization of vertical mixing in numerical models of Tropical Oceans', *Journal of Physical Oceanography* **11**, 1443–1451.

Pan, X., Wong, G. T. F., Shiah, F.-K. & Ho, T.-Y. (2012), 'Enhancement of biological productivity by internal waves: observations in the summertime in the northern South China Sea', *Journal of Oceanography* **68(3)**, 427–437.

Pétrélis, F., Llewellyn Smith, S. & Young, W. (2006), 'Tidal conversion at a submarine ridge', *Journal of Physical Oceanography* **36(6)**, 1053–1071.

Polzin, K., Toole, J., Ledwell, J. & Schmitt, R. (1997), 'Spatial variability of turbulent mixing in the abyssal ocean', *Science* **276**, 93–96.

Rainville, L. & Pinkel, R. (2006), 'Baroclinic Energy Flux at the Hawaiian Ridge: Observations from the R/P FLIP', *Journal of Physical Oceanography* **36(6)**, 1104–1122.

Ramp, S. R., Tang, T. Y., Duda, T. F., Lynch, J. F., Liu, A. K., Chiu, C. S., Bahr, F. L., Kim, H. R. & Yang, Y. J. (2004), 'Internal solitons in the northeastern South China Sea. part I: Sources and deep water propagation', *IEEE Journal of Oceanic Engineering* **29**, 1157–1181.

Ramp, S. R., Yang, Y. & Bahr, F. (2010), 'Characterizing the nonlinear internal wave climate in the northeastern South China Sea', *Nonlinear Processes in Geophysics* **17**, 481–498.

Rayleigh, L. (1876), 'On waves', *Philosophical Magazine* **1**, 257–279.

Russell, J. (1844), 'Report on waves', *Proceedings of the 14th meeting of the British Association for the Advancement of Science, York* **John Murray: London**, 311–390.

Sánchez-Garrido, J. & Vlasenko, V. (2009), 'Long-term evolution of strongly nonlinear internal solitary waves in a rotating channel', *Nonlin. Processes Geophys.* **16**, 587–598.

Scotti, A., Beardsley, R., Butman, B. & Pineda, J. (2008), 'Shoaling of noninear internal waves in Massachusetts Bay', *Journal of Geophysical Research* **113**, C08031.

Shaw, P.-T., Ko, D. & Chao, S.-Y. (2009), 'Internal solitary waves induced by flow over a ridge: With applications to the northern South China Sea', *Journal of Geophysical Research* **114**, C02019.

Shen, C., Evans, T., Oba, R. & Finette, S. (2009), 'Three-dimensional hindcast simulation of internal soliton propagation in the Asian Seas International Acoustics Experiment area', *Journal of Geophysical Research* **114**, C01014.

Shroyer, E., Moum, J. & Nash, J. (2010), 'Mode 2 waves on the continental shelf: Ephemeral components of the nonlinear internal wavefield', *Journal of Geophysical Research* **115**, C07001.

Simmons, H. & Alford, M. H. (2012), 'Simulating the long-range swell of internal waves generated by ocean storms', *Oceanography* **25(2)**, 30–41.

Simmons, H., Hallberg, R. & Arbic, B. (2004), 'Internal wave generation in a global baroclinic tide model', *Deep Sea Research II* **51(25-26)**, 3043–3068.

St. Laurent, L. (2008), 'Turbulent dissipation on the margins of the South China Sea', *Geophysical Research Letters* **35**, L23615.

St. Laurent, L. & Garrett, C. (2002), 'The role of internal tides in mixing the deep ocean', *Journal of Physical Oceanography* **32**, 2882–2899.

St. Laurent, L., Stringer, S., Garrett, C. & Perrault-Joncas, D. (2003), 'The generation of internal tides at abrupt topography', *Deep Sea Research I* **50(8)**, 987–1003.

Stanton, T. & Ostrovsky, L. (1998), 'Observations of highly nonlinear solitons over the continental shelf', *Geophysical Research Letters* **25**, 2695–2698.

Stastna, M. & Lamb, K. (2002), 'Large fully nonlinear internal solitary waves: The effect of background current', *Physics of Fluids* **14(9)**, 2987–2999.

Stastna, M., Poulin, F., Rowe, K. & Subich, C. (2009), 'On fully nonlinear, vertically trapped wave packets in a stratified fluid on the f-plane', *Physics of Fluids* **21**, 106604.

Stepanyants, Y. (2006), 'On stationary solutions of the reduced ostrovsky equation: Periodic waves, compactons and compound solitons', *Chaos, Solitions & Fractals* **28(1)**, 193–204.

Turner, R. & Vanden-Broeck, J.-M. (1988), 'Broadening of interfacial solitary waves', *Physics of Fluids* **31(9)**, 2486–2490.

Vitousek, S. & Fringer, O. (2011), 'Physical vs. numerical dispersion in nonhydrostatic ocean modeling', *Ocean Modelling* **40(1)**, 72–86.

Vlasenko, V., Guo, C., Stashchuk, N. & Chen, X. (2012), 'On the mechanism of A-type and B-type internal solitary wave generation in the northern South China Sea', *Deep Sea Research I* **69**, 100–112.

Vlasenko, V. & Hutter, K. (2001), 'Generation of second mode solitary waves by the interaction of a first mode soliton with a sill', *Nonlinear Processes in Geophysics* **8**, 223–239.

Vlasenko, V. & Hutter, K. (2002), 'Numerical experiments on the breaking of solitary internal waves over a slope-shelf topography', *Journal of Physical Oceanography* **32**, 1779–1793.

Vlasenko, V. & Stashchuk, N. (2007), 'Three-dimensional shoaling of large-amplitude internal waves', *Journal of Geophysical Research* **112**, C11018.

Vlasenko, V., Stashchuk, N., Guo, C. & Chen, X. (2010), 'Multimodal structure of baroclinic tides in the South China Sea', *Nonlinear Processes in Geophysics* **17**, 529–543.

Vlasenko, V., Stashchuk, N. & Hutter, K. (2005), *Baroclinic tides: theoretical modeling and observational evidence*, Cambridge University Press.

Warn-Varnas, A., Hawkins, J., Lamb, K., Piacsek, S., Chin-Bing, S., King, D. & Burgos, G. (2009), 'Solitary wave generation dynamics at Luzon Strait', *Ocean modelling* **31**, 9–27.

Whitham, G. (1974), *Linear and nonlinear waves*, New York: Wiley.

World Ocean Atlas (2009). http://www.nodc.noaa.gov/OC5/WOA09/pr_woa09.html.

Wunsch, C. & Ferrari, R. (2004), 'Vertical mixing, energy, and the general circulation of the oceans', *Annual Review of Fluid Mechanics* **36**, 281–314.

Yang, Y., Fang, Y., Chang, M.-H., Ramp, S., Kao, C.-C. & Tang, T. (2009), 'Observations of second baroclinic mode internal solitary waves on the continental slope of the northern South China Sea', *Journal of Geophysical Research* **114**, C10003.

Yang, Y., Fang, Y., Tang, T. & Ramp, S. (2010), 'Convex and concave types of second baroclinic mode internal solitary waves', *Nonlin. Processes Geophys.* **17**, 605–614.

Yang, Y., Tang, T., Chang, M., Liu, A., Hsu, M. & Ramp, S. (2004), 'Solitons northeast of Tung-Sha Island during the ASIAEX pilot studies', *IEEE Journal of Oceanic Engineering* **29**, 1182–1199.

Yuan, D. L., Han, W. Q. & Hu., D. X. (2006), 'Surface Kuroshio path in the Luzon Strait area derived from satellite remote sensing data', *Journal of Geophysical Research* **111**, C11007.

Yuan, Y., Zheng, Q., Dai, D., Hu, X., Qiao, F. & Meng., J. (2006), 'Mechanism of internal waves in the Luzon Strait', *Journal of Geophysical Research* **111**, C11S17.

Zabusky, N. J. & Kruskal, M. D. (1965), 'Interaction of "solitons" in a collisionless plasma and the recurrence of initial states', *Physical Review Letters* **15**, 240–243.

Zhang, Z., Fringer, O. & Ramp, S. (2011), 'Three-dimensional, nonhydrostatic numerical simulation of nonlinear internal wave generation and propagation in the South China Sea', *Journal of Geophysical Research* **116**, C05022.

Zhao, Z. & Alford, M. H. (2006), 'Source and propagation of internal solitary waves in the northeastern South China Sea', *Journal of Geophysical Research* **111**, C11012.

Zhao, Z., Klemas, V., Zheng, Q. & Yan, X. (2004), 'Remote sensing evidence for baroclinic tide origin of internal solitary waves in the northeastern South China Sea', *Geophysical Research Letters* **31**, L06302.

Zhao, Z., Klemas, V., Zheng, Q. & Yan, X.-H. (2003), 'Satellite observation of internal solitary waves converting polarity', *Geophysical Research Letters* **30(19)**, 1988.

Zheng, Q., Susanto, R. D., Ho, C.-R., Song, Y. & Xu, Q. (2007), 'Statistical and dynamical analyses of generation mechanisms of solitary internal waves in the northern South China Sea', *Journal of Geophysical Research* **112**, C03021.

Zheng, Q., Yuan, Y., Klemas, V. & Yan, X. (2001), 'Theoretical expression for an ocean internal soliton synthetic aperture radar image and determination of the soliton characteristic half width', *Journal of Geophysical Research* **106(C12)**, 31415–31423.

Zu, T., Gan, J. & Erofeeva, S. (2008), 'Numerical study of the tide and tidal dynamics in the South China Sea', *Deep-Sea Res. I* **55**, 137–154.

Bound copies of published papers.